THESE EN CO-TUTELLE
présentée pour obtenir le grade de
Docteur de l'Université de Lille
en Structure et Dynamique des Systèmes Réactifs

par
Roman JAWORSKI

THE PROPERTIES OF HYDROXYAPATITE AND TITANIUM OXIDE COATINGS OBTAINED BY SUSPENSION PLASMA SPRAYING

LES PROPRIÉTÉS DE DEPOTS DE L'HYDROXYAPATITE ET DE L'OXYDE DE TITANE OBTENUS PAR LA PROJECTION PLASMA DE SUSPENSION

Version finale
Date de soutenance : 30.09.2009

Directeurs de thèse : Prof. Lech PAWLOWSKI, ENSC Lille, France
Prof. Jerzy ZDANOWSKI, WUT Wroclaw, Pologne

Rapporteurs : Prof. Anne LERICHE - Université de Valenciennes et du Hainaut Cambrésis
Prof. Igor SMUROV - ENI Saint Etienne
Prof. Stanislaw MITURA - Université Technique de Lodz, Pologne

Examinateurs : Prof. Didier CHICOT - Université de Sciences et Technologies de Lille I
Prof. Tadeusz BERLICKI - Université de Technologie de Wroclaw, Pologne
Prof. Andrzej DZIEDZIC - Université de Technologie de Wroclaw, Pologne

Septembre 2009
Villeneuve d'Ascq

I would like to express my gratitude to Prof. Lech Pawlowski
and Prof. Jerzy Zdanowski for the help and directions during realization of the thesis.
Also the help of Prof. K. Nitsch and Drs F. Roudet, S. Kozerski, T. Piasecki,
Ch. Pierlot and Z. Znamirowski is warmly acknowledged.
I would like to thank Prof. Anne Leriche, Prof. Igor Smurov and
Prof. Stanisław Mitura for their efforts in reviewing this thesis.
I appreciate the partnership of the ENSCL students Maxime Quivrin and
Romain D'Haese in some projects of this thesis.

CONTENT

LIST OF ABBREVIATIONS

APS	Atmospheric Plasma Spraying
AS	Arc Spraying
BSE	Back Scattered Electrons
BSF	Body Simulated Fluid
CAPS	Controlled Atmosphere Plasma Spraying
CDHA	Calcium Deficient Hydroxyapatite
CGMS	Cold Gas Method Spraying
CPE	Constant Phase Element
CSN	Continuous Stream Nozzle
CTE	Coefficient of Thermal Expansion
CVD	Chemical Vapor Deposition
DC	Direct Current
D-GUN^{TM}	Detonation Gun Spraying
DOE	Design of Experiments
EDS	Energy Dispersive Spectrometer
EMPA	Electron Probe - Micro Analyzer
FED	Field Emitting Display
FS	Flame Spraying
GLR	Gas-to-Liquid mass Ratio
HA	Hydroxyapatite
HVOF	High Velocity Oxy Fuel
ICDD	International Center of Diffraction Data
IR	Infrared Spectroscopy
IS	Impedance Spectroscopy
ISM	Internal Standard Method
JCPDS	Joint Committee on Powder Diffraction Standards
LCD	Liquid Crystal Display
OHA	Oxyhydroxyapatite
PID	Proportional Integral Derivative (controller)
PVA	Poly Vinyl Alcohol
PVD	Physical Vapor Deposition
PVS	Pressurized Vessel System
RF	Radio Frequency
RFPPS	Radio Frequency Precursor Plasma Spraying
RIR	Reference Intensity Ratio
RTA	Reverse Transferred Arc
SEM	Scanning Electron Microscope
SOFC	Solid Oxide Fuel Cell
SPPS	Solution Precursor Plasma Spraying
SPS	Suspension Plasma Spraying
TBC	Thermal Barrier Coating
TCP	Tri-calcium Phosphate
TEM	Transmission Electron Microscopy
TTCP	Tetra-calcium Phosphate
VCS	Vacuum Cold Spraying
VPS	Vacuum Plasma Spraying
WDS	Wavelength Dispersive X-ray Spectrometer
XPS	X-ray Photoelectron Spectroscopy
XRD	X-ray Diffraction
YIG	Yttrium Iron Garnet
YPSZ	Yttria Partially Stabilized Zirconia
YSZ	Yttria-Stabilized Zirconia

LIST OF SYMBOLS

b_0	the mean of responses
[Ca]	solution of calcium nitrate tetrahydrate
C	capacitance
C_A	content of anatase
C_{Acor}	corrected content of anatase
C_{dry}	capacitance of dry sample
C_p	parallel capacitance
C_{PAR}	capacitance of the fixture and electrodes
d	distance between covers, scratch width
d_p	particle diameter
D_h	internal diameter of hose connecting powder feeder and injector
D_i	internal diameter of powder injector attached to plasma torch
E_a	energy of activation
F_g	direction of the evaporated gas-induced force
F_h	heat transfer direction from the droplet to the substrate
F_m	flow direction of the spreading fluid resulting from the crater
q_{cg}	carrier gas flow rate
G	conductivity
HS_L	scratch hardness
I_A	intensity of anatase (101) peak
I_R	intensity of rutile (110) peak
j	imaginary unit
k	coefficient of crystallite form
K_{CP}	coefficient of amount of water present in the sample
l	characteristic length (typically the droplet diameter)
L	normal force
L_C	critical load
L_h	length of hose connecting powder feeder and injector
L_i	length of powder injector attached to plasma torch
M"	imaginary dielectric modulus
n	parameter of CPE
Oh	Ohnesorge number
[P]	solution of diamonnium hydrogenposphate
pH_i	pH initial, power hydrogen of initial solution
pH_f	pH final, power hydrogen of final solution
Q	parameter of CPE (CPE factor)
Re	Reynolds number
R_S	parasitic resistance
s	surface of covers
tg δ	loss factor
U_{h_cg}	final velocity of carrier gas in hose
U_{h_p}	final velocity of powder particles in hose
U_{i_cg}	final velocity of carrier gas in injector
U_{i_p}	final velocity of powder particles in injector
V_{amon}	volume of ammonia
We	Weber number
Y	admittance

β	full width in half height
β_m,	full width in half height corrected by device deviation
β_0	device deviation
ε_o	permittivity of free space
ε_r	relative permittivity of dielectric
η_g	gas dynamic viscosity
λ	wave length
μ	liquid viscosity
ν	liquid velocity
ν_g	gas velocity
ν_p	particle velocity
ρ	liquid density
ρ_A	density of anatase
ρ_g	gas density
ρ_R	density of rutile
σ	surface tension
θ	angle of scan
ω	angular frequency

LIST OF FIGURES

LIST OF TABLES

1 INTRODUCTION

The materials investigated during realization of the thesis were hydroxyapatite ($Ca_{10}(PO_4)_6(OH)_2$) and titanium oxide (TiO_2). The investigations were a continuation of author's previous investigations as well as investigations realized before in the laboratories were the thesis was realized. The hydroxyapatite coatings are commonly used as coatings on the medical implants and thin titanium oxide coatings may be used in those coatings as bond coat. HA with TiO_2 could improve the properties of the coatings if it was as the intermediate gradient coatings. The goal of the thesis was to obtain the finely structured coatings of the materials, mentioned above, and examine the influence of process parameters on the coating properties.

The method of the coatings deposition was chosen suspension plasma spraying (SPS). The method is relatively new because it grew up as modification of atmospheric plasma spraying (APS) about 10 years ago. It also let one to obtain thinner and finely structured coatings. At Ecole Nationale Supérieure de Chimie de Lille (ENSCL), SPS was developed by adopting APS installation in the Laboratory of Thermal Spraying . To study the whole process of hydroxyapatite coating formation from the beginning to the end, synthesis and optimization of synthesis parameters of HA powder were carried out. Optimization of the SPS process parameters to find its influence on coating properties was performed using design of experiments (DOE). Various methods of investigation were used to observe some of the properties of those coatings. Microstructure and phase composition were tested by X-ray diffraction (XRD), scanning electron microscope (SEM), transmission electron microscope (TEM), micro-Raman spectroscopy and infrared spectroscopy (IR). Some mechanical properties were investigated by scratch test. Useful electrical measurements were carried out by impedance spectroscopy (IS).

Also very important property, which is strongly connected with the applications of hydroxyapatite (HA) coatings, is corrosion and dissolution resistance, this is why corrosion tests in body simulated fluid (BSF) were carried out.

The thesis was realized as co-tutelle at the two units, one in France – Ecole Nationale Supérieure de Chimie de Lille and second in Poland – Wroclaw University of Technology at the Faculty of Microsystem Electronics and Photonics.

1.1 THERMAL SPRAYING - DEPOSITION METHODS FAMILY

The family of thermal spraying includes few methods of deposition where a coating is made as a kind of brick wall where the bricks are molten, partially molten or solid particles of material deposited on a substrate. The coating is built up from stream of particles of deposited material heated by high efficiency heat source [1,2].

The differences between the methods result from variety of heat sources and average velocity of particles during the spraying.

These methods have a lot of advantages; one of them is that processes of this family are very simple and it is not necessary to prepare special atmosphere, excluding controlled atmosphere plasma spraying (CAPS), what causes that it is relatively cheap in comparison with physical or chemical vapor deposition (PVD, CVD).

Global market of thermal spraying enclosed about 4.8 billion Euros in 2004, 50% of it was devoted to plasma spraying where more than 90% of industrial spraying installations operated with Direct Current (DC) plasma torches, in the rest part among the others Radio Frequency (RF) plasma torches were used as a heart of spraying systems [3].

1.1.1 Flame Spraying (FS)

Flame Spraying is considered as the oldest thermal spraying process. It is cost-effective in regard both to equipment and maintenance costs.

The process consists of the combustion of a fuel gas which produces a flame in which the material to be sprayed is injected, molten and accelerated towards the substrate. Two different flame spray techniques exist depending on the form of the material to be sprayed, i.e. wire or powder.

There is a variety of the materials which are deposited by this method:
- metals and alloys
- ceramics
- composites
- plastics

Flame sprayed coatings are mainly used as:
- wear resistant coatings
- corrosion resistant coatings
- heat resistant coatings
- for reparation and refurbishing of worn parts.

1.1.2 Arc Spraying (AS)

In the arc spraying process a pair of electrically conductive wires is melted by existing between them electric arc, caused by applied electrical voltage. The molten material is atomized by compressed air and accelerated towards the substrate. The molten particles impacting on the substrate rapidly solidify to form a coating. This process carried out correctly is called a "cold process" (relative to the substrate material being coated) as the substrate temperature can be kept low during the processing what allows us to avoid damage, metallurgical changes and distortion of the substrate material. Electric arc spray coatings are normally denser and stronger than their equivalent flame spray coatings. Low running costs, high spray rates and efficiency make it a good tool for spraying large areas at high production rates. There are two basic disadvantages of the electric arc spraying process: only electrically conductive wires can be used as the sources of sprayed materials and a separate heat source is necessary when substrate preheating is required.

Main applications of the arc sprayed coatings are:
- anti-corrosion layers of zinc and aluminium
- prevention of machine excessive components wear.

1.1.3 Detonation Gun Spraying (D-Gun™)

The detonation gun basically consists of a long water-cooled barrel with inlet valves for gases and powder. Oxygen and fuel (acetylene most common) is fed into the barrel along with a charge of powder. A spark is used to ignite the gas mixture and resulting detonation heats and accelerates the powder to supersonic velocity down the barrel. A pulse of nitrogen is used to purge the barrel after each detonation pulse. This process is repeated many times.

The high kinetic energy of the hot powder particles during the impact with the substrate results in a build up of a very dense and strong coating. The total coating consists of many overlapping disks.

Typical applications:
- thermal barrier coatings
- erosion – corrosion resistant coatings
- wear resistant coatings.

1.1.4 High Velocity Oxy Fuel (HVOF)

There are a number of HVOF guns which use different methods to achieve high velocity of sprayed particles. One method uses a high pressure water-cooled HVOF combustion chamber and a long nozzle. Fuel (kerosene, acetylene, propylene and hydrogen) and oxygen are fed into the chamber, where the combustion produces a hot high pressure flame which is forced inside a nozzle to increase its velocity. The powder may be fed axially into the HVOF combustion chamber under high pressure or fed through the side of De Laval type nozzle, presented in Figure 1.1, where the pressure is lower. Another method uses a simpler system of a high pressure combustion nozzle and air cap. Fuel gas (propane, propylene or hydrogen) and oxygen are supplied at high pressure, the combustion occurs outside the nozzle but within an air cap supplied with compressed air. The compressed air pinches and accelerates the flame and acts as a coolant for the HVOF gun. The powder is fed at high pressure axially from the centre of the nozzle.

The coatings are very dense, strong and show low residual tensile stress or in some cases compressive stress, which enables deposition of much thicker coatings than by other previously mentioned processes[4].

Due to very high kinetic energy of the particles striking the substrate full melting of the particles is not necessary to form a high quality coating. This is certainly an advantage for the carbide cermet type coatings and therefore this process is really excellent for this material.

HVOF coatings are used in applications requiring lower oxidation of coating and the highest density and strength not found in most other thermal spraying processes [5,6].

The most common applications of coatings obtained by HVOF enclose:
- wear resistant components
- anti-corrosion coatings
- biocompatible coatings [7].

1.1.5 Vacuum Plasma Spraying (VPS)

Vacuum plasma spraying is a process typically performed in the chamber at 39–120°C to avoid thermal damage of deposited material. The process can induce non-thermally activated surface reactions, causing surface changes which cannot occur with molecular chemistries at atmospheric pressure [8].

Plasma processing is done in a controlled environment inside a sealed chamber under low pressure, around 13–65 Pa. The gas or mixture of gases is energized by an electrical field from DC to microwave frequencies, typically 1–500 W at 50 V. The treated components are

usually electrically isolated. The volatile plasma by-products are evacuated from the chamber by the vacuum pump, and if necessary can be neutralized in an exhaust scrubber.
In contrast to molecular chemistry, molecular, atomic, metastable and free radical species, existing in plasma are employed simultaneously for chemical effects.

Plasma also generates electromagnetic radiation in the form UV photons to penetrate bulk polymers to a depth of about 10 μm. This can cause chain scissions and cross-linking.

Typical applications of VPS coatings are:

- hot corrosion – resistant coatings
- production of coatings without impurities from air
- spraying of pure copper or tantalum coatings [1].

1.1.6 Controlled Atmosphere Plasma Spraying (CAPS)

The method bases on the same spray torch as used in atmospheric plasma spraying, the only difference is atmosphere surrounding the torch. The spray gun is operating in a chamber within a completely controlled environment. The atmosphere inside the chamber can change in the range from near vacuum (from 50 mbar) to elevated pressures (up to 4 bar). The spraying chamber may be chosen to prevent contamination of the coating material and substrate, or when a reaction of the coating material with a specifically introduced substance is desired. The coatings are very dense, extremely well bonded, free of contamination. Metallic coatings are free of oxides. Non-metallic coatings, such as ceramics sprayed in chambers backfilled with non-reactive atmospheres, are very pure. A unique feature of the controlled atmosphere spray process is the ability to use Reverse Transferred Arc (RTA) to metallurgical cleaning of the working piece without taking out from the chamber, what allows CAPS process to follow immediately.

CAPS coatings are mostly applied as:

- biocompatible ceramics coatings
- thermal barrier coatings
- wear resistant coatings.

1.1.7 Cold Gas Method Spraying (CGMS)

The process is sometimes called Cold Gas Spraying. The process basically uses high pressure compressed gas to transport particles of fine powder at very high velocities (500 - 1500 m/s). Compressed gas, usually helium, is fed via a heating unit to the gun where the gas exits through a specially designed nozzle (usually De Laval type, Figure1.1.) at very high velocity. The gas is also pressed via high pressure powder feeder to introduce powder material into the high velocity gas jet. The powder particles are heated to higher temperature and accelerated to higher velocity, while impacting on substrate they deform as splats and form the coating. The particles remain in the solid state and are relatively cold. Advantages of this process is that during the spraying only weak oxidation occurs, during cooling down the coatings are less stressed because of lack of large and rapid temperature changes in comparison to the changes which occur when material is transformed from liquid to solid state in other processes of thermal spraying, where high temperature gradients exist.

The most typical applications of CGMS coatings are:
- corrosion protection
- electrical and thermal conductive coatings.

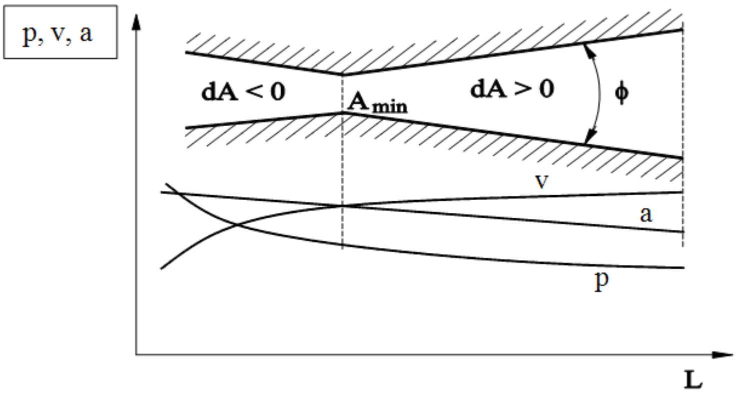

Figure 1.1 *De Laval type nozzle cross-section with marked changes of pressure p, velocity v and speed of sound a along the nozzle L.*

A variant of cold gas spraying is Vacuum Cold Spraying (VCS) presented schematically in Figure 1.2. where the system consists of a vacuum chamber and vacuum pump, an aerosol room and accelerating gas, feeding unit, a particle accelerating nozzle, work table and a control unit. Crystalline structure doesn’t change after deposition what can suggest that the structure of the powder can be retained in the coating (not under influence of high temperature).

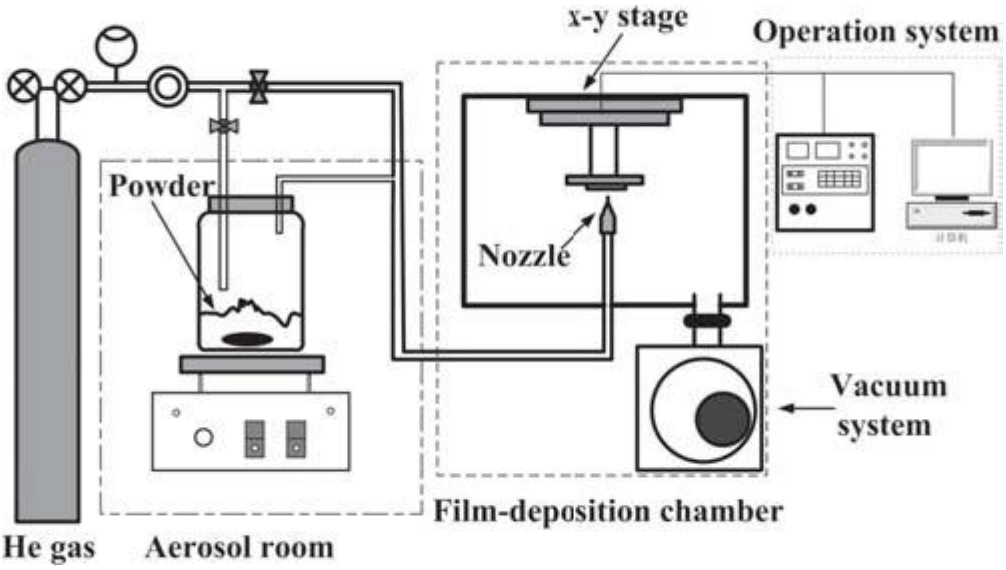

Figure 1.2 *Schematic diagram of VCS [9].*

1.1.8 Atmospheric Plasma Spraying (APS)

Atmospheric Plasma Spraying method was patented at the beginning of 1960 by Giannini and Ducati [10] and in 1962 by Gage et al. [11]. The torch of plasma spraying is based on the Gerdien [12] type plasma generator.

APS is used in many branches of industry [2] from medical [13,14], through automotive [15] and transportation to aerospace [16]. Rico et al. presented the results of anti-wear properties of coatings deposited by atmospheric plasma spraying from agglomerated nanostructured alumina –titania powder [17]. The method can apply very wide variety of coating materials and it is also used for covering differently shaped surfaces from big print rollers to very small part of dental prosthesis.

Principle of this method is based on electric arc ignition between an anode (nozzle) and cathode (electrode). A sketch of typical plasma torch is presented in Figure 1.3. Process gases, most often mixtures of argon, nitrogen, hydrogen and helium, flow between the electrodes and are ionized to become flame of hot plasma gas. Different mixtures of plasma gases let one to get different temperatures of plasma jets and different enthalpies. Physical properties of gases used for plasma spraying are listed in the Table. 1.1 [18]. Usually plasma jet core has temperature ranging from 8000^{0}C to 20000^{0}C. The temperature can be adjusted by the construction of plasma torch, choice of plasma gases and electrical parameters of electric arc [19]. Examples of temperature and velocity distribution in plasma jet are presented in Figure 1.4. When powder of the coating material is injected by carrier gas, into the plasma jet, it is melted, accelerated and propelled towards the substrate. When the stream of melted or partially melted particles reaches the substrate, each particle forms a splat. Coating is formed by the splats overlapping. Typical spraying distances used in APS are in range from 8 to 12 cm.

Table 1.1 Physical properties of plasma gases [18].

Type of gas Physical property	Ar	He	H_2	N_2
Density, [kg/m^3]	1.78	0.178	0.098	1.25
Ionization energy, [eV]	15.7	24.9	15.4	14.5
Dissociation energy, [J/mol]	-	-	4.3x10^5	9.4x10^5
Thermal capacity, [J/(mol·^{0}C)]	21	21	35	-
Thermal conduction coefficient at 6000 K, [W/(m·^{0}C)]	0.17	1.5	2.0	-
Boiling temperature, [^{0}C]	-185.5	-268.9	-259	-196

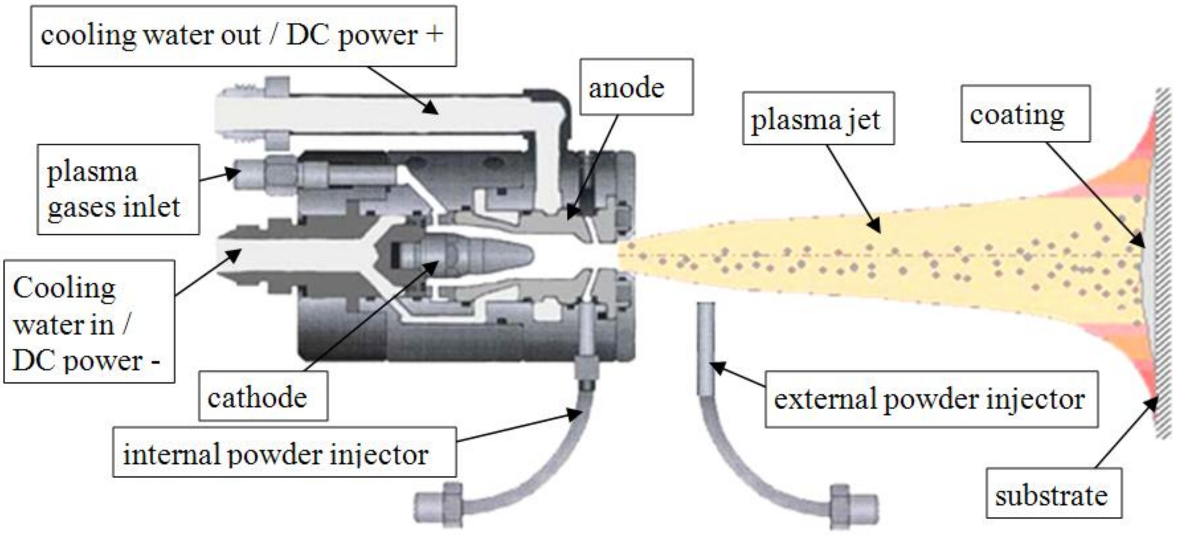

Figure 1.3 *Cross-section of a Praxair SG-100 plasma torch.*

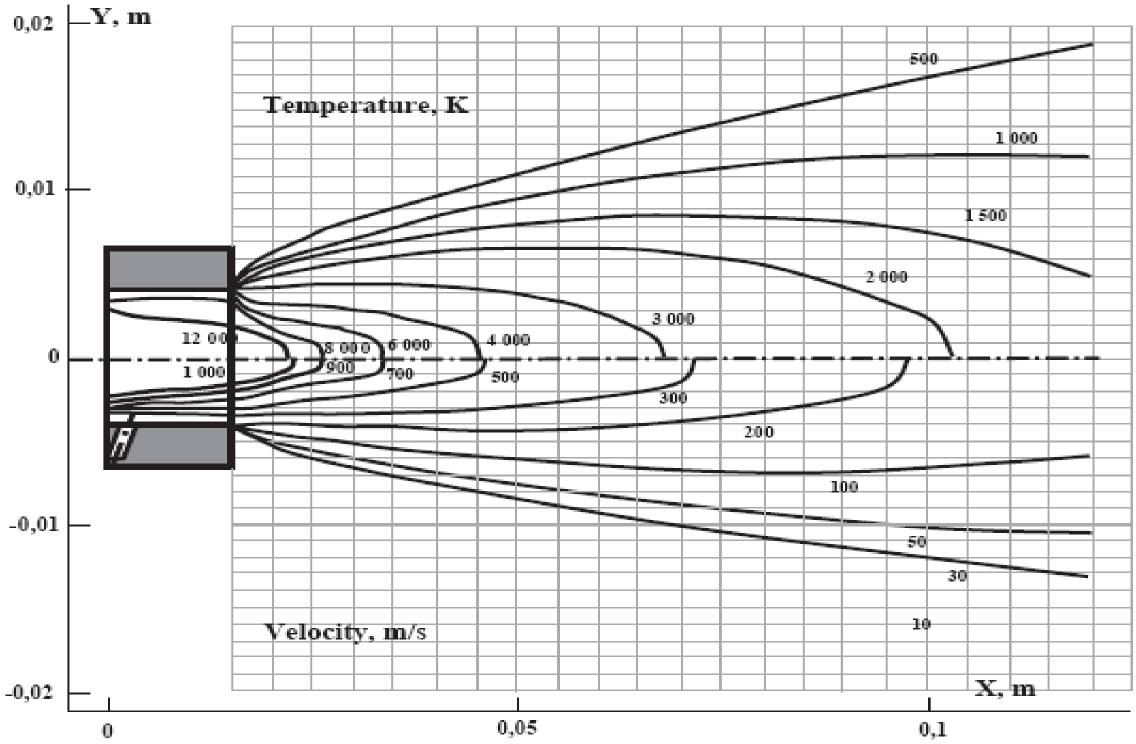

Figure 1.4 *Calculated profiles of temperatures and velocities of a plasma jet generated by SG-100 torch supplied with 24 kW of electric power and plasma forming gases Ar+2.5 vol.%* H_2 *with a total flow rate of 50 slpm [20].*

Powders are the most typical form of initial material for APS coating deposition. The powders for APS applications are produced by the ways listed below:

- spray drying
- cladding
- sintering

- fusing
- crushing.

Typical images of powders used for atmospheric plasma spraying are presented in Figure 1.5. The size distribution of those powders usually ranges from few to few hundreds of micrometers.

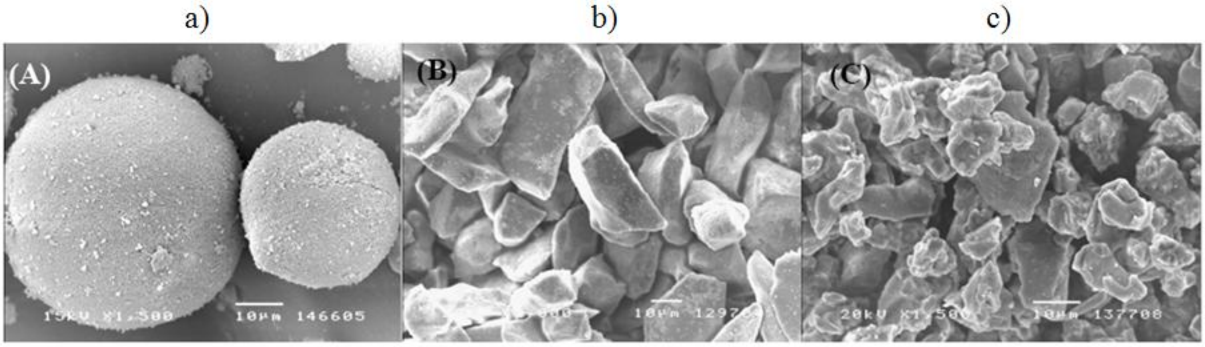

Figure 1.5 *SEM micrographs of powders used to APS: a) agglomerated powder, b) cladded powder and c) fused powder.*

Transportation of powder is realized by carrier gas, typically argon, and its mixtures with hydrogen or a mixture of helium with hydrogen. The powder is then injected by injectors localized internally or externally, what is illustrated in Figure1.3. In Figure 1.6, a complete powder injecting system is presented. Speed of powder particles is very important spraying parameter, which decides on the trajectory of powder particles penetrating the plasma jet. It depends on few variables, among others on carrier gas flow rate, powder feed rate, lengths and diameters of hose and injector. More comprehensive description and calculations can be found elsewhere [20].

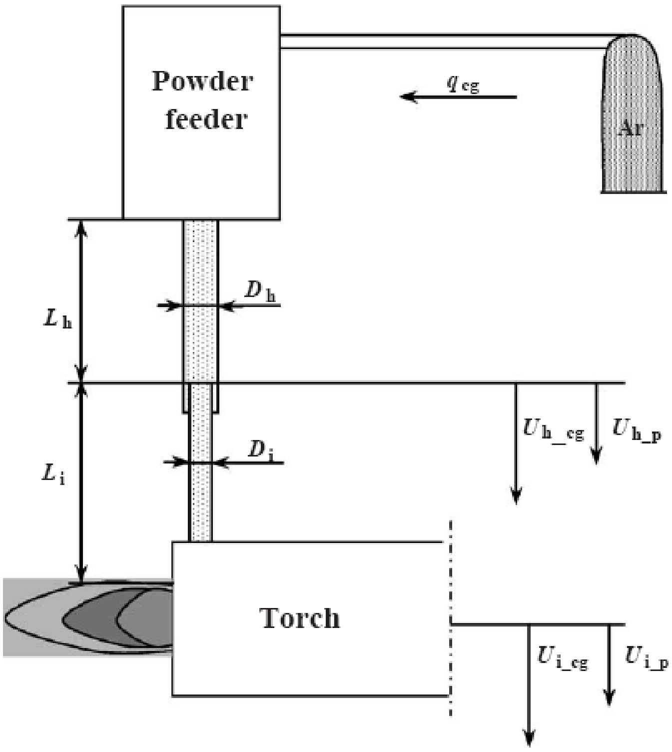

Figure 1.6 *Complete powder injection system [20].*

Since about 10 years the interest in finely structured or nano-structured coatings has been gradually growing up, thus some tries to spray finely structured coatings by using finely sized powders have been done. Unfortunately, radial injection using carrier gas was impossible because small particles had not enough energy to get at the core of plasma jet. Very interesting idea which appeared was the feeding of nano-structured powder axially by using plasma gases. The method of injection turned out troublesome. The powder was deposited on cathode and anode what caused increase in electric arc voltage and the torch had to be cleaned very often. It is why not many papers describing spraying of finely structured powders using APS have been published. That was a direct reason of examination and further modification of classical spraying methods to adopt them to those requirements. New methods which are now of interest are Suspension Plasma Spraying (SPS) and Solution Precursor Plasma Spraying (SPPS)[21].

1.1.9 Solution Precursor Plasma Spraying (SPPS)

The technique has grown up since 1997 so it is relatively new. By this method a variety of novel materials can be produced including some with superior properties [22]. It enables one, among others, to make functional oxide ceramic coatings by starting from solution precursors and directly producing inorganic films. SPPS is a modification of APS by forced interest in finely structured coatings. The modification consisting in a change of sprayed material source (Figure 1.7.), results from transportation problems of fine grained powders (among others the presence of surface forces effects influencing the powder flow).In SPPS, feeding material is a liquid solution. Therefore the method is able to deliver fine splats without the difficulties and limitations connected with fabrication and feeding fine solid powders. SPPS method developed some challenges of producing high-molar solutions and engineering their chemical and physical properties. Schematically, SPPS is presented in Figure 1.7. Commonly used SPPS installations base on DC plasma spraying torches, but some authors indicate that spraying using radio frequency torches seems to be also promising. That method of spraying is called Radio Frequency Precursor Plasma Spraying (RFPPS) [23].

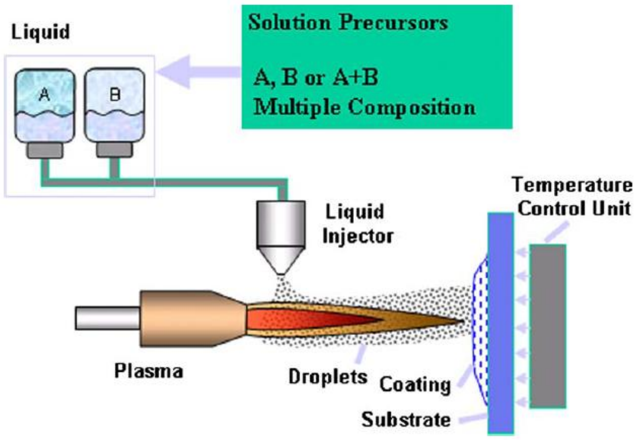

Figure 1.7 *Scheme of SPPS [24].*

The liquid feedstock is prepared as dissolved precursor either in water or ethanol, rarely isopropanol or butanol. Aqueous solutions allow one to prepare higher precursor concentration than organic ones, also they are cheaper to produce and more safe for handle and store. The most important parameters of solutions are: viscosity, surface tension and specific mass. Relationships between those parameters can be found elsewhere [21].

The solutions are usually injected into plasma jet by atomizing nozzle or continuous stream injector and are transported by pneumatic system, where compressed air force out liquid medium or by system using peristaltic pumps, where solution feed rate can be controlled by rotation of pump motors. Optimization of injection parameters have to be carried out precisely to obtain coating with the best properties.

After injection of solutions into plasma jet some effects occur which never exist in the other thermal spraying methods i.e. drops fragmentation and solvent evaporation, then pyrolysis and sintering, melting and crystallization. All listed effects are presented graphically in Figure 1.8.

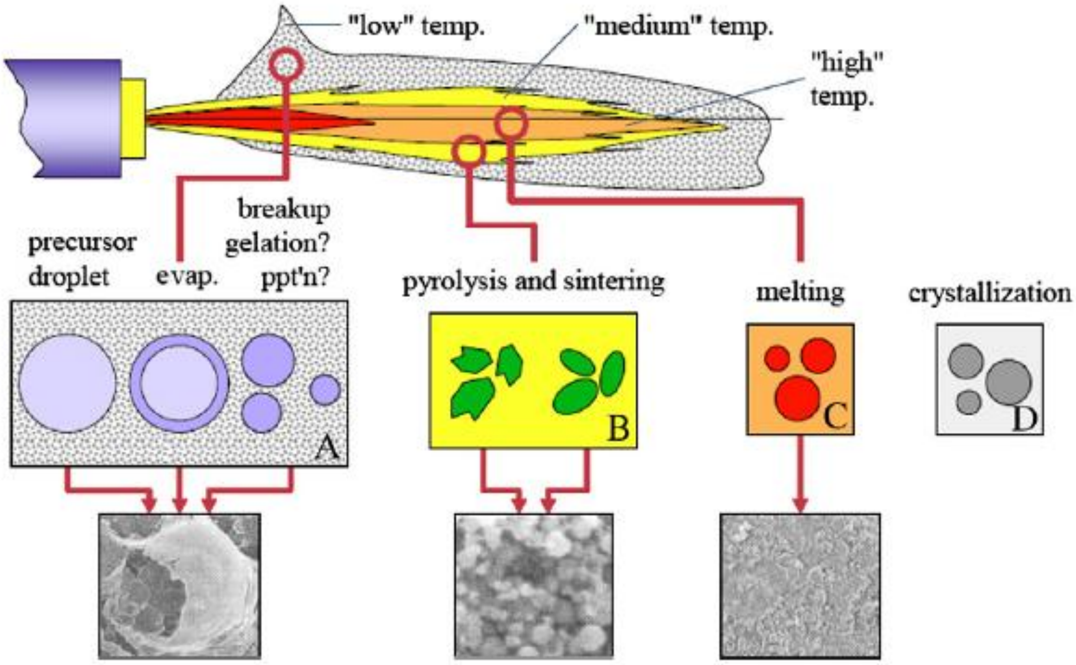

Figure 1.8 *Illustration of effects present at SPPS [25].*

Basu et al. [26] showed different behaviors of solution precursor droplet injected into plasma jet depending on heating rate, droplet size and properties of the dissolved solute and precipitation which directly affect the particle morphologies, from solid particles to hollow spheres and fragmented shells reduced by internal pressurization and particle rupture. Figure1.9.a indicates the behavior of small droplets where an increase in solute concentration throughout the droplet during the evaporation stage results in volume precipitation and affects solid particle morphology. Part 1.9.b concerns the case with larger sized droplets or solutes having low super-saturation limit, what results in shell formation due to surface precipitation. This case can have three different final morphologies, depending on porosity of formed shell. Low porosity shell (case I), where the shell fracture occurs, is produced by internal pressurization due to vaporization of trapped liquid by further heating. Second case (case II) shows the situation where highly permeable shells have sufficient venting what counteract the pressure increase and hollow shells are formed. Third path (case III) takes in consideration impervious shell where not only fragmentation but also secondary atomization from the liquid core may occur. Finally Fig. 1.9.c shows behavior of some precursors where the formed shell may be elastic and subsequent internal pressurization results in inflation and rupture of the shell into collapsed precipitate clumping.

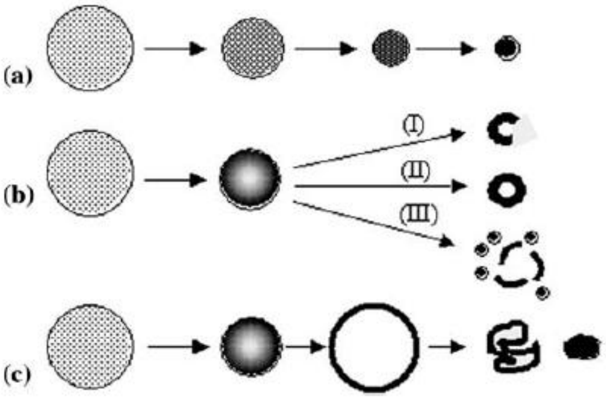

Figure 1.9 *Vaporization and precipitation routes of a solute contained in a droplet: (a) uniform concentration of solute and volume precipitation leading to solid particles; (b) supersaturation near the surface followed by (I) fragmented shell formation (low permeability through the shell), (II) unfragmented shell formation (high permeability), (III) impermeable shell formation, internal heating, pressurization and subsequent shell break-up, and secondary atomization from the internal liquid; (c) elastic shell formation, inflation, and deflation by solids consolidation [26].*

The typical coatings obtained by SPPS as injected liquid spray or a stream containing ceramic precursor salts are applied as Thermal Barrier Coatings (TBC)[24].

1.1.10 Suspension plasma spraying (SPS)

The method used in this thesis will be precisely described in the next chapter.

1.1.11 Hybrid Method of Spraying

In some cases, thermal spraying method and laser spraying can have some disadvantages when used separately. For example, plasma jet is a surface type heat source, it means the particles are usually heated and melted superficially, but in the case of laser as a heat source, absorption of the energy takes place in entire volume of particles (dielectric particles, which sizes are commensurable with the radiation wavelength) – this provides volume heating and complete melting of the spray particles what results in some quality improvement of obtained coating. It was an idea to create hybrid system which is made as a combination of two methods, laser and plasma spraying. In this hybrid system, laser power, required for the spraying process, was substantially reduced and simultaneously the process productivity and material utilization increased.

In Figure 1.10, plasma and laser spraying process as well as hybrid process implemented by coaxial joining of the plasma jet and laser beam using an integrated plasma torch are presented. The first part (Figure 1.10.a) shows the case where particles are accelerated only by plasma jet. In the second case (Figure 1.10.b) the particles are accelerated only by cold gas flow and heated by laser radiation. In the last case (Figure 1.10.c) the particles are accelerated by plasma jet and heated both by plasma jet and the laser radiation.

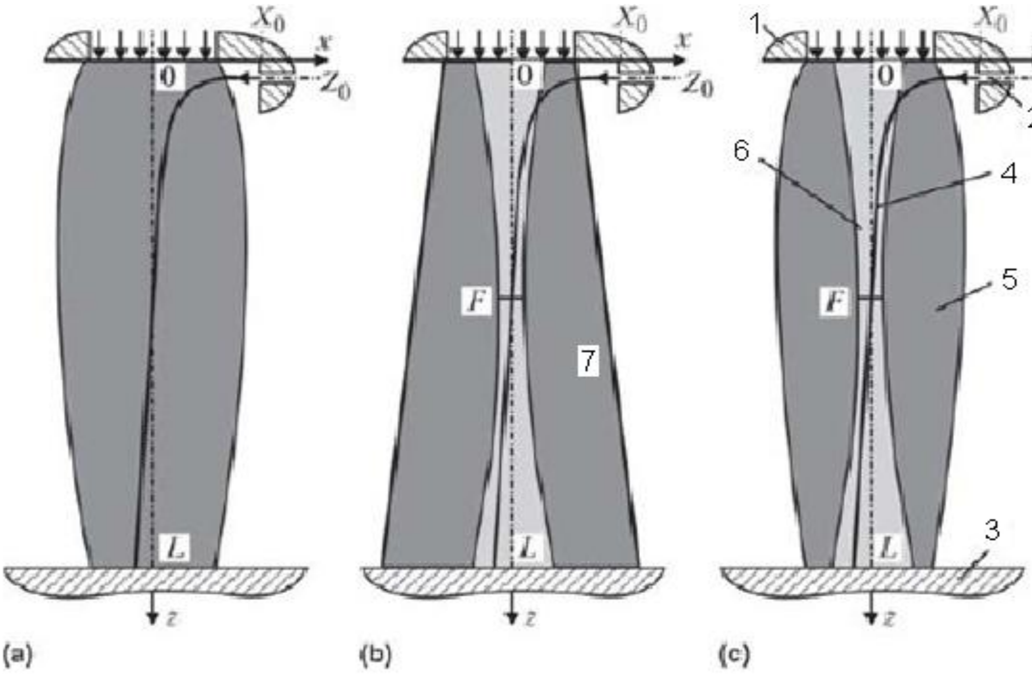

Figure 1.10 *Flow diagrams of (a) plasma, (b) laser, and (c) hybrid laser-plasma spraying processes. 1- plasma torch nozzle; 2- powder injector; 3- substrate (spray distance 0 – L); 4- path of a spray particle; 5- plasma jet; 6- laser beam (F- focal distance); 7- cold gas flow [27].*

1.2 FORMATION OF COATING OBTAINED BY THERMAL SPRAYING

Coatings deposited by thermal spraying are widely used in industry to improve specific service properties of machine components. Thickness of the coatings is usually in the range between 50 µm and a few millimeters. The coatings with thickness below 50 µm are deposited e.g. by SPS and SPPS.

Molten or partially molten particles, which reach the substrate or previously deposited coating, transform into lamellae and can get two shapes of the splats. The first one (Figure 1.11.a) is the shape of pancake, the second one (Figure 1.11.b) is flower shape splat, where existing central part of deformed disc is surrounded by splashed parts of deposited material. This kind of splats is obtained in special conditions of spraying and then more pores occur in final coating. Fukumoto et al.[28] determined transition temperature (T_t), i.e. substrate temperature at which the splat shape changes to a flower like splat from pancake splat for most metallic and ceramic sprayed materials.

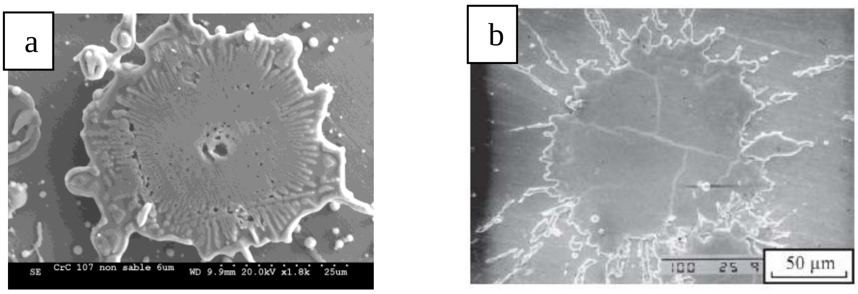

Figure 1.11 *Splat formed as: a) pancake b) flower like.*

Splat formation mechanisms are in good agreement with adhesion/cohesion characteristics of coatings manufactured on rough surfaces [3,29]. Effect of roughness influence on the splat shapes was widely examined by computer simulation by Raessi et al. [30].

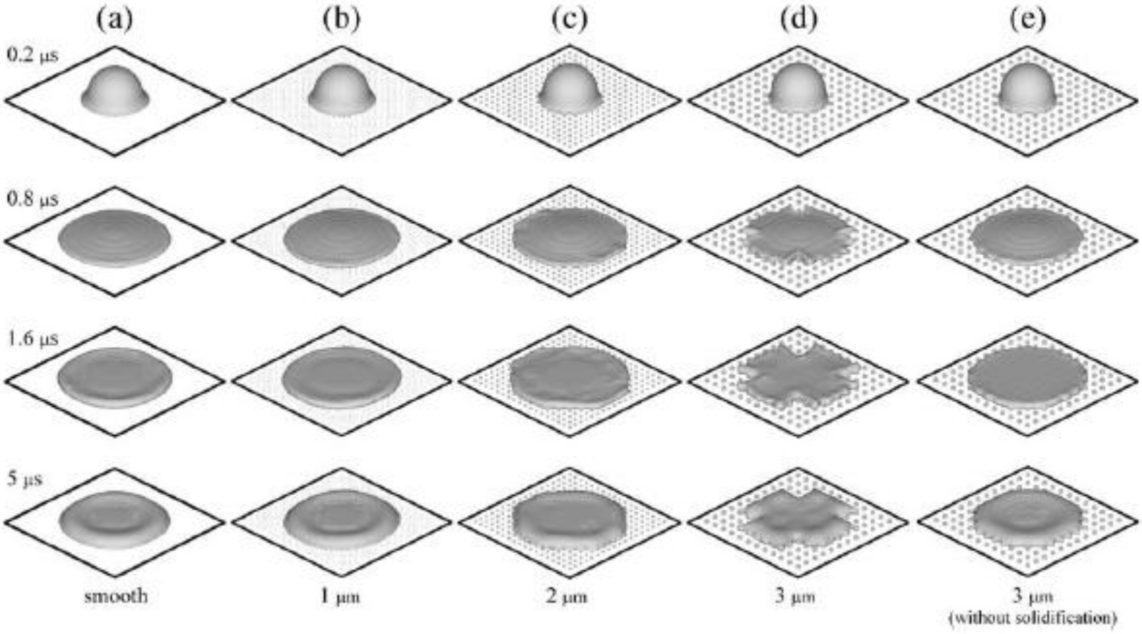

Figure 1.12 *Computer-generated images of 40 µm diameter alumina droplets at 2055^{0}C impacting with a velocity of 65 m/s onto alumina substrates initially at 25^{0}C, characterized by different values of surface roughness [30].*

Flattening results shown in Figure 1.12 in the cases a) and b) do not differ considerably, but for the roughness value 2 and 3 µm the changes in splat shapes are substantial. Especially in the case d) blocking of splat splashing in the direction of 45^0 is demonstrated and propagation of liquid splat follows along perpendicular roughness lines. For comparison, the case without solidification is presented on e) series, for the same roughness i.e. 3 µm. As conclusion Raessi et al.[30] presented a relationship of increase in roughness up to a certain value with the splat diameter increase.

In the moment when particle gets transformed into splat, rapid cooling and solidification occurs. Solidification starts however before complete flattening of impinged particle and lasts for few microseconds. During the process, a formation of metastable phases of deposited material is possible. For example - anatase phase when titania coating is sprayed. Pasandideh-Fard [31] proposed schematic picture showing the impact of a 60 µm diameter molten nickel particle at 1600 °C landing with a velocity of 73 m/s on a stainless steel plate initially at a temperature of 290 °C - stages of solidification during flattening are shown in Figure 1.13.

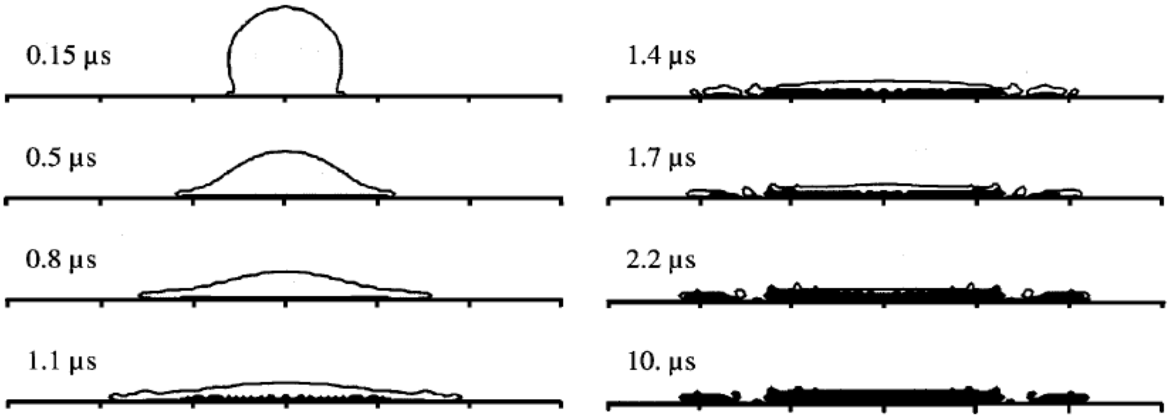

Figure 1.13 *Cross-section view through flattening particle. Black shows the solidified portion of the droplet and white represents liquid [31].*

To improve a contact between coating and substrate some authors showed that investigation of wettability should be carried out. Results of this experiment are shown in Figure 1.14 where packing of the pores in the case of poor or good wettability is presented [32].

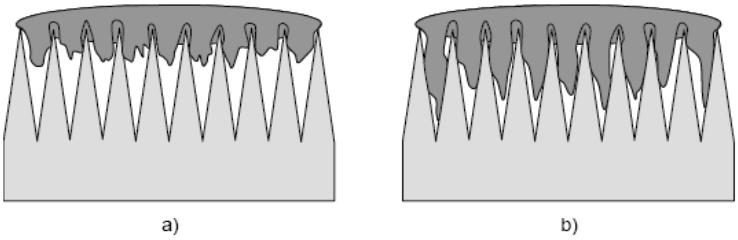

Figure 1.14 *Scheme of the contact between lamellae and the surface asperities at a nanoscale a) poor wettability, b) good wettability [32].*

Adhesion of the coating can be improved by substrate preheating. Fauchais et al.[33] showed that the preheating greatly influence splat adhesion and cohesion. In this case, adhesion is improved because thin oxide layer emerges on the substrate surface (when metallic substrate is taken into consideration) and evaporation of absorbed superficial water takes place what enhances wettability. Some micrographs are presented in Figure 1.15 where sprayed samples were made on the substrate at room temperature and on the substrate preheated to 600K.

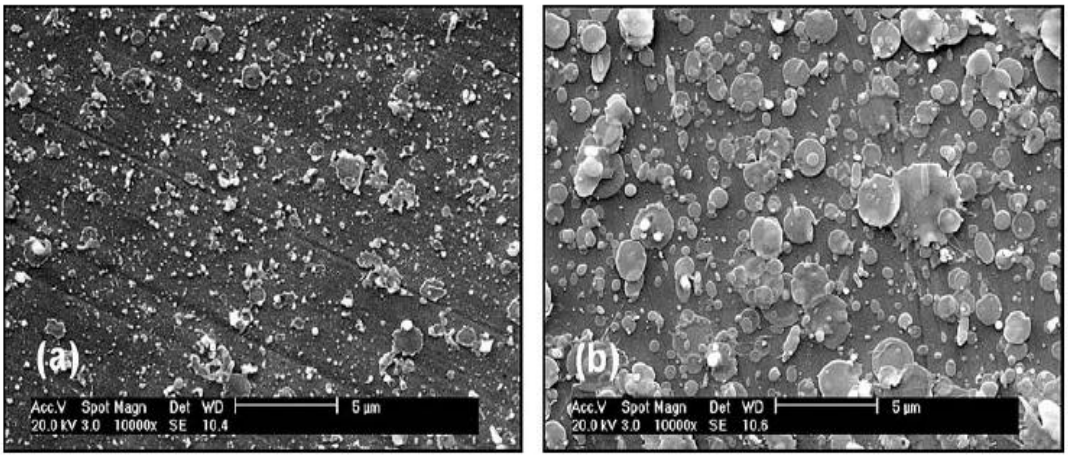

Figure 1.15 *SEM micrographs of zirconia splats and particles sprayed on 304L stainless steel substrate (a) at room temperature and (b) preheated at 600K [33].*

Li et al. [34] studied the case of impact of a molten droplet characterized by melting point much higher than the substrate. Such temperature difference can result in partially melting of the substrate underneath the central part of formed splat. The melting of the substrate surface to a certain depth alters the flow direction of the droplet. The significant change of fluid flow direction leads to detaching of fluid from the substrate. Consequently, splashing occurs during the droplet-spreading process. This type of splashing cannot be suppressed through substrate preheating. The results indicated that the flattening of a spray droplet is significantly influenced by localized melting of the substrate by the droplet impact. Cracking occurring in the molybdenum splat, deposited on the steel substrate was caused by restraining of the splat contraction during cooling and low plasticity of the solidified splat material. This phenomenon is shown in Figure 1.16.

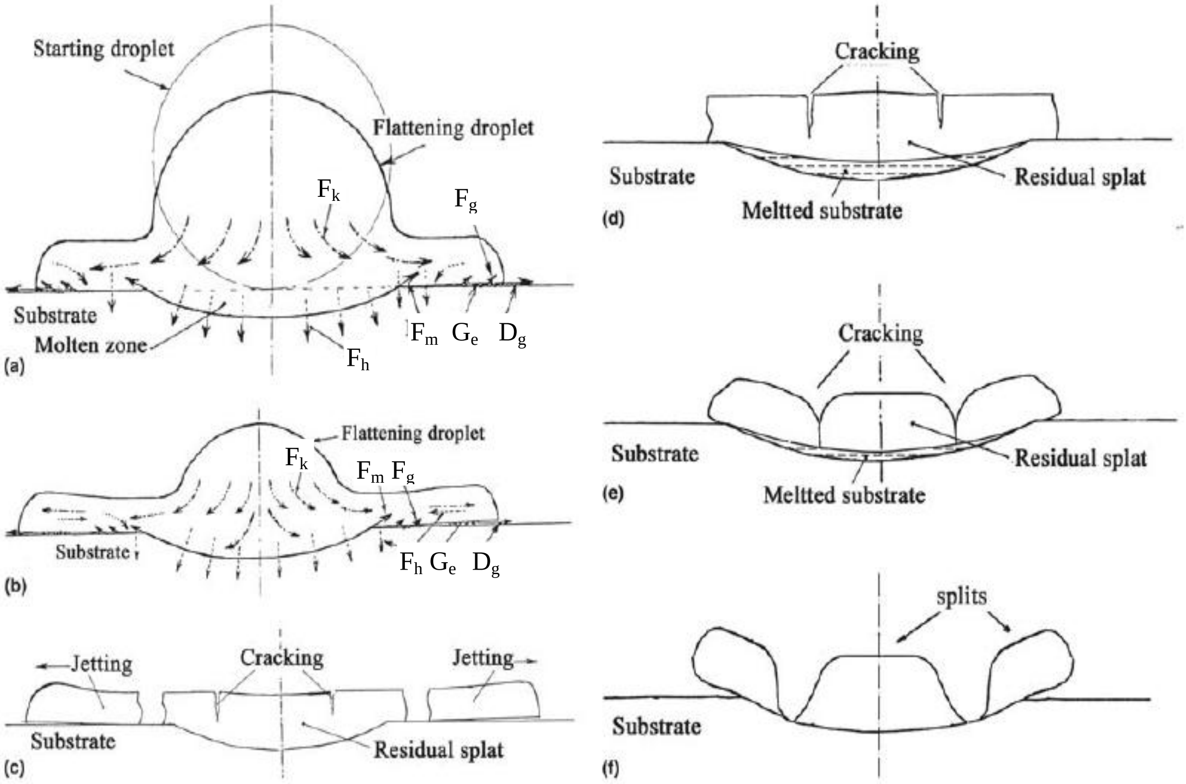

Figure 1.16 *Schematic diagram of droplet impact inducing the melting of a substrate and the flattening behavior of droplet resulting in the formation of a splat with splits. (a) and (b) indicate the early stages of flattening, resulting in the melting of the substrate by the impacting droplet. When flattening completes (c), the splashing occurs, driven by the inertial force of the rapidly flowing fluid along direction* F_m*. Cracking occurs when the surface layer of the splat is solidified, as shown in (c) and (d). The displacement by floating of the cracked splits on low-melting-point liquid film results in the formation of splitting of the residual central splat (e) and the final splat (f) [34].*

Stress in the coating strongly depends on the kind of used substrate. The best case is when the substrate and coating have the same coefficients of thermal expansion (CTE) and during cooling of the coating the same values of shrink. If the substrate has higher CTE it automatically generates compressive stress in the coating during cooling. In the case when coating has higher value of CTE, tension stress appears. Stresses in the coating can deteriorate adhesion of the coating.

Very important thing for coating formation is to understand the splat curling up during flattening what also results in poorer adhesion of the coating. Curling up is caused by some factors i.e. mismatch of thermal expansion coefficients what generates stresses described above, surface tension of liquid splat, surface roughness and remelting. Xue et al.[35] assumed that splat curling up is entirely caused by shrinkage of splats as they cool down from a high initial temperature to the substrate temperature. When the bottom area of the splat has good adhesion it can’t contract but the upper surface shrinks curling up the edges. The angle of curling up increases with area of the splat bonded to the substrate and decreases with substrate temperature increase. Examples of curling up of the splats are shown in Figure 1.17.

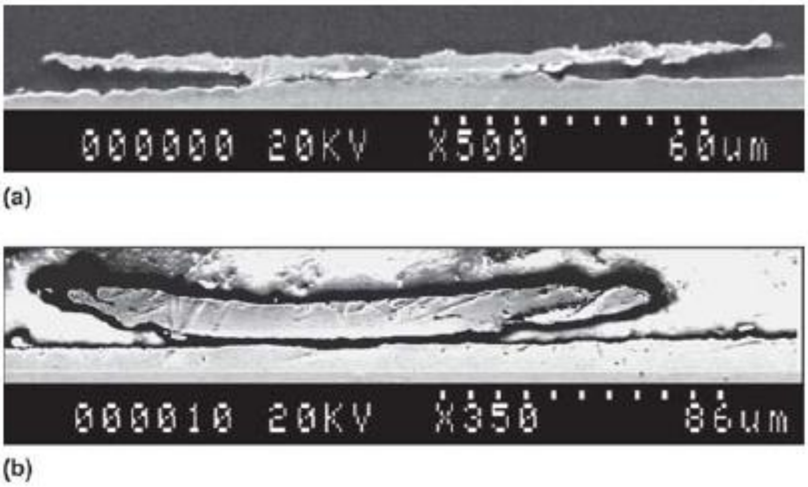

Figure 1.17 *Cross-sections of nickel splats on a stainless steel 303 substrate with initial surface temperature of 400^0C: a) 38% of the splat radius bonded: b) 49% of the splat radius bonded [35].*

Surface roughness is an important parameter in splat-solidification studies , because the presence of roughness promotes substrate remelting in the conditions under which smooth surface would not remelt [35].

1.3 MICROSTRUCTURE OF THERMALLY SPRAYED COATINGS

Microstructure of thermally sprayed coatings fully depends on spraying parameters which must be optimized to obtain a coating with required properties. The morphology of the first layer of splats plays an important role for further splat layers generation and generally it influences the coating microstructure. Growing of the coating is inherently burdened with defects and discontinuities caused by splats splashing and solidification mechanisms. This is why classification of typical defects and their reasons have to be determined. Figure 1.18 presents inhomogeneous microstructure of thermally sprayed coating with description of its defects.

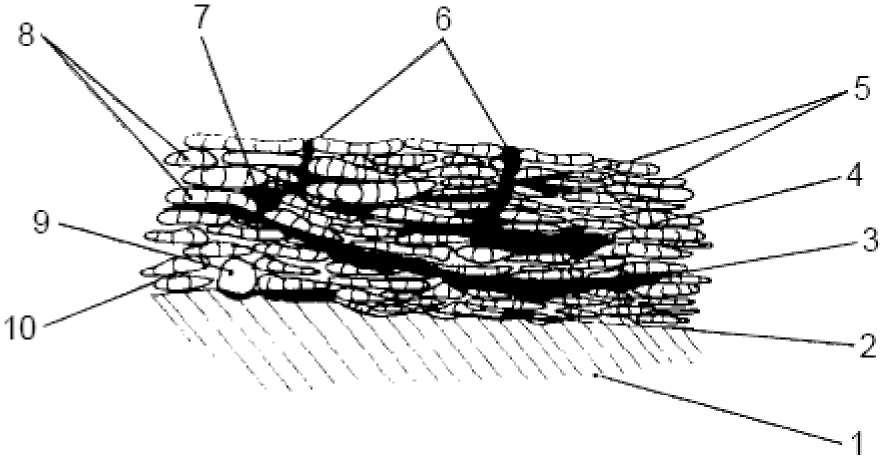

Figure 1.18 *Cross-section of a thermally sprayed coating with all microstructural defects: (1) substrate; (2) weak contact to the substrate; (3) crack resulting from one-torch-pass stresses; (4) crack resulting from relaxation of vertical stresses; (5) lamellae solidified with columnar crystals; (6) crack resulting from relaxation of in-plane stresses; (7) large pore (a few micrometres in size); (8) well-deformed lamellae; (9) powder particle that remained solid upon spraying; (10) small pore (submicrometre size)[1].*

Microstructure of the coating also depends on phase composition which in turn depends on initial powder composition, deposition parameters or, if used, post treatment. Pawlowski listed four factors influencing phase composition [1]:

- ✓ high temperature – which may result in partial evaporation of material component when melting temperature is exceeded,
- ✓ interaction of sprayed material with plasma gases – then reduction or decarburation reaction may occur. There are some examples when this phenomenon is used for improving the properties of sprayed material [36],
- ✓ nucleation and solidification – depending on nucleation energy formation of non-stable phases may occur, solidification depends on temperature of the splat,
- ✓ rapid cooling of lamella.

For more predictable coating deposition the knowledge of phase diagrams is recommended. This is shown as example on HA phase diagram (Figure 1.19).

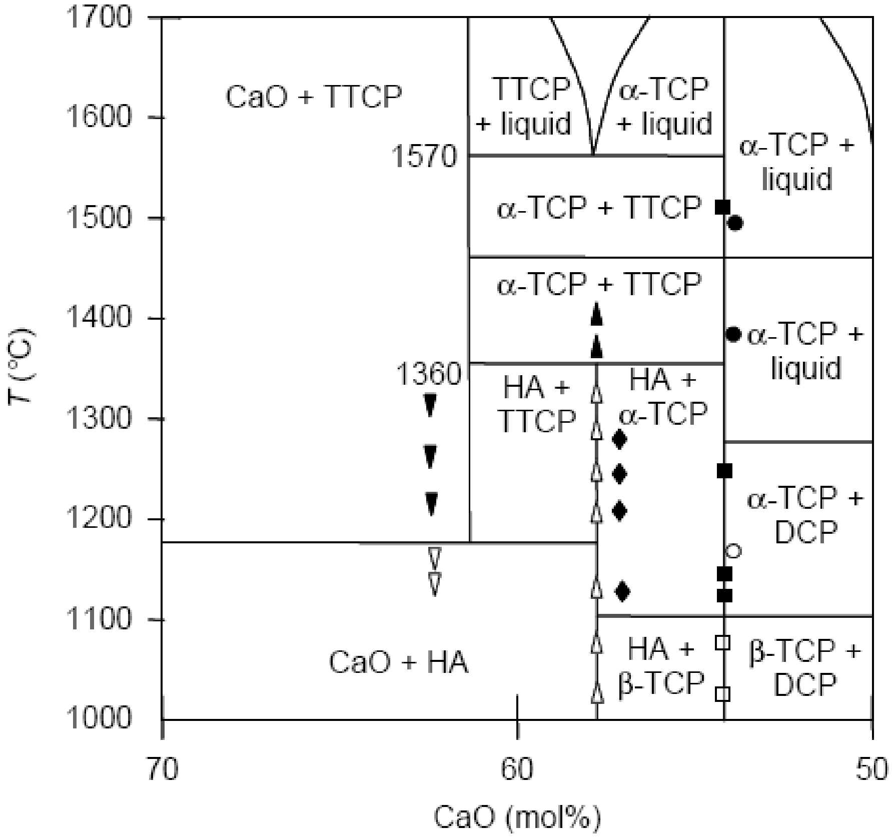

***Figure 1.19** Part of the phase diagram of CaO–P_2O_5 [1].*

Dyshlovenko et al.[37,38] on the basis of a phase diagram modeled HA particle during atmospheric plasma spraying. The presence of different phases after solidification was explained by rapid cooling of particle and freezing liquid phases and high temperature phases to form of amorphous phase.

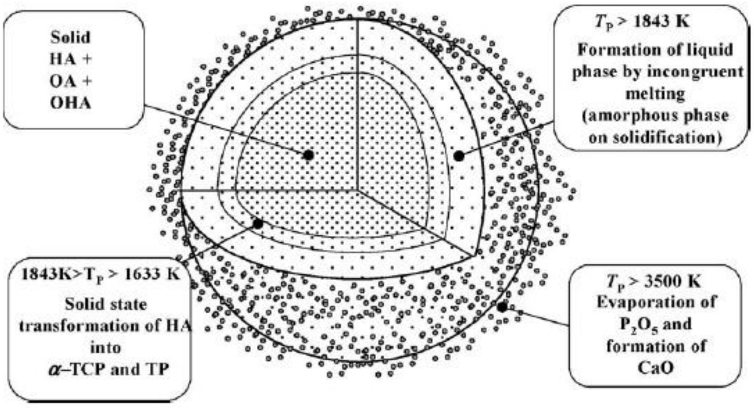

***Figure 1.20** Different phase zones present inside HA particle upon impact [37].*

Heimann et al.[39,40] showed hydroxyapatite phase decomposition after injecting into plasma jet using APS. This process is presented as chemical four-step process:

Step 1: $Ca_{10}(PO_4)_6(OH)_2 \rightarrow Ca_{10}(PO_4)_6(OH)_{2-2x}O_x\square_x + xH_2O$
(hydroxyapatite) (oxyhydroxyapatite, OHAp)

Step 2: $Ca_{10}(PO_4)_6(OH)_{2-2x}O_x\square_x \rightarrow Ca_{10}(PO_4)_6O_x\square_x + (1-x)H_2O$
(oxyhydroxyapatite, OHAp) (oxyapatite, OAp)

Step 3: $Ca_{10}(PO_4)_6O_x\square_x \rightarrow 2Ca_3(PO_4)_2 + Ca_4O(PO_4)_2$
(oxyapatite) (tricalcium phosphate)+(tetracalcium phosphate)

Step 4a: $2Ca_3(PO_4)_2 \rightarrow 3CaO + P_2O_5$

Step 4b: $Ca_4O(PO_4)_2 \rightarrow 4CaO + P_2O_5$

(the squares in the formulae of oxyhydroxyapatite and oxyapatite refer to lattice vacancies in the OH positions along the crystallographic c-axis in the structure of hydroxyapatite. In the completely dehydroxylated oxyapatite (OAp) a chain of oxygen ions exists parallel to the c-axis each one followed by a vacancy ($x = 1$)).

They also observed that HA particles injected into a plasma jet at a different water partial pressure differ in terms of occurrence and quantity of decomposed phases.

Another example concerns the influence of powder inhomogeneity on the microstructure of titanium oxide coating. It considers the case when single powder particles have different phase composition. During spraying TiO_2 particles may be slightly reduced what would result in inclusion Magneli phases Ti_xO_{2x-1} into the coating [41].

1.4 MATERIALS USED FOR SPRAYING

1.4.1 Hydroxyapatite

Hydroxyapatite is present in nature as mineral compound within family of apatites. It is also inorganic component of bones and teeth. Chemical formula of HA is $Ca_{10}(PO_4)_6OH_2$.
The most common applications of hydroxyapatite coatings find place in medicine because of their advantageous biocompatibility [42,43]. Unfortunately, this material in bulk has too weak tensile strength, low fatigue resistance, elastic modulus mismatch and resultant stress shielding what excludes the possibility of its use for prosthesis production. Some thermophysical constants of bulk hydroxyapatite were listed by Dyshlovenko et al.[38] and are presented in Table 1.2. Therefore, HA is used as a coating on metal implants for orthopedic and dental applications. The most popular method used for deposition of this material is atmospheric plasma spraying. In 2006, in USA and Europe more than 1 million hip and knee prosthesis were produced and the number is still growing [39].Hip and knee prosthesis are shown in the Figure 1.21. Generally the parts of prosthesis which are inside bone or directly abut on bone are covered with HA by APS [44,45,46]. Recently some authors applied the method of HVOF to deposit the HA coatings, which also seem to have good biological properties[43]. Another method which was applied for HA coatings production is

pulsed laser deposition (PLD)[47,48]. To date because of corrosion and dissolution of the coating in human body, the prosthesis must be replaced every 10 – 15 years. Some authors suggest that electric field applied to hydroxyapatite coating may simulate grows of osseous tissue [40,**49,50**].

Pyda et al. showed the way to reinforce the polycrystalline hydroxyapatite by inclusions of zirconia. This inclusions result in increase of the bending strength value about 80% i.e. to the approximately 180MPa. The inclusions were made by the hot pressing method of mixture nanostructured powders of HA and pure ZrO_2 [51].

Good quality hydroxyapatite coatings applied in prosthetics should have at least 95% of pure crystalline hydroxyapatite.

Table 1.2 Physical data of HA [38].

CONSTANT	VALUE
Heat of melting [kJ/mol]	15.5
Melting point [K]	1843
Heat of evaporation [kJ/mol]	45.24
Boiling point [K]	3500
Molecular mass [kg]	$1.668x10^{24}$
Density [kg/m^3]	3156
Thermal expansion coefficient [1/K]	$13.3x10^{-6}$

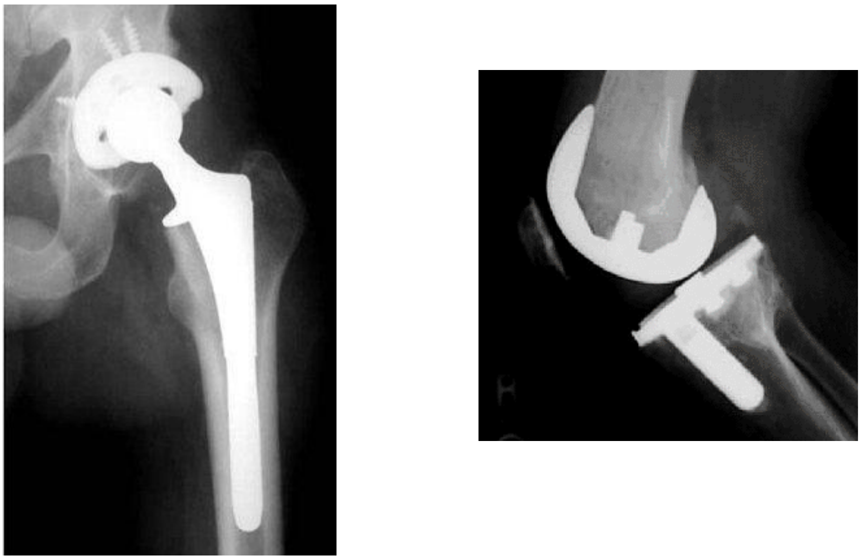

Figure 1.21 *X-ray photo of the hip and knee prosthesis.*

1.4.2 Titanium oxide

Titanium dioxide (titania) naturally occurs in three phases: tetragonal rutile, anatase and brookite. Its basic thermophysical constants are listed in Table 1.3. Titania is stable, nontoxic and dielectric. During plasma spraying of rutile, decomposition to anatase phase occurs [41,**52**,53]. The typical application is pigment in white paints and paper whitening agent. Few years ago very interesting property was discovered i.e. photocatalytic ability. This is why it is widely used in photocatalytic degradation of harmful and toxic organic pollutants [9]. In other applications titania is used as a base or component of biocompatible coatings and as load-bearing component in composites. Recently titania has been applied in electronics in dye-sensitized solar cells and as field emitters. Titanium oxide is also used in optics as optical filters [54] as well as coating on self-cleaning glass.

Table 1.3 Physical data of TiO_2 [55].

CONSTANT		VALUE
Density	[g/cm^3]	4
Modulus of Rupture	[MPa]	140
Compressive Strength	[MPa]	680
Poisson’s Ratio		0.27
Fracture Toughness	[MPa/m$^{1/2}$]	3.2
Shear Modulus	[GPa]	90
Modulus of Elasticity	[GPa]	230
Microhardness (HV0.5)		880
Resistivity (25°C)	[Ω·cm]	10^{12}
Resistivity (700°C)	[Ω·cm]	$2.5x10^4$
Dielectric Constant (1MHz)		85
Dissipation Factor (1MHz)		$5x10^{-4}$
Dielectric Strength	[kV/mm]	4
Thermal Expansion Coeff.(RT-1000°C)		9×10^{-6}
Thermal Conductivity (25°C)	[Wm/K]	11.7

Nano-structured gradient TiO_2 and HA coating obtained by suspension plasma spraying was deposited onto titanium substrate, and it was widely examined by Tomaszek [56,57]. Gradient of coating composition was obtained due to application of suspension feeding system with two feedstocks. Changing of particular suspension feed rates from 25 to 0 g/min to 0 to 25g/min was programmed (TiO_2 to HA suspension respectively). The suspension feed rate vs number of torch passages is presented in Figure 1.22.

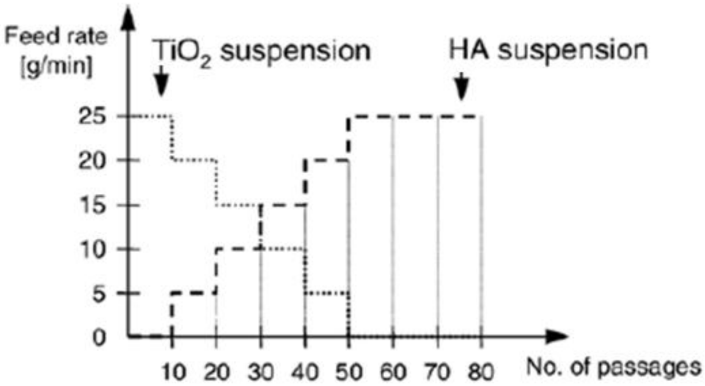

Figure 1.22 *Feed rate of HA (---) and TiO_2 (···) suspensions during SPS process [57]*

Tomaszek investigated also emission properties of TiO_2 [58]. Porosity of the coating obtained by SPS is advantageous because extraction of electrons can occur from each conic section. Further emission experiments were done by Czarczyński and Znamirowski [59,60]. It made possible to build the first field emission display (FED) by Znamirowski and Ladaczek [61], where plasma sprayed titania were used as matrix of electron emitters. The structure of lighting segment is shown in Figure 1.23.

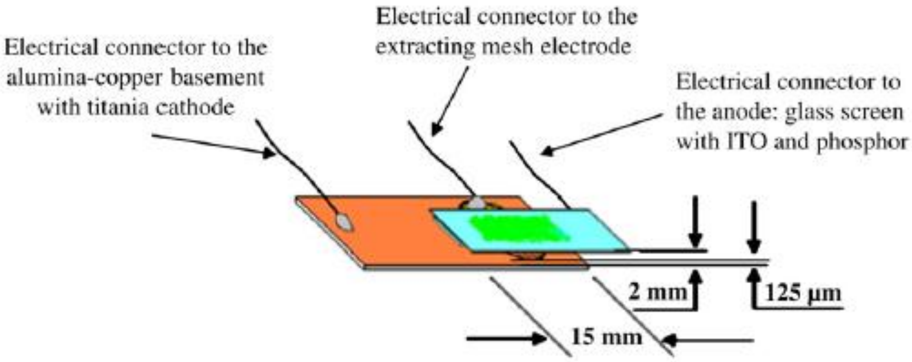

Figure 1.23 *Sketch of the lighting segment structure [61].*

2 EXPERIMENTAL

2.1 SUSPENSION PLASMA SPRAYING (SPS)

SPS is a modification of the APS process in which sub-micrometer particles are put into suspension, instead of using dry powder stream. This modification made possible to obtain much finer grains and pore sizes as well as dense and thin ceramic coatings [62]. The fact that the new method was elaborated at low costs due to utilizing existing spraying installations was its unquestioned advantage. Schematically SPS is shown in Figure 2.1.

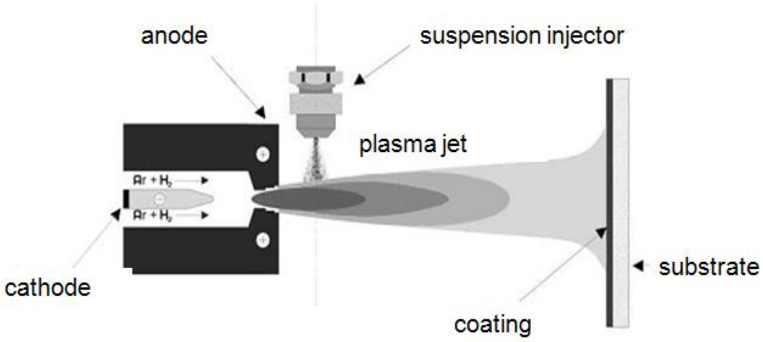

Figure 2.1** Sketch of SPS with external radial injection of the suspension **[63].

SPS coatings can be applied e.g. to obtain:

- HA coatings used in prosthetics;
- TiO_2 coatings used as photovoltaic elements[64], field emitters, intermediate layers for prosthesis and photocatalytic coatings [65,66];
- YPSZ thermal barrier coatings (TBC), YSZ components for solid oxide fuel cells (SOFC).

Spraying distance i.e. the distance between torch nozzle exit and substrate in SPS is much shorter than in APS (4-6cm instead of 8-12cm). Mainly it is caused by more intensive plasma jet cooling by injected suspension. This parameter must be carefully selected because, on the one hand, when small particles are sprayed with too long distance then evaporation of the particles before they reach the substrate may occur, on the other hand too short distance may cause not complete evaporation of solvent and/or partial melting of the substrate.

Fauchais et al.[67] presented a history of suspension particles injected into plasma jet as it is shown in Figure 2.2. Two different suspensions were taken into consideration. First case (Figure2.2 a) concerned suspension made from powder with particle size distribution from tens to hundreds of nanometers, (usually made by chemical route), which had tendency to agglomerate within suspension droplet. The droplet in the plasma could explode after solvent evaporation what would result in a forming of aggregate pieces which could have been molten and next form splats. Explosion can also produce single particles which may evaporate and not participate in the coating formation. Second type of suspension (Figure 2.2 b) includes powder after attrition milling with size distribution from hundreds of nanometers to tens of micrometers. Molten particles are often formed after solvent evaporation and next form splats on the substrate.

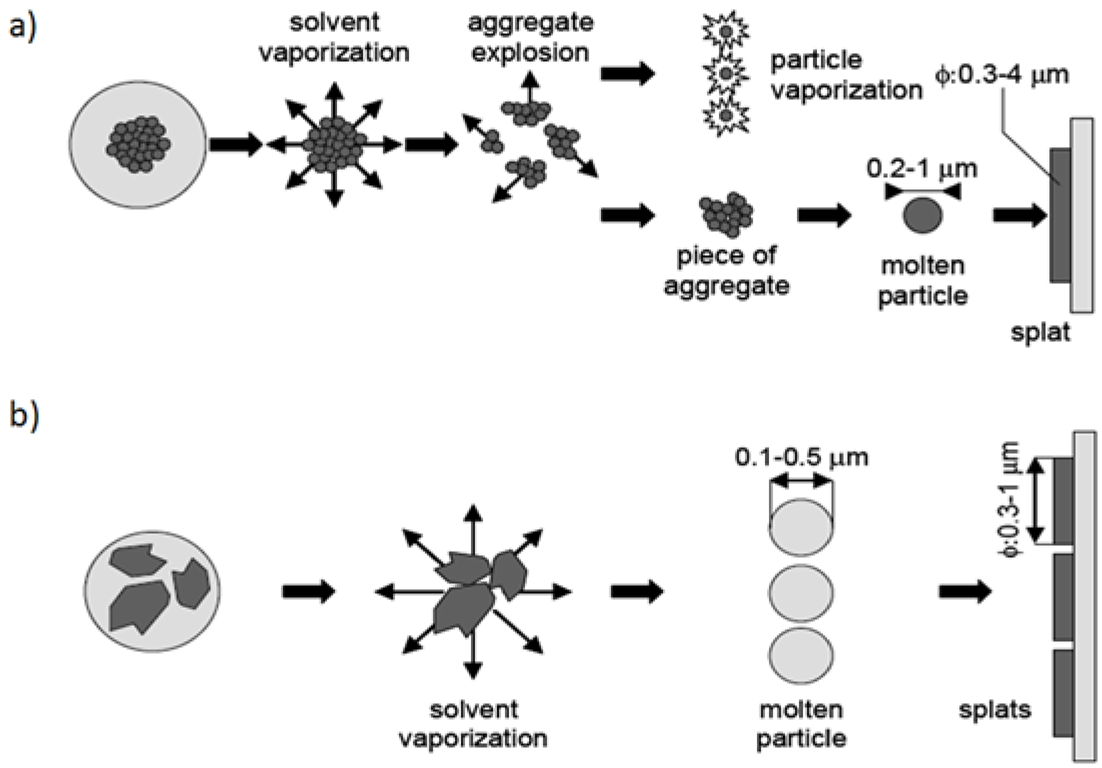

Figure 2.2 *Mechanism of suspension droplet treatment in a plasma jet; a) nanosized particles, b) attrition milled particles [67].*

2.2 SUSPENSION PREPARATION

Knowledge about suspension preparation details and results of its properties investigation is necessary to full understanding their influence on coating properties [68, 69]. Suspensions are made using fine sized powders and solvent. As it has been already mentioned, the powders used for SPS are usually prepared by two ways: chemical route or attrition milling. The most often used solvent is water and/or ethanol, rarely methanol or isopropanol. Alcoholic suspension is used to reduce cooling and separation of plasma jet. A polyvinyl alcohol (PVA) is sometimes added to the suspensions to tailor its viscosity. PVA also improves the dispersion and stability of the suspension [70].

The suspensions can be prepared by adding a dispersant which limits agglomerate sizes. The influence of the dispersant on suspension stability was examined by Tomaszek [56]. In some investigations made by the author some undesirable effects of dispersant with ethanol used as a solvent for suspension production occurred what in consequence excluded the possibility of using dispersant for improving suspension stability.

The problem of sedimentation of the suspension was partially solved by using electromagnetic or ultrasonic stirring. Time of suspension sedimentation should be checked before spraying due to later sedimentation of the powder in the feeding conduit. In consequence, decreasing of flow rate and/or decreasing of injector nozzle diameter can occur. The size distribution and morphology of the powder must be also carefully selected [3]. Some scientists claim that stability of suspension seems to be enhanced by increasing the solid content [71].

Rampon et al. [70] showed (Figure 2.3) how the value of gas-to-liquid mass ratio (GLR) of low-viscosity suspension influences the spray shape pattern. Decreasing GLR from 0.6 to 0.15 shrinks spray shape pattern and makes it more converge. For suspension defining Weber number was calculated**.** It is a dimensionless value useful for analyzing fluid flows where an interface between two different fluids occurs. Weber number calculations were made according to the formula:

$$We = \frac{\rho v^2 l}{\sigma} \qquad (2.1)$$

Also Ohnesorge number which relates the viscous and surface tension force for the suspension was calculated, according to the formula:

$$Oh = \frac{\mu}{\sqrt{\rho \sigma l}} = \frac{\sqrt{We}}{Re} \qquad (2.2)$$

Reynolds number must be known before Ohnesorge number calculations will be done. It gives information about the ratio of inertial forces to viscous forces and, consequently, it quantifies the relative importance of these two types of forces for given flow conditions. The calculations were performed using the following formula:

$$Re = \frac{\rho_g d_p (v_g - v_p)}{\eta_g} \qquad (2.3)$$

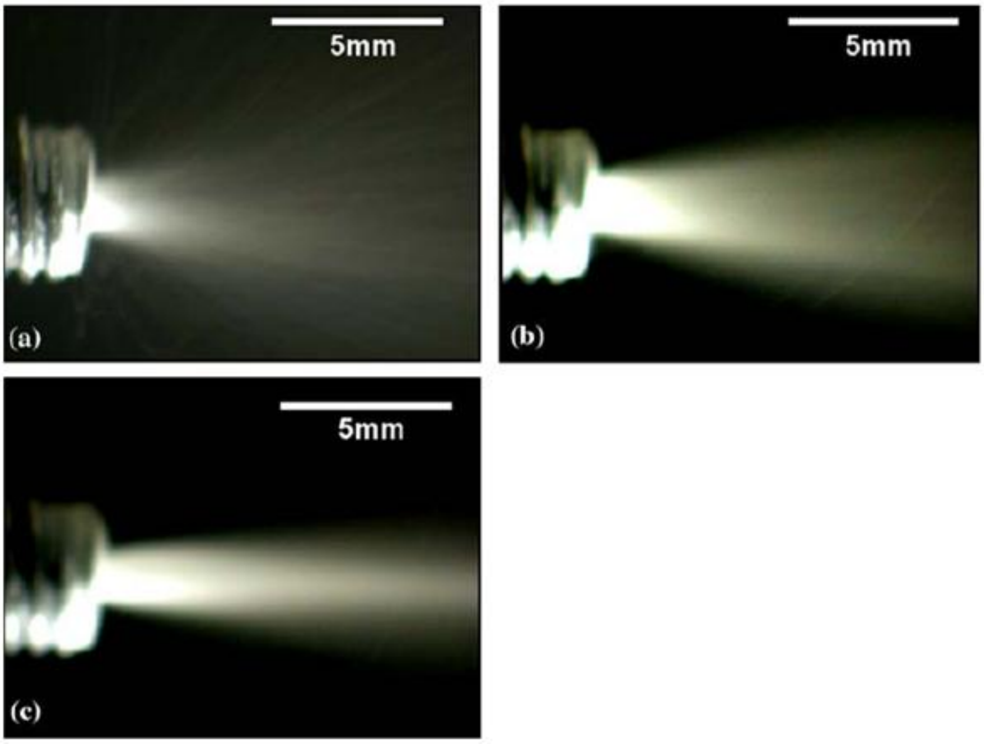

Figure 2.3 *Spray patterns photographs of low-viscosity Y-PSZ suspensions (Oh=0.025 and We = 6) for different GLR values: a) 0.6, b)0.3, and c) 0.15 [70].*

2.3 DROPLET INTERACTION WITH PLASMA JET

Droplet fragmentation and solvent evaporation occurs when liquid droplets get into DC plasma jet [72].

Fauchais et al. [21] defined three zones identified within plasma jet where injected suspension droplets were subjected to different phenomena:

- plasma jet core (temperatures >8000K) (corresponding to zone III in Figure 2.4) where droplets can take over the highest heat and momentum transfer
- plasma jet plume (temperatures from 3000K to 6000K)(corresponding to zone II in Figure 2.4) where droplets can take over heat and momentum drastically reduced in comparison with the ones in plasma jet core
- the plasma fringe (temperatures below 3000K)(corresponding to zone I in Figure 2.4) where a stream of droplets can be fragmented but heat treatment is insufficient

Gell et al.[24] showed similar to Fauchais et al.[21] model for SPPS (Figure 2.4). Injected solution precursor droplets penetrate plasma jet, and then droplet momentum and location of injection determine which region of plasma jet is reached by the droplet and this directly determines time-temperature history of the droplet.

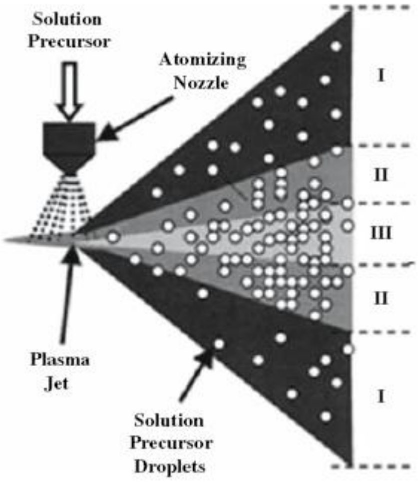

Figure 2.4 *Regions of plasma jet; I - cold outer region, II - moderate inner core, and III - the hot inner core [24].*

Some scientists described droplet fragmentation using a simple force balance (with assumption that the drag force is equal to the surface tension force). Fauchais et al. [67] and Fazilleau et al. [73] stated that the fragmentation time of large droplets (diameter from range 50 to 300μm) was much shorter (few microseconds) than their vaporization time (2 to 3 orders of magnitude). It was concluded that the vaporization can be neglected in fragmentation calculations. For example, Fazilleau et al. and Fauchais et al. considering Ar-H_2 plasma, showed that the fragmentation of initial droplets (average sizes about 225 μm) takes place in the jet fringes, before they reach plasma jet axis (fragmented droplets sizes about 1μm). This fact explains why plasma jet can be divided into 2 parts close to the torch nozzle exit (5mm) and is again joined at the distance of 15mm downstream. This phenomenon is presented in Figure 2.5 in form of spectroscopic measurements. It is interesting that reduction of plasma jet core temperature is only 2000K at water injection equal to 20ml/min. Increasing water feed rate to 50ml/min caused more intensive cooling down of plasma jet. Using ethanol which has lower heat of evaporation caused less intensive cooling of plasma jet.

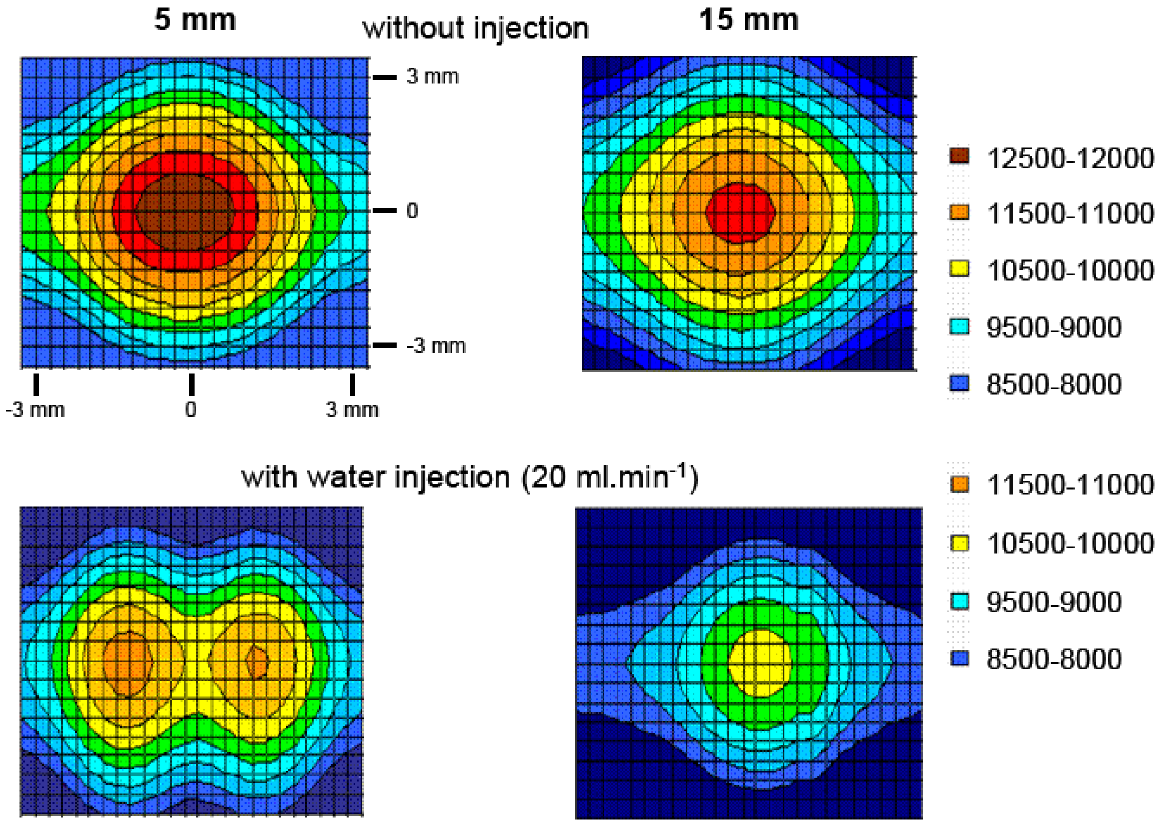

Figure 2.5 *Results of spectroscopic measurements with and without water injection (Ar –H_2, DC plasma jet 45-15 SLPM, average specific enthalpy of 17.9 MJ·kg^{-1})[73].*

2.4 SUSPENSION INJECTION

Suspension injecting system has a great influence on final coating properties. The kind of injector, its position, angle, feed rate of injected suspension are the basic parameters of the injecting system [74,75].

Feeding of suspension to the injection nozzle is very important - feeding system has to fulfill some requirements when it is applied as the suspension feeding system. The most important parameter is pressure of suspension delivered to the injection nozzle. At present, three types of transportation systems are used, i.e. suspension feeder with peristaltic pumps, suspension feeder with perfusion pumps and pneumatic feeding system (the easiest to realize). Feed rate of the feedstock material is controlled by rotation of the pump motors in the first two systems and by the pressure of the gas which ‘push out’ the suspension in pneumatic system. In the Figure 2.6, two types of delivery systems used in plasma spray laboratory in ENSCL are shown [76,77].

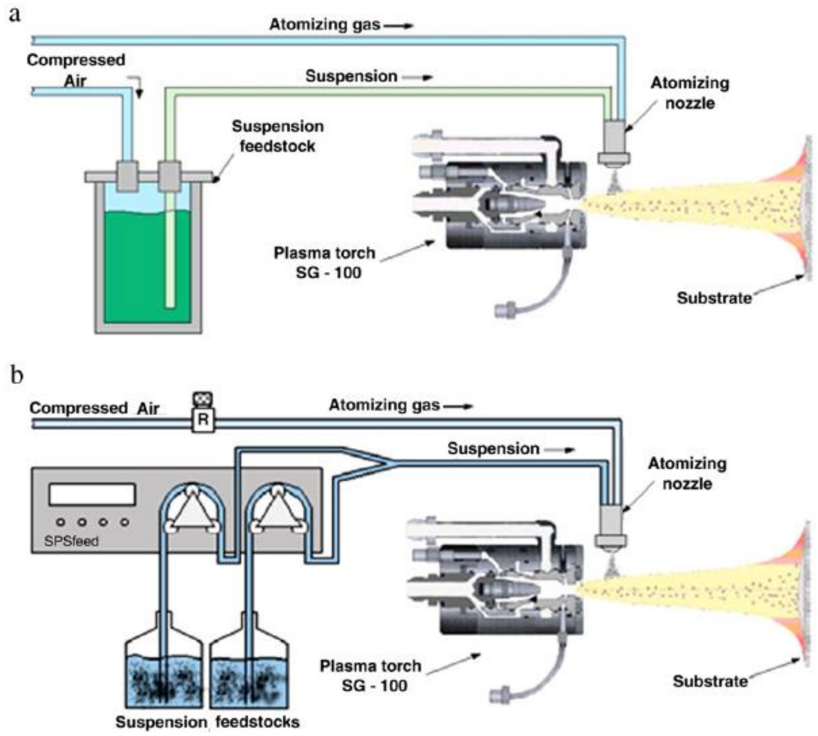

Figure 2.6 *Two systems of suspension delivery with atomizing nozzle used in ENSCL: a) pneumatic system, b) system with peristaltic pumps [76,77].*

Injecting techniques can be classify in two main groups:

- **Pneumatic injection** where liquid is atomized by gas (mostly argon or air) what results in stream of suspension droplets with wide diameter range - from few to hundreds of micrometers. This kind of injection highly disturbs and cools plasma jet because of presence of liquid droplets and stream of atomizing gas. The stream of atomized suspension has usually a cone shape with narrow cone angle what causes that the droplets achieve different areas of plasma jet. The most desirable is the situation when all droplets would be injected into plasma core. In practice, the droplets are injected into plasma jet core as well as to jet fringes what is not advisable (not enough energy to evaporate solvent and heat powder particles). Also small sized particles have to small momentum to get into plasma jet core so they stay in plasma fringes in spite of good flight direction towards to plasma core.
- **Mechanical injection**
    - First type of mechanical injection is achieved by using some ink printing nozzles which are electronically controlled with frequency about tens of kHz. Usually, those nozzles are made as cylindrical body and piezoelectric core. Diameter of nozzle determines droplet sizes. Droplet velocity is determined by pressure inside liquid container and by frequency which also determines the number of produced droplets.
    - Second type of mechanical injection occurs when liquid is placed in a closed container where some external pressure is applied, sometimes called Pressurized Vessel System (PVS). This pressure determines velocity of particles stream. The nozzle diameter influences directly the droplet size. This method can operate with atomizing nozzle and continuous stream nozzle.

Two types of injection nozzles are under consideration in this thesis i.e. atomizing injection nozzle and continuous stream nozzle of injected suspension. Atomizing nozzle is only used as an external injector. The second type of injector may be located outside the plasma torch – which is called external injection, or may be mounted inside the torch, where internal injection takes place. This nozzle can be supplied only by pneumatic system, because peristaltic pumps have not enough pressure to inject suspension inside the plasma jet. A view of the injectors mounted on the plasma torch is presented in Figure 2.7.

Figure 2.7 *Internally mounted continuous stream nozzle into the plasma torch (left), externally mounted atomizing nozzle(right).*

Typical atomization nozzles can be made as:

- capillary atomizer
- fan nozzle (mechanical secondary atomization)
- air blast atomizer (type of atomizer nozzle used by author)

In the case of external injection, the droplets of suspension may have different trajectories within plasma jet, depending on injection parameters. Classification of those trajectories for SPPS was presented by Gell et al. [24] and is shown in Figure 2.8. The same phenomena and nomenclature concerns SPS.

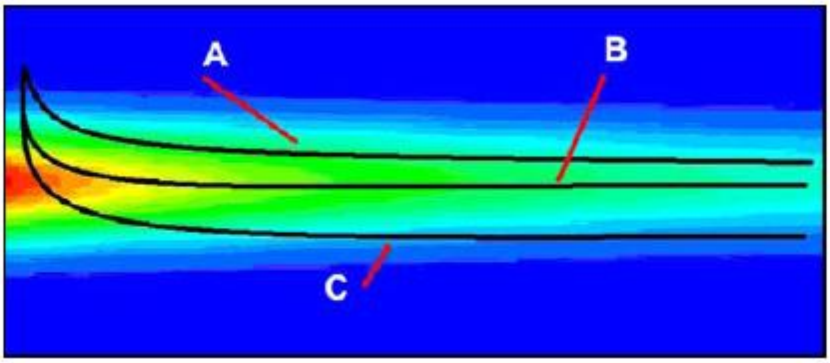

Figure 2.8 *Possible trajectories of suspension droplet/stream injected into plasma jet: A) under penetration, B) ideal penetration and C) over penetration [24].*

2.5 FINELY STRUCTURED COATINGS OBTAINED BY SPS

Microstructure of SPS coatings depends on higher number of parameters than in the case of conventional spraying. For example for APS the most significant parameters are: spraying distance, electric arc power, plasma gases composition and feed rate and carrier gas feed rate. In the case of SPS instead of the last parameter, additionally new emerged: suspension feed rate, suspension composition (among other things: GLR, kind of solvent, kind of dispersant), kind of injection (internal or external, atomizer nozzle or continuous stream nozzle, angle of injection). This makes SPS more complicated and requires more time and more investigations to optimize finely structured coatings.

Due to finely structured powder used for the suspension production, SPS coating should be more dense and compact in comparison to other thermally sprayed coatings [78]. In consideration of density and adhesion, the fact that injection of suspension droplets may have different place within plasma jet, those properties are worse than expected. It is caused by the droplets which are injected into plasma fringes and are not properly heated and melted (low temperature space) and in consequence they are deposited on the substrate as just dried powder particles and are sintered by the next torch pass. These phenomena influence also negatively coating cohesion also. Next difference in relation to APS coatings is the fact that smaller particles of powder result in splats with smaller diameter and thickness. Generally, the coatings obtained by SPS have, after tens of torch passages, thickness of the order of tens micrometers instead of hundreds of micrometers in APS case. However, in some cases thinner coatings are advisable - Rampon et al. investigated SOFCs where decreasing to thin (10 to 20 μm) zirconia- based electrolyte coatings should improve cell stability, life time and operating temperature [71].

Ctibor et al. [79] claimed that the nanostructured coatings in general, exhibit finer pores than the coatings obtained by spraying conventional microsized powders.

Typical, porous, finely structured SPS titania coating is compared to alumina coating deposited by APS in Figure 2.9.

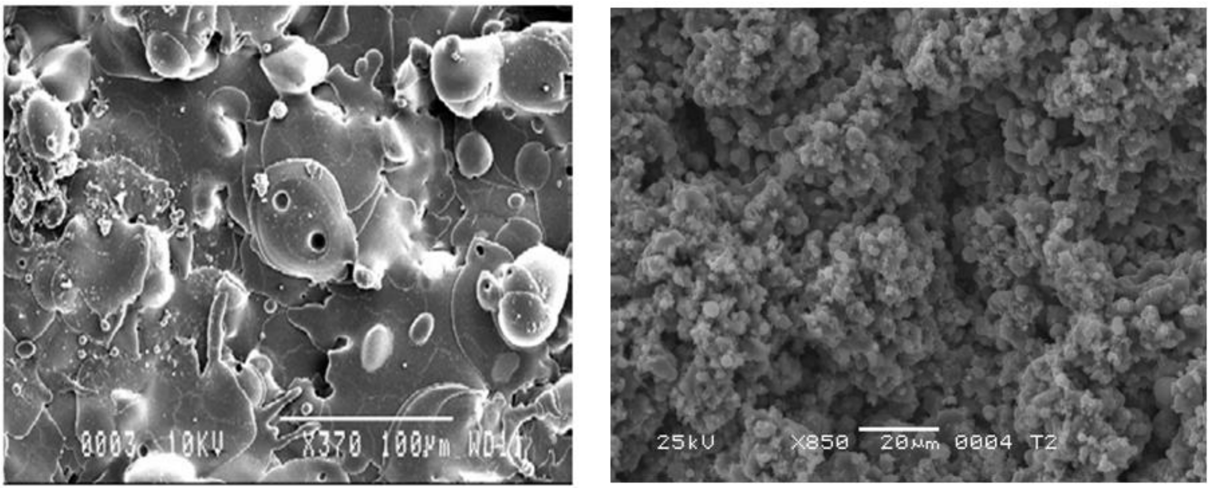

Figure 2.9 *APS alumina coating (left), and porous, finely structured SPS titania coating (right).*

During SPS phase decomposition occurs, similar to that described in section 1.3. Additionally, during spraying the coatings from alcoholic suspension, formation of carbides probably occurs. However, this problem was not widely examined. Defects which are present in finely structured coatings are caused mainly by the same reasons as described in section 1.3. Extra defects connected with weak cohesion are caused by poor evaporation of suspension solvent what results in deposition of just dried powder which may be later sintered or covered by the next layer of the coating.

2.6 METHODS OF EXPERIMENTAL INVESTIGATION

2.6.1 Granulometry

The distribution of powder grains sizes was measured by Mastersizer X Series N^{o}6078 with PS14B Sample Suspension Unit produced by Malvern Company. The analysis of measurement results was carried out by Malvern Instrument MastersizerX v.2.15 software.

2.6.2 Temperature measurements

Temperature of coating at plasma spraying was measured using digital infrared IN5PLUS pyrometer made by Impac. The results were collected and presented graphically using InfraWin software.

2.6.3 X-ray diffraction (XRD)

X- ray diffraction spectra were measured (in ENSCL laboratory) by Bruker D8, Karlsruhe, with CuK_{α} radiation using 2θ usually in the range from 20^{0} to 60^{0}. The patterns were analyzed using Diffrac Eva software based on Joint Committee on Powder Diffraction Standards - International Centre of Diffraction Data – JCPDS-ICDD.

Some measurements concerning phase analysis for the needs of hydroxyapatite powder optimization were done using a set-up of Miniflex of Rigaku (Japan) with CuK_{α} radiation and Rigaku software.

Phase content analysis by Reference Intensity Ratio (RIR) method

Measurement conditions:

Step of 0.02 degree in the 2θ scale are usually used with the time longer than 2 seconds per step. If the counting time is longer, then higher sensitivity is obtained. The counting time over 10 seconds per step is preferred.

The RIR method bases on the Internal Standard Method (ISM) which uses the equation (2.4) to estimate the content of unknown phase by knowing a standard phase [80]. The equation has the following form:

$$\frac{X_\alpha}{X_\beta} k = \left(\frac{I_{(hkl)\alpha}}{I_{(hkl)'\beta}}\right) \qquad (2.4)$$

where α is the phase to be determined, β is the standard phase and k is the calibration constant derived from a plot of $I_{(hkl)\alpha}/I_{(hkl)'\beta}$ vs. X_α/X_β . Direct application of ISM method requires careful preparation of standards to determine the calibration curves.

After a simple transformation the equation takes the following form:

$$X_\alpha = \frac{1}{k} X_\beta \left(\frac{I_{(hkl)\alpha}}{I_{(hkl)'\beta}}\right) \qquad (2.5)$$

Values of k using corundum as the β phase (standard) in a 50:50 mixture with the α phase are now published for different phases in ICDD powder diffraction files. The $I_{(hkl)}$ is defined as the 100% peak for each phase, and denoted as I/I_c ($I/I_{corundum}$). The reference intensity ratio for the 50:50 mixture of phase α and corundum is described by relation:

$$RIR_\alpha = \frac{I_\alpha}{I_c} \qquad (2.6)$$

It provides a quick resource for quantitative evaluation. Finally the results of phase content are simply achieved using the Eva software attached to Bruker D8 diffractometer, by adjusting of peaks intensity in the data base to corresponding peaks of obtained spectrum.

Values of RIR for common phases present in plasma sprayed hydroxyapatite obtained from Eva software are listed below (Table 2.1).

Table 2.1 RIR values for the phases present in plasma sprayed hydroxyapatite**.**

Phase type	Number in JCPDS	RIR value
HA	73-1731	1.1
αTCP	70-0374	0.5
βTCP	70-2065	1.3
TTCP	70-1379	0.8
CaO	82-1690	4.5

Phase content analysis by French Norm No. NF S 94-066 and No. NF S 94-067 method

Measurement conditions:
Scan step must be at least $0{,}02^0$ in the 2θ scale.

The method let one to calculate only relative phase content (percentage) i.e. its amount in the proportion to HA. Results of phase content are directly obtained from the calculation of the corresponding peaks areas and their proportion to the area of hydroxyapatite peak.

Data sheet and peaks denotations which are necessary for the calculation of integrated intensity are shown in Table 2.2.

Table 2.2 Basic data for phase content calculations**.**

Phase type	Number in JCPDS	hkl index	Lattice spacing d
HA	9–342	(210)	3.080 Å
αTCP	9–348	(170)	2.905 Å
βTCP	9–169	(0210)	2.88 Å
TTCP	25–1137	(040)	2.995 Å
CaO	4–0777	(200)	2.405 Å

For amorphous phase we need to measure halo which maximum is for d=2.97 Å, and compare its area with the area of HA peak (210).

2.6.4 Micro-Raman Spectroscopy

Micro-Raman spectroscopy studies were carried out using Dilor-Jobin Yvon-Spex, type Lab Ram spectrometer in LASIR, UMR CNRS 8516, University of Lille laboratory,

He-Ne laser with wavelength of 632.8nm and power of 8mW was used. The samples were mounted and positioned in Olympus BX40 microscope table. Two types of observations were carried out i.e. surface observations and cross-section observations. The cross-sections were prepared by immersing the sample in epoxy resin, then cutting the embedded sample transversely and polishing with a sand paper (finally with the least granulation of 4000) and in the end by diamond paste with granulation at least 0.25 μm. The spectra were analyzed using LABSPEC software.

2.6.5 Infrared Spectroscopy (IR)

The infrared spectroscopy is the method of investigation which allows one to obtain vibrational spectra or in the case when far infrared is used - rotational spectra. The IR made possible to determine which of the functional groups are present in the analyzed compound. The measurements in the infrared range let one to analyze the structure of the particles and their influence on surroundings. This is the basic method used in the hydrogen bond investigation and it is complementary to Raman spectroscopy. All measurements were done using Magna IR 860 ESP device in the range of 1400 and 650 [cm^{-1}](resolution 4 [cm^{-1}]) in the reflection-absorption mode (in LASIR, UMR CNRS 8516, University of Lille laboratory).

2.6.6 Scanning Electron Microscopy (SEM)

Two microscopes were used to observe surfaces and cross-sections of the samples. The first one was JEOL-JSM 6480L, equipped with a secondary electron detector and an energy dispersive spectrometer (EDS) (laboratory of Mechanics, University Lille 1, URM CNRS 8107). For a quantitative chemical analysis Cameca CAMEBAX electron micro- probe analyzer (EMPA) was used. Some pictures of cross-sections (prepared as described in section

2.6.4) of HA samples used in corrosion tests were obtained using Back Scattered Electrons (BSE). For the elemental analysis, the second microscope - Cameca SX100 EMPA with four wavelength dispersive X-ray spectrometers (WDS), were used (in ENSCL laboratory).

Additionally cross-sections of HA samples or surfaces of HA samples destined for surface observation were covered by very thin carbon or gold coating to carry away the charges.

2.6.7 Transmission Electron Microscope (TEM)

The TEM studies were realized by a Hitachi H8100 microscope equipped with a scanning unit and detector for secondary electrons at 200 kV (in Institute of Composite Materials, Chemnitz University of Technology). The specimens were prepared as the samples cross-sections (Figure 2.10 a,b).

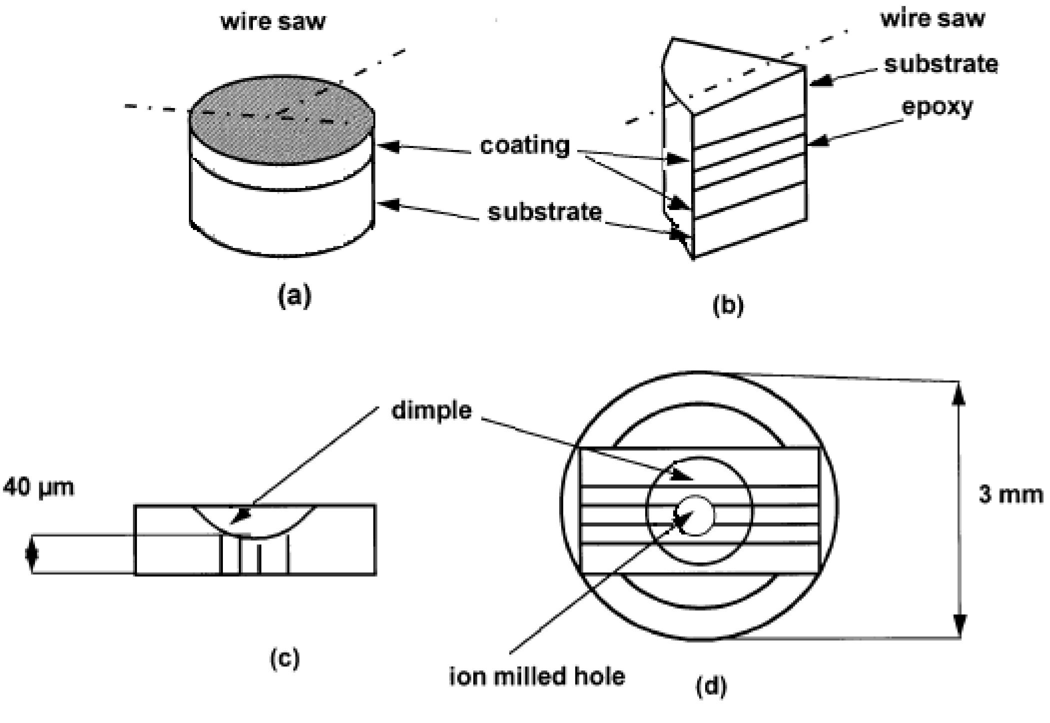

__Figure 2.10__ Schematic description of the TEM specimens preparation [81].

At first the samples were segmented. To avoid a break up of the specimens during sawing and thinning the surface of the specimens was coated with a thin gold layer by means of sputtering. Two segments were then glued with epoxy resin in a face-to-face configuration. Subsequently, thin plates were carefully cut using a diamond wire saw(Figure 2.10 b). The thickness of the plates was reduced, by using SiC sand paper with final granulation of 4000, to a thickness of 50 µm and in the second step by means of one sided dimple grinding in the central part (Figure 2.10 c). After positioning into a copper ring of 3 mm diameter, the centre of the compound was finally thinned by Ar ion milling(Figure 2.10 d). To minimize any artefacts, the energy of the Ar ions and the incident angle were set to 3.5 kV and 5° correspondingly**.**

2.6.8 Impedance Spectroscopy (IS)

Impedance spectroscopy is the method of electrical response analysis of examined material, stimulated by an electrical signal in the wide frequency range in order to investigate physicochemical properties of a material. Results of IS measurements include real and imagine values of impedance vs. time or frequency (few decades mainly from 10μHz to few hundreds of MHz). The results may contain also information about the sample geometry and about the influence of the electrodes and leads on the impedance characteristics. The analysis of the results, depends on construction of the equivalent circuit in which the elements (resistor, capacitor, inductor, or constant phase element (CPE)) and kind of their connections (in series, in parallel or mix of those) inform about the phenomena occurring inside the structure of tested sample and in consequence about the mechanisms of electrical conductivity and polarization [82,83,84,85,86].

In this thesis Agilent 4294A impedance analyzer (in Wroclaw University of Technology, Faculty of Microsystem Electronics and Fotonics laboratory) was used and the results of measurements were analyzed with ZView software. The samples were placed on a heated table with proportional-integral-derivative (PID) temperature controller.

2.6.9 Scratch test

The scratch test was realized with a Micro-CombiTester of CSM Instruments equipped with a Rockwell diamond indenter having a tip radius of 0.2 mm (in Belgian Ceramic Research Center laboratory in Mons, Belgium).

The scratches were linear with progressively increasing load. The critical load L_C was determined as a critical force necessary to peel off the coating which consequently enables one to estimate the coating cohesion by measurements of the scratch hardness. The hardness was calculated using the width of the scratch and the value of force applied.

2.6.10 Design of Experiments (DOE)

Design of Experiments (DOE) is used by many authors to obtain the highest number of valuable information about interesting process parameters using the smallest number of experiments. The goal of the parameters optimization of some production processess is finding such adjustments which allow one to obtain e.g. maximal quantity or the best quality product. In this thesis DOE was used to create a mathematical model which shows the influence of process variables on experiment response. For example the mathematical model describes how the changes of plasma spraying parameters influence the coating properties. The initial step in the design of experiments is a choice of variables which will be coded as low (-1), central (0) and high (+1) level. The experimental space is defined between low and high levels of these parameters real values. The variables in the reported investigations are spraying process parameters and some chemical parameters of the powder synthesis. In the thesis two methods of design of experiments were used i.e. full factorial design and composite matrix [87,88,89].

Full factorial design of experiments

The full factorial design is used when the interactions between the factors which are taken into consideration are suspected. In this type of design the polynomial equation (regression equation) of the following form is utilized:

$$Y = b_0 + \sum b_j X_j + \sum b_{ij} X_{ij} + \sum b_{ijk} X_{ijk} \qquad \mathit{(2.7)}$$

where Y is the system response, b_0 is the mean value of all responses of the experiment, i,j,k vary from 1 to number of variables, b_i coefficient represents the effect of the variable X_i and b_{ij}, b_{ijk} are the coefficients of regression which represent the effects of interactions of variables X_i*X_j and $X_i*X_j*X_k$ respectively.

The polynomial equation for the case of two variables has the following form:

$$Y= b_0 + b_1X_1 + b_2X_2 + b_{12}X_1*X_2 \qquad \mathit{(2.8)}$$

All coefficients representing the effects of the variables were calculated using Nemrod software [90]. The significance level of the effects was specified using Student test, where the estimation of standard deviation σ_i - for coefficient b_i is done and then the ratio b_i/σ_i is calculated. The Student t-test compares resulting value of this ratio to the tabulated value in Student test at 95% confidence level. If the calculated value is greater than the theoretically expected value then the coefficient is significant. The number of freedom degree should be higher than 5. Last step in the analysis is probability calculations and if the value exceeds 50% the variable is significant and hardly influences the process.

Composite matrix

This method is similar to that described above. The difference consist in a change of polynomial which is used for regression and that the analysis of variable coefficient is not so important. The polynomial equation for the case of two variables has the following form:

$$Y= b_0 + b_1X_1 + b_2X_2 + b_{11}X_1^2 + b_{22}X_2^2 + b_{12}X_1X_2 \qquad \mathit{(2.9)}$$

where Y is the system response, b_0 is the mean value of all responses of the experiment, b_1 coefficient represents the effect of the variable X_1 and the same for b_2, b_{11} coefficient represents the effect of the square of variable X_1 and respectively b_{22} coefficient represents the effect of the square of variable X_2, b_{12} is the coefficient of regression which represents the effects of interactions of variables X_1*X_2.

The method does not take into consideration the values of coefficients and their significance but in result of the analysis two dimensional isopleths are drawn. The region where the maximum value of response occurs is marked, and on the other hand the area which should be avoided fill up the plane. Those areas are limited to some values of the variables of course.

3 RESULTS

3.1 SYNTHESIS OF HYDROXYAPATITE POWDER

The goal of the experiments whose results are reported in this chapter was to obtain the purest hydroxyapatite powder (with no admixtures of other phases of calcium phosphate) in rather considerable quantity (no less than 500 grams). There are different ways of synthesis of such hydroxyapatite powder. The most popular are synthesis realized by solution reaction of calcium hydroxide and phosphoric acid [91,92] and by reaction between diammonium phosphate and calcium nitrate in presence of ammonia [93].

In the thesis, the second type of synthesis was chosen, because it seemed secure (less danger chemical agents), and the synthesis using similar parameters has been already carried out in ENSCL laboratory sometime before.

Synthesis of pure hydroxyapatite powder (ideal case) describes the formula below:

$$6(NH_4)_2HPO_4 + 10Ca(NO_3)_2 + 8NH_4OH \rightarrow 6H_2O + 20NH_4NO_3 + Ca_{10}(PO_4)_6(OH)_2$$

Two solutions were prepared as components of the reaction. The first one was diamonnium hydrogenposphate - $(NH_4)_2HPO_4$ (molecular weight M = 132,06 g/mol) dissolved in 50 ml of milliQ water, marked in experiment as [P] solution. The second one was a solution of calcium nitrate tetrahydrate - $Ca(NO_3)_24H_2O$ (molecular weight M = 236,15 g/mol), also dissolved in volume of 50ml of milliQ water, marked in experiment as [Ca] solution. The quantities of the calcium and phosphorus atoms participating in the reaction depended on concentration of the solutions. Mole concentrations of $Ca(NO_3)_24H_2O$ and $(NH_4)_2HPO_4$ were of course equal to mole concentrations of Ca and P atoms, adequately. To obtain maximal productivity of the hydroxyapatite, the atomic ratio of Ca/P in the precursors of reaction must be always equal to atomic ratio of Ca/P in the hydroxyapatite, it means 5/3. Different concentrations of the solutions were prepared for the experiment, their values are presented in Table 3.1.

Table 3.1 Molar concentrations and masses of reaction precursors.

Calcium nitrate tetrahydrate concentration [mol/l]	Mass of the calcium nitrate tetrahydrate dissolved in 50 ml milliQ water [g]	Diammonium hydrogenphosphate concentration [mol/l]	Mass of the diammonium hydrogenphosphate dissolved in 50 ml milliQ water [g]
0.5	5.9038	0.3	1.9809
1	11.8075	0.6	3.9618
2	23.615	1.2	7.9236
3	35.4225	1.8	10.5648
4	47.23	2.4	15.8472

The experiment was carried out in the reactor shown in Figure 3.1.

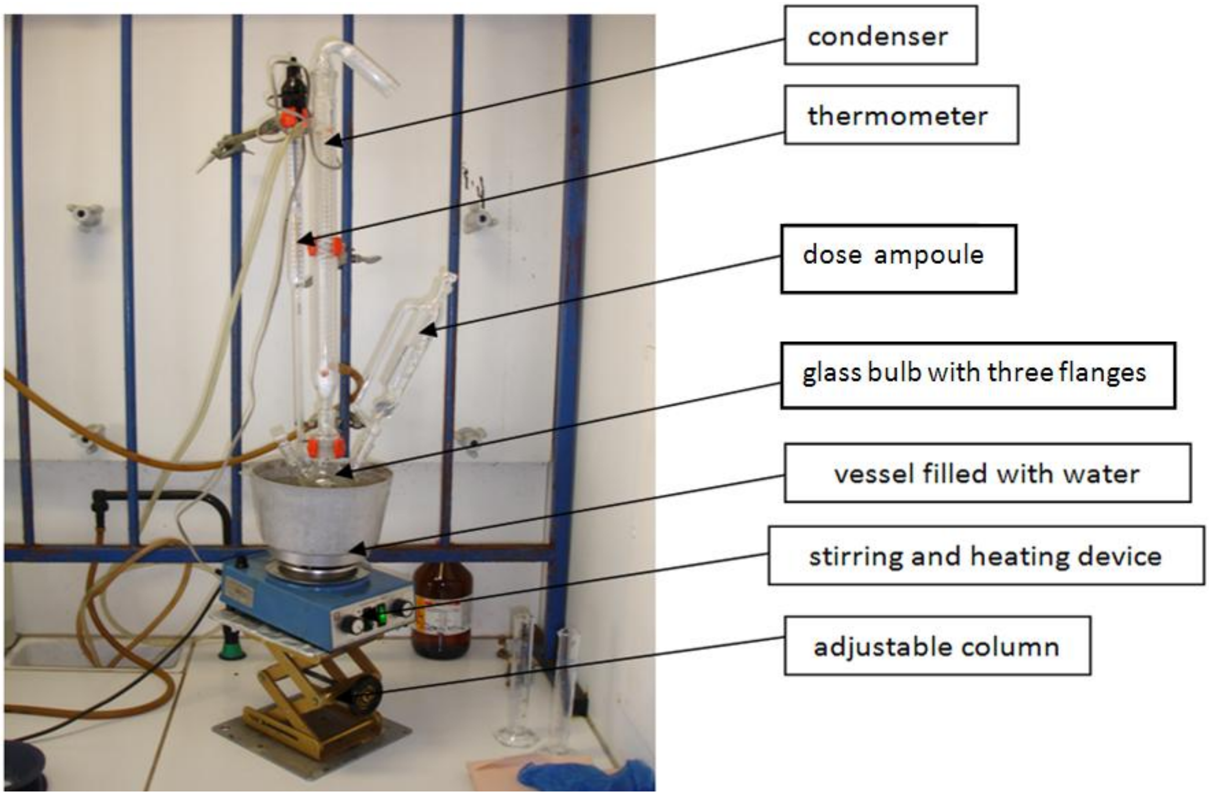

Figure 3.1 *The reactor used for hydroxyapatite powder synthesis.*

The standard procedure for hydroxyapatite synthesis was prepared, including the following steps:

- Introducing of calcium nitrate solution into a glass bulb
- Heating up the solution to 80°C with simultaneous stirring
- Introducing of ammonia solution and initial pH (pH_i) measurement
- Introduction of diammonium phosphate solution dropwise by dose ampoule during 15 minutes
- Keeping on the whole system for 3 hours with continuous heating up to 80°C and stirring
- Measurement of final pH (pH_f) putting the obtained suspension into a closed vessel and leaving it for cooling down for 24 hours
- Filtration of precipitate by vacuum glaze filter and cleaning it by milliQ water
- Drying during a night at elevated temperature of 80° C in an oven
- Calcination of hydroxyapatite powder during a night (2 hours for increasing temperature to 1000° C, 4 hours in constant 1000° C and then convection cooling to ambient temperature).

As the result of chemical reaction a suspension was obtained, with hydroxyapatite powder as precipitate and a mixture of water and ammonium nitrate ($H_2O + NH_4NO_3$) as a solvent. Generally the forming of HA powder is accompanied by forming of other phases i.e. tricalcium phosphate (αTCP and βTCP; $Ca_3(PO_4)_2$), tetracalcium phosphate (TTCP;$Ca_4P_2O_9$), calcium oxide (CaO after calcination from $Ca(OH)_2$). The presence of calcium carbonate ($CaCO_3$) with CO_2 from air was observed.

The calculations of hydroxyapatite content were realized by X-ray spectrum analysis, by the methods described in section 2.6.3. Typical XRD spectrum of HA powder is shown in Figure 3.2.

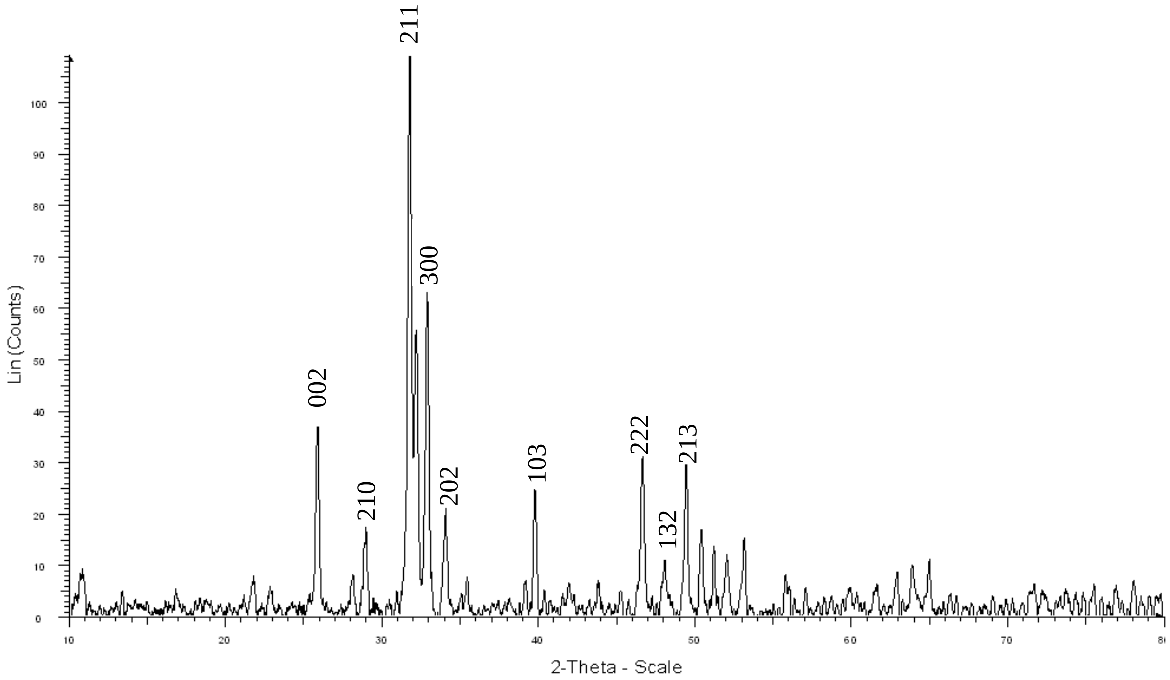

Figure 3.2 *Typical XRD diagram of HA powder with marked peaks.*

Morphology of HA powder particles after synthesis and drying (a) and after calcination (b) with magnification x1000 are presented in Figure 3.3.

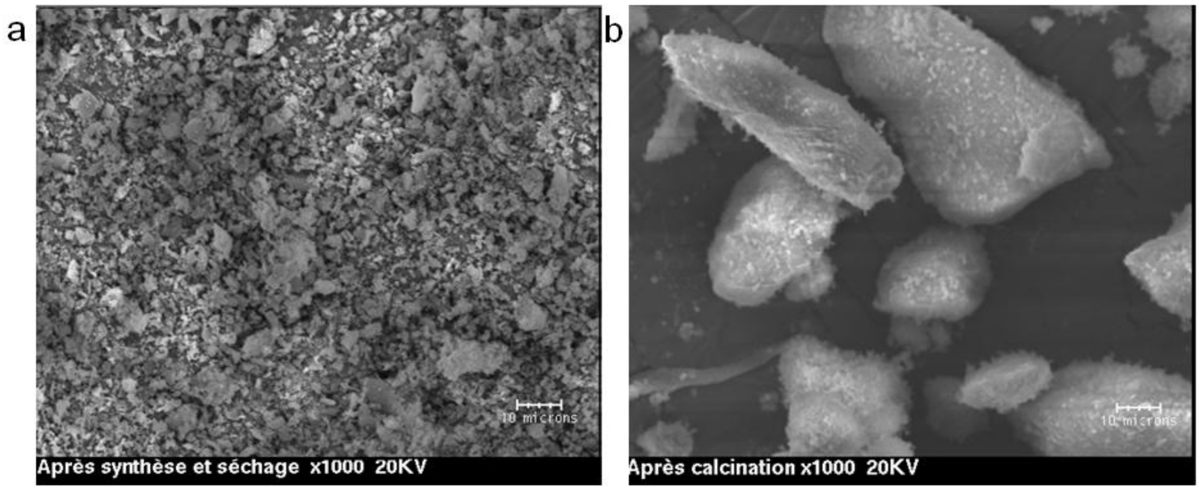

Figure 3.3 *Morphologies of HA powder particles after synthesis and drying (a) and after calcination (b)****[94].***

The micrographs show that the calcination caused significant increase in the powder grains sizes. For the needs of SPS it would be better to use powder without calcination but it was necessary to get crystal form of powder what in consequence required additional treatment i.e. mechanical milling.

3.2 THE OPTIMIZATION OF HYDROXYAPATITE POWDER SYNTHESIS

Two methods of optimization were applied, the first one was an optimization by trial and errors method and the second one was optimization by composite matrix.

3.2.1 Trial and errors method

Optimization of hydroxyapatite synthesis by trial and errors method was carried out, for small amounts of hydroxyapatite, i.e about 2.5 grams for one run of experiment.

For verification of the reactor in ENSCL laboratory and for confirmation of the values of experiment parameters with initial conditions optimized by Hornez et. al [93] the synthesis process was carried out and repeated four times. The results are collected in Table 3.2.

The initial parameters are listed below:

- concentration of calcium nitrate solution : 0.5 mol/l (for 50ml of solution)
- concentration of diammonium phosphate solution: 0.3 mol/l (for 50ml of solution)
- volume of ammonia solution : 10 ml
- time of adding of diammonium phosphate solution : 15 minutes
- time of reaction: 3 hours
- rest time: 24 hours

Table 3.2 Results of initial experiments.

Experiment No.	[Ca] [mol/l]	[P] [mol/l]	V_{amon} [ml]	Time of adding	Time of reaction	Rest time	pH_i	pH_f	Quality of powder	Mass of obtained HA [g]
HA1	0.5	0.3	10	15 min	3h	24h	-	-	100%HA	2.28
HA2	0.5	0.3	10	15 min	3h	24h	-	-	100%HA	2.46
HA3	0.5	0.3	10	15 min	3h	24h	-	-	100%HA	2.45
HA4	0.5	0.3	10	15 min	3h	24h	-	-	100%HA	2.37

The first idea to obtain larger quantities of hydroxyapatite powder in a single synthesis and a shorter time was an increase of the initial solutions concentrations and the values were multiplied by 2,4 and 8 times. The amount of ammonia was the same for all trials. The results of the syntheses are presented in Table 3.3.

Table 3.3 Results of syntheses for different concentrations of initial solutions.

Experiment No.	[Ca] [mol/l]	[P] [mol/l]	V_{amon} [ml]	Time of adding	Time of reaction	Rest time	pH_i	pH_f	Quality of powder	Mass of obtained HA [g]
HA2C	1	0.6	10	15 min	3h	24h	11.68	9.4	91%HA	4.81
HA4C	2	1.2	10	15 min	3h	24h	11.44	8.75	95%HA	9.6
HA8C	4	2.4	10	15 min	3h	24h	11.03	8.7	62%HA	18.93

As it is shown in table 3.3 the quality of the powder seems to depend on initial and final pH of reacting substances. Increasing of pH should increase the purity of hydroxyapatite powder.

The second idea of accelerating the hydroxyapatite synthesis was reduction of the reaction time from 3h to 15minutes. Also the synthesis without rest time was carried out. This experiment was repeated twice. The results of the experiments are shown in Table 3.4.

Table 3.4 Results of the experiments with reaction time shortening.

Experiment No.	[Ca] [mol/L]	[P] [mol/L]	V_{amon} [ml]	Time of adding	Time of reaction	Rest time	pH_i	pH_f	Quality of the powder	Mass of obtained HA [g]
HAe1	0.5	0.3	10	15 min	15 min	0	11.85	9.72	100%HA	2.43
HAe2	0.5	0.3	10	15 min	15 min	0	11.81	9.65	100%HA	2.33

As it can be seen, this idea was correct – substantial shortening of reaction time did not influence the purity of synthesized powder.

Modification of quantity of ammonia solution for different concentrations of initial solutions was the third idea. The quantity of ammonia was multiplied by the same factor as the concentration of initial solutions, it means, that when the concentration was multiplied by 2 the volume of ammonia was also multiplied by 2 in comparison with initial parameters. The results are presented in Table 3.5. The mass of synthesized powder was measured only in the last three experiments.

Table 3.5 Results of the experiment with different ammonia volumes.

Experiment No.	[Ca] [mol/L]	[P] [mol/L]	V_{amon} [ml]	Time of adding	Time of reaction	Rest time	pHi	pH_f	Quality of powder	Mass of obtained HA [g]
HA4C1a	2	1.2	40	15 min	15 min	0	12.03	9.89	100%HA	-
HA4C1b	2	1.2	40	15 min	15 min	24h	12.03	9.89	100%HA	-
HA4C2a	2	1.2	80	15 min	15 min	0	12.37	9.76	99%HA	-
HA4C2b	2	1.2	80	15 min	3h	24h	12.37	9.52	99%HA	-
HA8C1a	4	2.4	80	15 min	15 min	0	12.24	10.04	98%HA	-
HA8C1b	4	2.4	80	15 min	3h	24h	12.24	9.11	98%HA	-
HA8C2	4	2.4	80	15 min	3h	24h	12	9.56	98%HA	-
HA8CA1	4	2.4	40	15 min	15 min	0	11.42	8.86	92%HA	18.77
HA8CA2	4	2.4	60	15 min	15 min	0	11.65	9.14	83%HA	18.2
HA8CA3	4	2.4	100	15 min	15 min	0	11.91	9.58	37%HA	12.4

According to Table 3.5 the most interesting for further synthesis was the experiment marked in red with No. HA4C1a. The experiment was chosen for synthesis because the time of reaction was considerably reduced, the concentrations of initial solutions were multiplied, what should result in shortening the time needed for synthesis of 500 grams of HA powder.

The next step was to check the influence of changing volume of reagents and volume of reactor, what is sometimes called as a scale effect. In this case a glass bulb with the volume of 1l was used instead of the 0.25l, and the volumes of added precursor solutions were changed from 50ml to 200ml. The last change increased the masses of calcium nitrate and diammonium phosphate dissolved in milliQ water to 94.46 grams and 31.6944 correspondingly. In result the powder with 100% quality was obtained. Finally, the parameters of the experiment HA4C1a were applied for synthesis of large quantity (about 600-700g) of HA powder.

3.2.2 Analysis by composite matrix

Design of experiment DOE using composite matrix has been roughly described in section 2.6.10.

The analysis includes two-factorial statistical investigation, using the concentration of calcium nitrate solution as the first factor (the concentration of diammonium phosphate is inherently connected with the concentration of calcium nitrate by chemical reaction) and the volume of ammonium solution as the second one. As the responses purity (or quality) and mass of obtained powder are taken.

The composite matrix consists of three blocks:

- complete full factorial 2^k matrix, (No. 1 to No. 4 experiments)
- matrix with four star points i.e. α=1.41, (No. 5 to No. 8 experiments)
- matrix of the central experiment with 0 level (No. 9 to No. 11 experiments)

In the Table 3.6 experimental space (composite matrix) with code values (levels) of the experiment parameters ([Ca], [P] and V_{amon}) and corresponding real values, are presented.

Table 3.6 Experimental space presented as composite matrix .

N°exp	Normalized units			Natural units		
	[Ca] [mol/l]	[P] [mol/l]	V_{amon} [ml]	[Ca] [mol/l]	[P] [mol/l]	V_{amon} [ml]
1	-1	-1	-1	1	0.6	20
2	1	1	-1	3	1.8	20
3	-1	-1	1	1	0.6	60
4	1	1	1	3	1.8	60
5	-1,41	-1,41	0	0.57	0.35	40
6	1,41	1,41	0	3.4	2.0	40
7	0	0	-1,41	2	1.2	11.7
8	0	0	1,41	2	1.2	68.3
9	0	0	0	2	1.2	40
10	0	0	0	2	1.2	40
11	0	0	0	2	1.2	40

The results of purity estimation of HA powder and masses of obtained dried powder are presented in Table 3.7 as experimental responses Y_1 and Y_2 for variables X_1 (concentration of $[Ca^{2+}]$) and X_2 (volume of ammonium hydroxide) respectively.

Table 3.7 Experimental composite matrix with variables and their responses.

N°exp	X_1 $[Ca^{2+}]$ [mol/l]	X_2 vol. NH_4OH [ml]	Y_1 =Purity of obtained powder [%]	Y_2 = Mass of obtained powder [g]
1	1	20	100	4.96
2	3	20	46	13.48
3	1	60	98	4.95
4	3	60	65	14.38
5	0.57	40	100	2.76
6	3.4	40	60	16.17
7	2	11.7	85	9.9
8	2	68.3	98	9.98
9	2	40	99	9.85
10	2	40	100	9.81
11	2	40	100	9.75

As it was mentioned before, the composite matrix is composed of three blocs i.e. full factorial design (exp. No. 1-4), 4 star points (exp. No. 5-8) and 3 experiments in the center (exp. No. 9-11) are compiled in graphical form in Figure3.4.

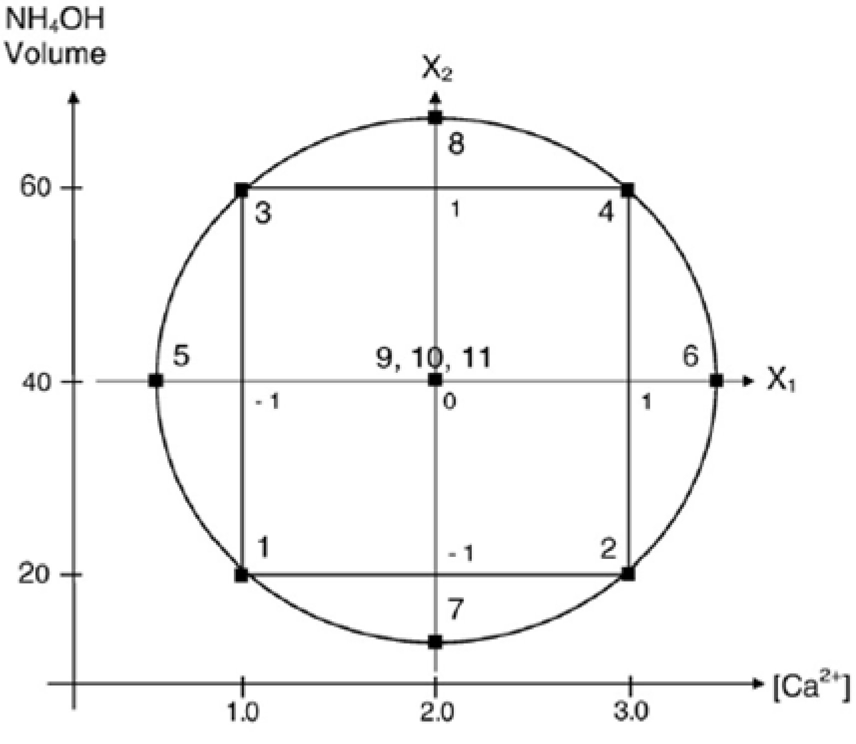

Figure 3.4 *Composite design for two process variables: $[Ca^{2+}]$ mole concentration [mol/l] and volume of ammonium hydroxide NH_4OH [ml]* ***[95].***

The next step concerns to the calculations of isopleths for two process variables i.e. concentration of calcium nitrate solution and volume of ammonium hydroxide. The results (response Y_1) are shown graphically in the X_1 X_2 plane (in normalized units) in Figure 3.5.

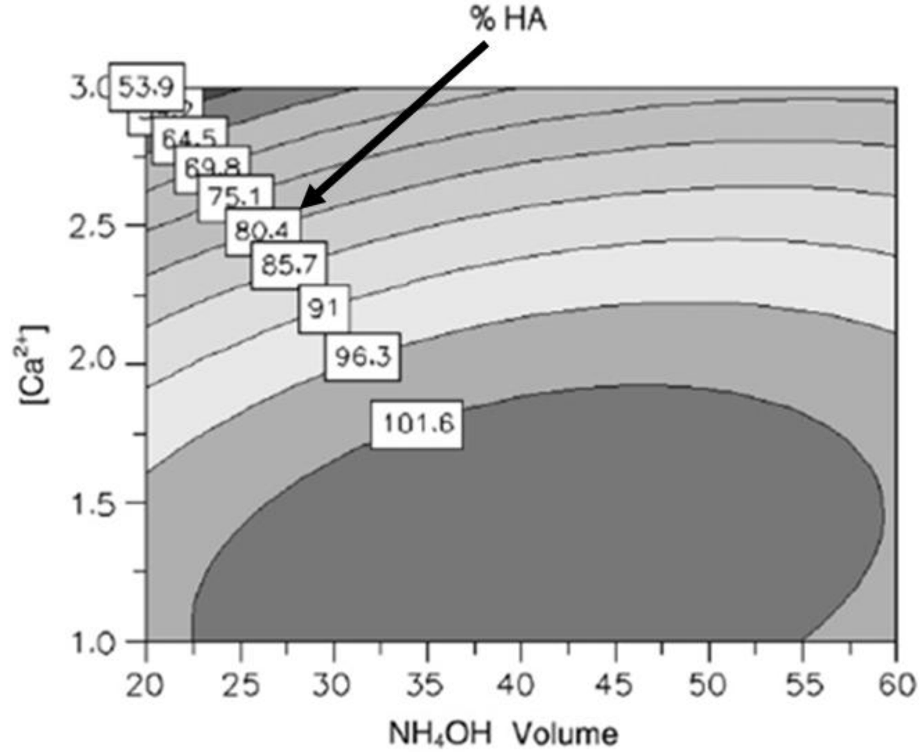

Figure 3.5 *Experimental values of purity of HA and the corresponding isopleths for two process variables: [Ca^{2+}] mole concentration [mol/l] and volume of ammonium hydroxide NH_4OH [ml]* ***[95].***

The response Y_2 clearly indicates that the mass of dried powder is strongly correlated with the concentration of calcium nitrate (Table 3.7).

The value of 101.6% is of course the result of software calculations. The area limited to this curve indicates the most purest hydroxyapatite powder which we can obtained. As it is shown in Figure 3.5, the response Y_1 (purity of HA) is also correlated with calcium nitrate concentration and for the concentration values above than 2 [mol/l] obtaining of pure HA is impossible.

After statistical treatment by Nemrod software, the coefficients which represent the variable effects and their interactions are substituted to the regression equation corresponding to composite matrix (values rounded off) and the equation takes the following form:

$$Y= 100 - 18 X_1 + 4 X_2 - 12 X_1^2 - 6 X_2^2 + 5 X_1 X_2 \qquad (3.1)$$

Basing on the equation above by deriving and assuming that the derivative is equal to zero, the optimal values of the variables were found:

- X_{1opt} equal to - 0.74 (optimal concentration of calcium nitrate solution should be equal to 1.26 mol/l and correspondingly, the concentration of diammonium phosphate solution 0.76 mol/l)
- X_{2opt} equal to 0.041 (optimal volume of ammonia should be equal to 41ml)

The calculated values confirm that optimal experimental conditions are within the experimental area shown in Figure 3.5. After HA synthesis optimization about 600g of powder (the mean purity 99%) was obtained.

Finally the grains size distribution of HA powder obtained by the procedure described in this section are shown in Figure 3.6.

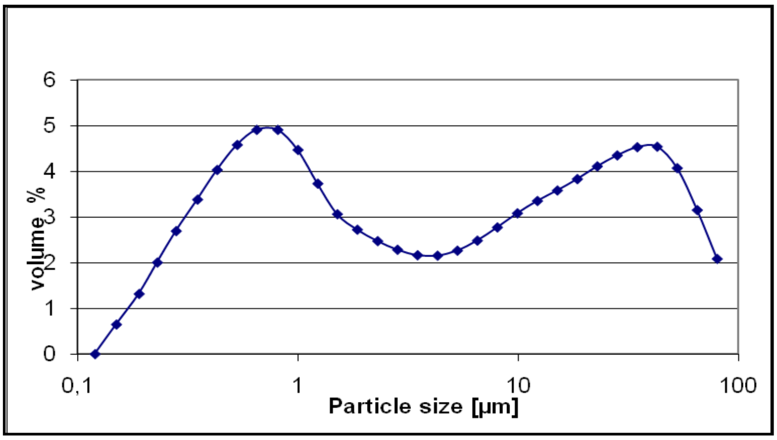

***Figure 3.6** Grains size distribution of home made hydroxyapatite powder.*

The distribution of the HA powder particles is bimodal. There is high number of the particles with the sizes below 1µm, but the second maximum is visible for the sizes about 70µm. It is probably caused by additional treatment of powder after calcination i.e attrition milling where powder was mechanically comminuted by zirconia balls in form of suspension with ethanol as a cooling medium. Then the powder was dried (that process favors forming of agglomerates) and finally powder was separated from zirconia balls by sieving using 150µm grit size sieve.

The synthesis of the hydroxyapatite powder by precipitation was carried out. The precursor solutions were diammonium phosphate and calcium nitrate. The optimization of the synthesis was done by two ways i.e. trial and errors method and composite matrix as well. The mass and the purity of the obtained powder were taken as response for the two variables – concentration of the [Ca] solution and volume of ammonia which participated in chemical reaction. The optimal values of the variables were calculated and for the concentration of [Ca] solution it was 1.26 mol/l and optimal volume of ammonia was equal to 41ml. Also the temperature raised to 80^0C in comparison to 60^0C applied by Bouyer et al. [106] to the synthesis seems to result in better purity of the powder. The change in the synthesis parameters results in forming of different phases of calcium phosphate. Unfortunately the calcination and attrition milling must have been applied to obtain fine grained powder in crystalline form.

3.3 OPTIMIZATION OF SUSPENSION INJECTION SYSTEM

Optimization of injection was carried out using two types of injectors i.e. atomizer nozzle (air blast nozzle, ATM), and continuous stream nozzle (CSN). The latter was made with different internal diameters (this parameter was strongly correlated with droplet sizes). The configuration of injectors mounted onto the torch is shown in Figure 2.7. The CSN is shown in Figure 3.7.

Figure 3.7 *View of continuous stream nozzles.*

The optimization was carried out by changing some parameters of injection, injector configuration and electric power input into plasma. All experiments were carried out with the use of PVS (shown in Figure 2.6 a).

The parameters which were the same for all runs are listed below:

- ✓ Ar feed rate – 45 slpm
- ✓ H_2 feed rate – 5 slpm
- ✓ No. of passages – 4 (excluding run No. 23 where 36 passages were done)
- ✓ Contents of powder in each suspension was 20 wt% (different solvents were used - water, ethanol or a mixture of ethanol with water 50:50 wt%)

The rest of parameters which were adjusted are listed below (Table 3.8). The surfaces of majority of samples were smooth but in some experiments rough surfaces were obtained by sand blasting.

Table 3.8 The parameters used in experiments (where ATM – atomizer nozzle, CSN – continuous stream nozzle (in configuration as internal – int and external - ext)).

Experiment No.	Injector type /configuration/ /internal diameter[mm]	Pressure of atomizing gas or gas which push out the suspension [bar]	Suspension solvent	Spray distance [mm]	Electric power input to plasma[kW]
7	CSN/int/0.6	0.4	H_2O	50	30
8	CSN/int/0.6	0.2-0.3	H_2O	50	40
9	CSN/int/0.5	0.2-0.3	C_2H_5OH	80	40
10	CSN/int/0.5	0.2-0.3	C_2H_5OH	50	40
13	ATM/ext/08	0.8	H_2O	80	30
14	CSN/ext/0.5	0.8	H_2O	80	30
15	CSN/int/0.5	0.2	H_2O	80	30
16	ATM/ext/08	0.8	C_2H_5OH	80	30
17	CSN/ext/0.5	0.8	C_2H_5OH	80	30
18	CSN/int/0.5	0.2	C_2H_5OH	80	30
19	CSN/int/0.5	0.4	H_2O/ C_2H_5OH	80	30
20	CSN/int/0.5	0.4	H_2O/ C_2H_5OH	60	30
21	ATM/ext/08	0.8	H_2O/ C_2H_5OH	60	30
22	ATM/ext/08	0.8	H_2O/ C_2H_5OH	80	30
23	CSN/int/0.5	0.5	H_2O/ C_2H_5OH	60	30

SEM images of sample surfaces bring some information about the quality of the coatings. Two samples were chosen as examples to illustrate some effects of injection on the coating properties. The samples are presented in Figure 3.8. Micrographs of the other samples are shown in appendix (section 7.1).

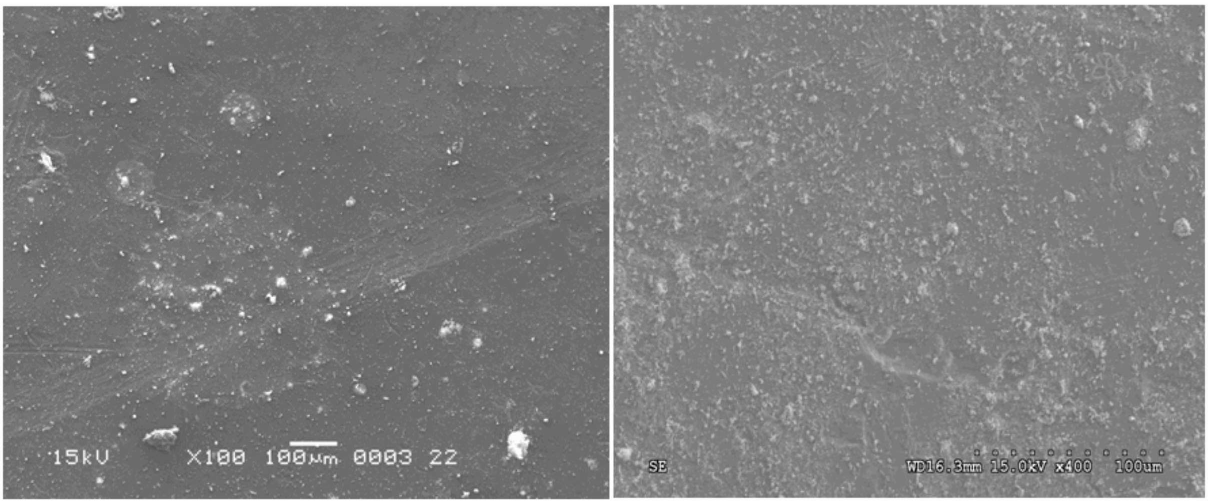

Figure 3.8 *Micrograph of sample No. 22 (left - magnification x100) and No. 8 (right – magnification x400).*

The examples presented in Figure 3.8 show a significant difference between the sample sprayed using atomizer (left) and CSN (right). High number of fine splats was obtained in the case of internal injector. The traces (residua) of evaporated droplets occurring in the experiment No. 22 (probably the droplets were injected into plasma jet fringes) mean that in these cases the solvent was evaporated after the droplet impact on the substrate. Then the powder particles were sintered – in consequences adhesion of the coating was decreased. Additionally the feed rate of suspension in the case CSN was significantly lower (due to reduced pushing gas pressure) and as result more splats were obtained, this indicates that using CSN/int increases the spraying efficiency significantly.

Some investigations concerning suspension temperature raise before injecting should be undertaken. Preheating of the suspension could have a positive influence on more effective and faster solvent evaporation.

The results of the injection optimizations let one to see that the most important parameter of the suspension injection is the suspension feed rate. The maximum of the suspension feed rate may be different for different electric power inputs to plasma due to the change of the temperature of the plasma jet. The atomizer cools down plasma more than CSN. This may be compensated by changing the spraying distance, but there are some limitations due to substrate melting point, which may be melted when the spraying distance will be too short.

The atomizer favors the suspension particles to stay in the jet periphery what is unwanted in the SPS process. Finally the CSN/int is the most promising and the most efficient injection system.

As the solvent the mixture of ethanol with water in 50:50 proportion is chosen as the optimal. Water cooled down the plasma jet more intensively in comparison with pure ethanol which caused excessive raise of the temperature and melting of the substrate (under condition that, the rest of parameters was the same).

3.4 PROPERTIES OF HYDROXYAPATITE COATINGS

3.4.1 Preliminary investigations of HA coatings

The samples were prepared by SPS using home synthesized HA powder described in section 3.1.

The substrates used in this experiment were titanium plates with dimensions 20x20x0.8 mm. Before spraying, the plates were sand blasted using corundum grit (size -250+120µm), under pressure of 2 bar, then the substrates were cleaned by ethanol and dried by compressed air.

The next step enclosed preparation of suspension with the following proportions:
360g of distilled water, 360g of ethanol and 80g of HA powder what corresponds to 40 wt% of water, 40 wt% of ethanol and 20 wt% of HA.

Previously prepared suspension was injected by a nozzle into plasma jet inside plasma torch Praxair SG-100 (with attached anode 03083-175, cathode 03083-129 and gas injector 03083-113), mounted on 5-axis ABB IRB-6 industrial robot. The view of spraying installation illustrates Figure 3.9. Additionally, reservoir with water was used to clean suspension delivery system between experiments to prevent blocking of the injector .

Figure 3.9 *Plasma spraying installation.*

As plasma gas a mixture of Ar and H_2 with flow rate of 45 and 5 slpm correspondingly was used. Electric power input into plasma was equal to 40kW. Suspension injection parameters were adjusted as follows - angle of injection $\alpha=100^0$, distance d = 8mm, distance D =10mm accordingly to Figure 3.10. The suspension injector was in configuration of continuous stream nozzle with internal diameter of 0.75mm. Trajectory of the torch over the samples is presented in Figure 3.10. Twenty passes for each run were done with a break of 1 minute for cooling between every five passages. Variable parameters of spraying, maximal coating temperature during spraying and estimated coating thicknesses are presented in Table 3.9.

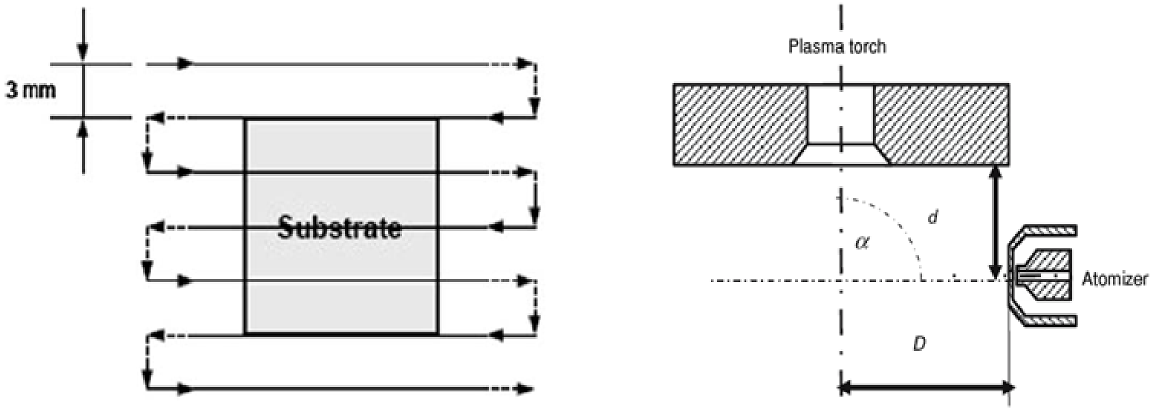

Figure 3.10** Trajectory of the torch over the substrate (left), and sketch of suspension injector position (right). Internal diameter of atomized liquid outlet is 1.5mm and internal diameter of suspension delivery outlet is 0.7mm **[96].

Table 3.9 Variable spray parameters, maximal coating temperature and coating thicknesses **[94].**

Experiment No.	Torch linear velocity [mm/s]	Spray distance [mm]	Maximal coating temperature during spraying [°C]	Coating thickness [µm]
1	125	50	860	10
2	125	60	450	13
3	250	50	560	Very thin
4	250	60	290	33

The results of the maximal coating temperature measurements indicate that the spraying distance influences the coating temperature significantly, the values for 50 mm are higher than values for 60 mm, independently on the torch velocity. In the case of the coating thickness measurements the results suggest the torch velocity equal to 125 mm/s in the aspect of repeatable coating thickness.

The contents of crystal phases present in obtained coatings were determined according to French Norm phase content calculation method. Results of the calculations are collected in Table 3.10.

Table 3.10 Crystal phase content in SPS coatings **[94].**

Experiment No.	α-TCP/HA [%]	β-TCP/HA [%]	TTCP/HA [%]	CaO/HA [%]	Amorphous/HA [%]
1	31	21	12	Absent	Absent
2	37	2	Absent	Absent	3
3	21	10	10	6	Absent
4	Absent	33	Absent	5	Absent

The coatings sprayed in this experiment were very thin and their color turned to be dark brown. This fact caused that optimization of suspension injection system was necessary (see section 3.3) and no further investigations for this experiment were done. The phase content analysis of sprayed coatings shows that α-TCP is the most evident, the other phases are less evident, with finally nearly absent amorphous phosphate phase. There is no regular relationship between phase content and spraying parameters (torch velocity and spraying distance).

3.4.2 Corrosion investigation – HA samples in BSF

After optimization of injection system successive experiments were prepared using design of experiments DOE to investigate corrosion of HA coatings in Body Simulated Fluid (BSF). Experimental space (Table 3.11) was chosen for 2 parameters i.e. spraying distance and electric power input to plasma. The rest of parameters was kept constant similar to previous experiments, differences consisted in the fact that linear velocity of plasma torch was set as constant and equal to 500mm/s and internal injector (with internal diameter of 0.5mm) was used instead of external injector. The samples and suspension were prepared by the same method as described in previous experiment. For this experiment 70 samples were sprayed in total. Fourteen samples per one experimental conditions set were sprayed in two runs i.e. 7 samples by run.

Table 3.11 Experimental space chosen for corrosion investigations.

Experiment No.	Electric power input in plasma [kW]	Spraying distance [mm]	Resulting maximal coating temperature during spraying [°C]
1	30	60	510
2	27	50	600
3	33	50	630
4	27	70	520
5	33	70	630

Selection of BSF was carried out by comparison of ion molar concentrations in two simulated body fluids i.e. Kokubo solution and Hank solution with their concentrations in human plasma. This comparison is shown in Table 3.12.

Table 3.12 Comparison of BSF fluids to human plasma.

Ions type	Molar concentration of ions [mmol/l]		
	Kokubo solution	Hank solution	human plasma
Ca^{2+}	2.5	1.3	2.2
HPO_4^{2-}	1.0	0.8	0.8
Na^{+}	142.0	137.7	140.3
Cl^{-}	148.8	146.9	148.0
Mg^{2+}	1.5	1.9	1.3
K^{+}	5.0	5.4	5.3
SO_4^{2-}	0.5	0.8	0.5
HCO_3^{-}	4.2	-	4.0
pH	7.4	7.0	7.4

Finally the Kokubo solution was chosen for corrosion tests due to its closer ion concentrations to human plasma. Futhermore, the solution also includes less hazardeous reagents and there is an easy way to adjust its pH. Based on the indications, the concentrations about 1l of BSF was prepared. Time of immersion was chosen as a parameter in corrosion tests. The immersion periods were: 0, 3, 7, 14, 28 and 60 days. To prevent samples from influence of dissolved components of coating in BSF each sample was immersed in BSF in a separate small container. All containers were put into a reservoir filled with water heated to 37^{0}C with using of temperature controlling unit. The complete experimental set is shown in Figure 3.11. After immersion period, the samples were cleaned in distilled water and dried by night in temperature 60^{0}C, then the samples were prepared for further investigations (cross-sections etc.).

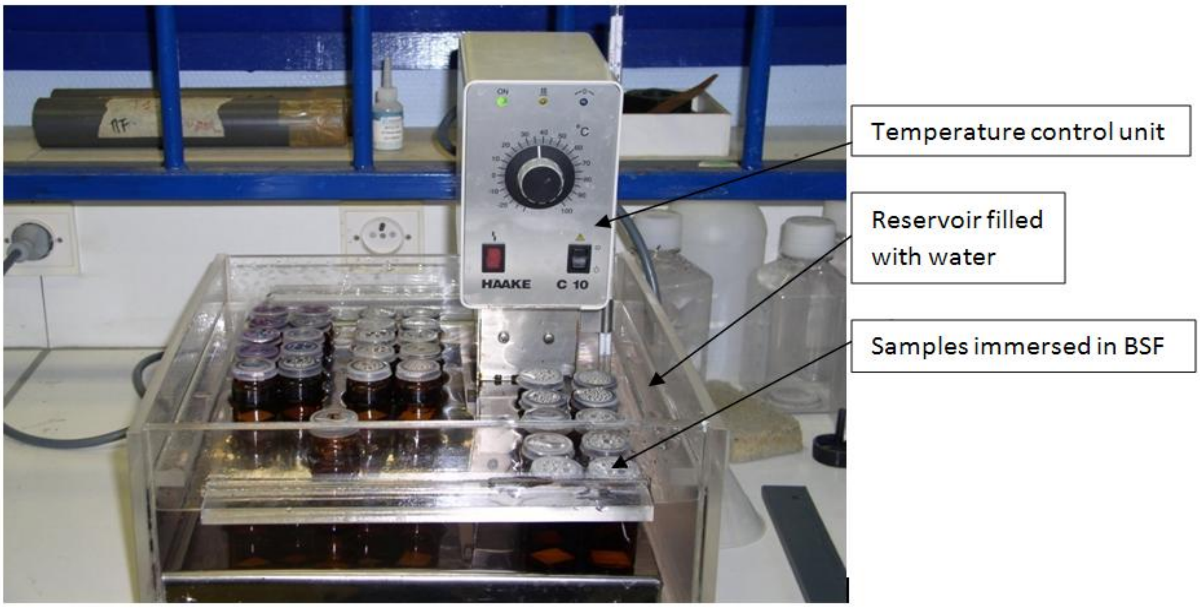

Figure 3.11 *Experimental setup for corrosion investigations.*

Denotations of all investigated samples are collected in Table 3.13.

Table 3.13 Samples codes.

Sample Code	Experiment N°	SBF Soaking Period [days]	Samples Quantity
100	1	0	3
103	1	3	3
107	1	7	2
114	1	14	2
128	1	28	2
160	1	60	2
200	2	0	3
203	2	3	3
207	2	7	2
214	2	14	2
228	2	28	2
260	2	60	2
300	3	0	3
303	3	3	3
307	3	7	2
314	3	14	2
328	3	28	2
360	3	60	2
400	4	0	3
403	4	3	3
407	4	7	2
414	4	14	2
428	4	28	2
460	4	60	2
500	5	0	3
503	5	3	3
507	5	7	2
514	5	14	2
528	5	28	2
560	5	60	2

3.4.3 X-ray phase content investigation

Firstly, the phase content analysis was carried out, using RIR method, for one of each experiment sample. The results are listed in Table 3.14.

Table 3.14 Phase content in samples used for corrosion tests.

Sample Code	Fraction of HA [%]	Fraction of α-TCP [%]	Fraction of β-TCP [%]	Fraction of TTCP [%]	Fraction of CaO [%]
100	85.6	11.1	2.4	0.0	0.8
200	85.2	8.9	1.9	3.6	0.4
300	71.6	14.5	3.7	9.4	0.8
400	85.6	8.7	2.7	1.7	1.2
500	90.9	6.2	1.4	0.1	1.4
103	92.1	6.1	0.7	0.9	0.2
203	90.7	7.9	1.2	0.1	0.1
303	75.9	11.5	1.3	11.0	0.4
403	94.4	4.5	0.9	0.0	0.2
503	89.5	8.5	0.9	0.9	0.2
107	91.7	8.0	0.0	0.0	0.4
207	91.6	5.9	0.0	2.4	0.1
307	74.4	13.6	2.7	9.1	0.3
407	89.2	8.3	2.3	0.0	0.2
507	95.6	3.5	0.0	0.8	0.1
114	89.4	8.7	1.5	0.0	0.4
214	95.8	4.1	0.0	0.0	0.1
314	77.0	11.4	3.5	7.6	0.5
414	92.6	5.2	0.7	1.3	0.2
514	95.2	4.7	0.0	0.0	0.1
128	86.5	9.7	1.2	2.4	0.2
228	95.9	2.3	0.0	1.7	0.2
328	69.2	11.7	3.7	15.1	0.3
428	92.4	5.5	0.7	1.3	0.1
528	91.7	8.2	0.0	0.0	0.2
160	89.2	7.0	1.7	2.0	0.2
260	94.6	4.5	0.3	0.6	0.1
360	74.0	11.0	1.4	13.2	0.4
460	88.4	7.4	1.1	2.6	0.3
560	92.9	6.5	0.0	0.6	0.0

The results of HA fractions calculations are shown in graphical form in Figure 3.12. The contents of remaining phases are shown in appendix (section 7.2).

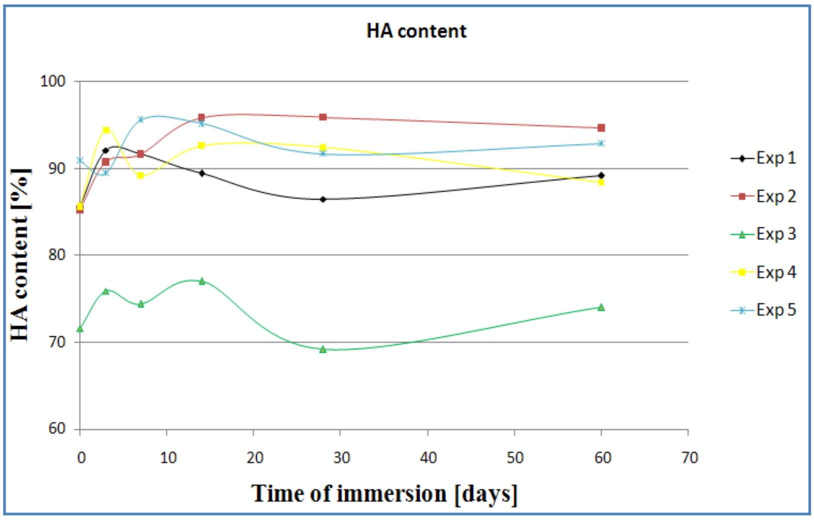

Figure 3.12 *Content of HA vs. immersion time.*

The plots showing the content of HA vs. time of immersion, made possible to decide that the samples of series 2 and 5 were chosen to further investigations, because the content of HA seems to be the most stable independently of immersion time.

The statistical analysis was carried out with Nemrod software to see the influence of spraying parameters on HA content. The results for samples without immersion in BSF are presented in Figure 3.13. The other results are included in appendix (section 7.3). The numbers in squares indicate HA content of the experiment carried out with parameters corresponding to values of variables shown on the axis and corrected by the results of central experiment

Figure 3.13 *Results of statistical treatment showing the influence of spraying parameters on HA content for experiments 1 to 5 without immersion in BSF.*

The mathematical model chosen for this analysis is presented in section 2.6.10 for the case of full factorial design of experiments. The coefficients calculated for all samples b_0, b_1, b_2 and b_{12} are collected in Table 3.15.

Table 3.15 Coefficients representing the effect of the variables in the mathematical models for all experiments.

Time of immersion [days]	b_0	b_1	b_2	b_{12}
0	83.8	-2.1	4.9	4.7
3	88.5	-4.9	4.3	2.5
7	88.5	-2.7	4.7	5.9
14	90	-4	3.8	5.4
28	87.1	-6.8	4.7	6.5
60	87.8	-4	3.2	6.3

Due to small number of experiments the results of calculation didn't show which parameters are the most significant. But it can be clearly seen that for the distance of 70mm the content of HA is higher and does not change drastically with change of electric power input into the plasma. The conditions of the smallest spraying distance and the highest electric power input into plasma (experiment No. 3) caused the most significant phase decomposition what results in the HA content decrease.

3.4.4 Infrared Spectroscopy (IR) analysis

The samples were measured by infrared spectroscopy. The results of measurements are shown in Figure 3.14 and Figure 3.15 for sample series No. 2 and No. 5 respectively. The most significant peak for the calcium phosphate is located in range from 750 cm^{-1} to
1250 cm^{-1}. The results are not good enough due to the difference of the transmittance in the range from

1250 cm^{-1} to 4000 cm^{-1} caused by the changes in the background (probably caused by not sufficient preparation of the coating surface). The results show that the calcium phosphate peak has different transmittance for different samples. In the case of sample series No. 2 these differences are just a little higher than the changes in transmittance disturbed by changes of the background. The case of series No. 5 shows higher changes of the transmittance for the peak of calcium phosphate. Unfortunately, it is impossible to draw any conclusions from the results of infrared spectroscopy measurements presented below.

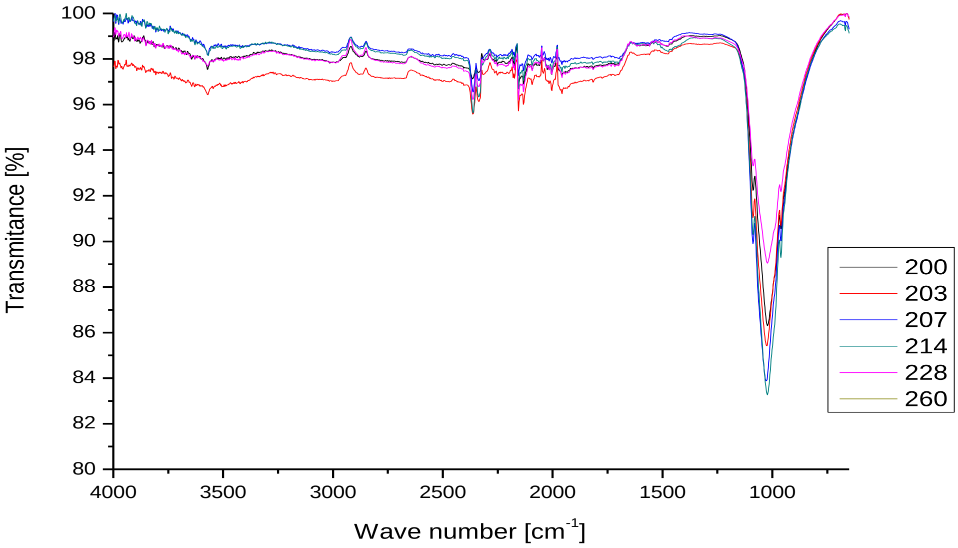

Figure 3.14 *IR spectra for samples series Exp No. 2 .*

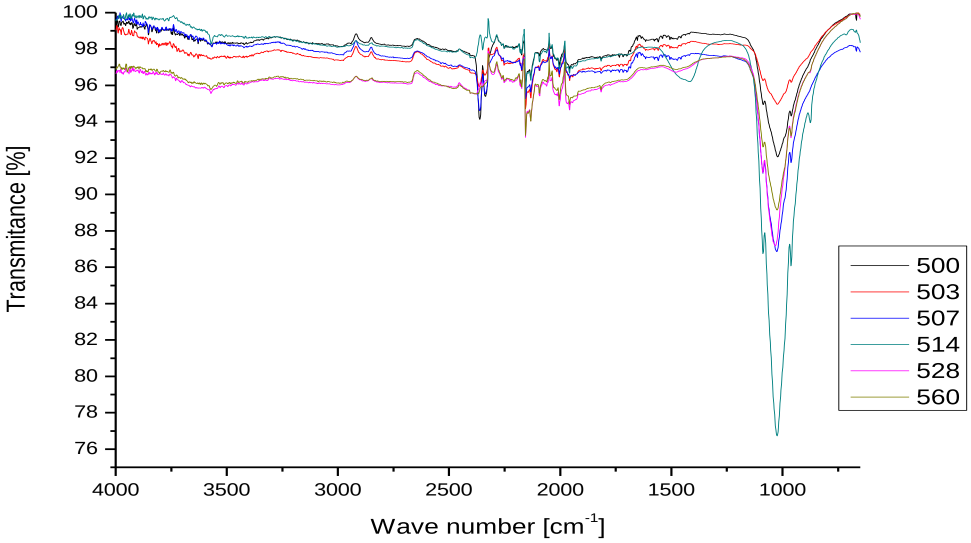

Figure 3.15 *IR spectra for samples series Exp No. 5.*

3.4.5 Micro-Raman analysis

Two series of samples were chosen for micro-Raman examinations. The previous results let one to choose samples series 2 and 5 for further investigation by other methods. The coatings were investigated at three or four points at the cross-section, i.e. one point adjacent to the substrate, two points in the middle of the coating and the last one close to the top of the coating. The marked points and the spectra corresponding to the samples 200, 207, 500,560, which were chosen as the most interesting are presented in Figures 3.16 - 3.19. The other micrographs and micro-Raman spectra are included in appendix (section 7.4).The substrate is always presented on the left hand side of the picture, then marked points on the coating and bright area on the right hand side correspond to epoxy resin.

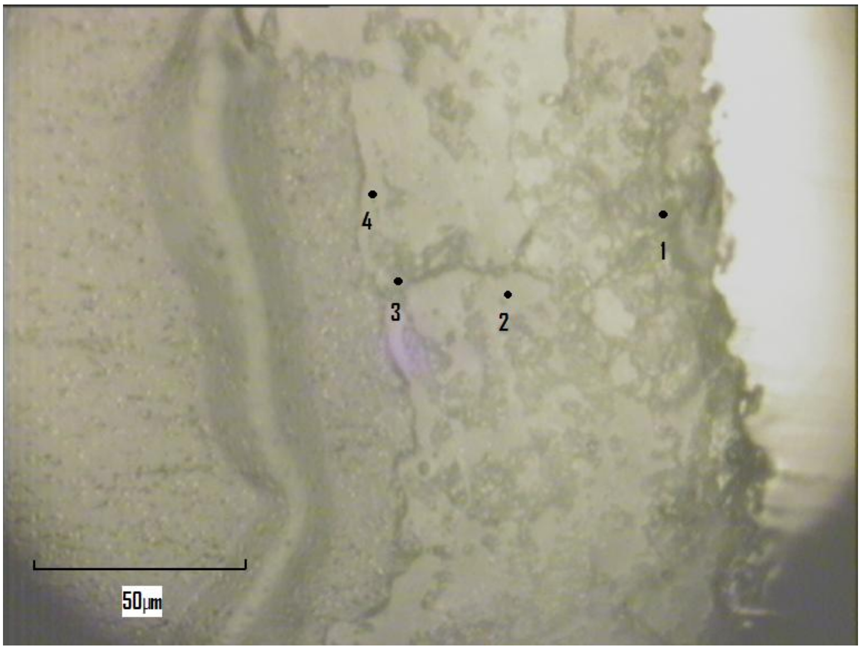

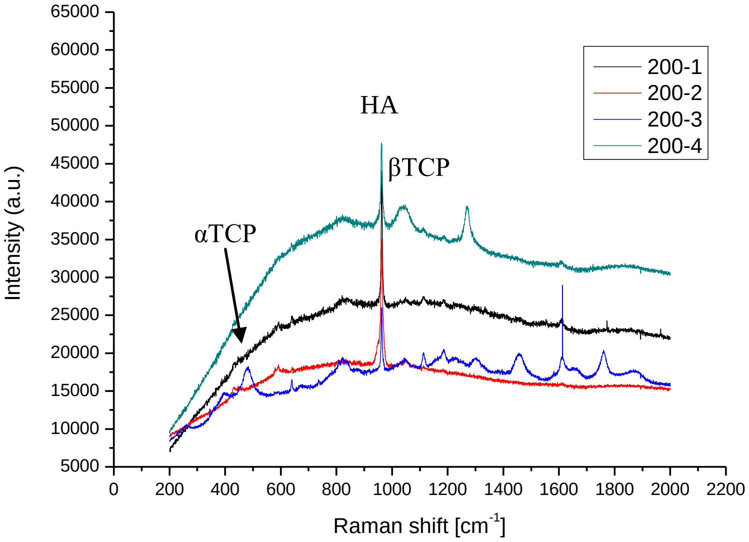

Figure 3.16 *Cross-section of sample 200 (top) and Raman spectra (down).*

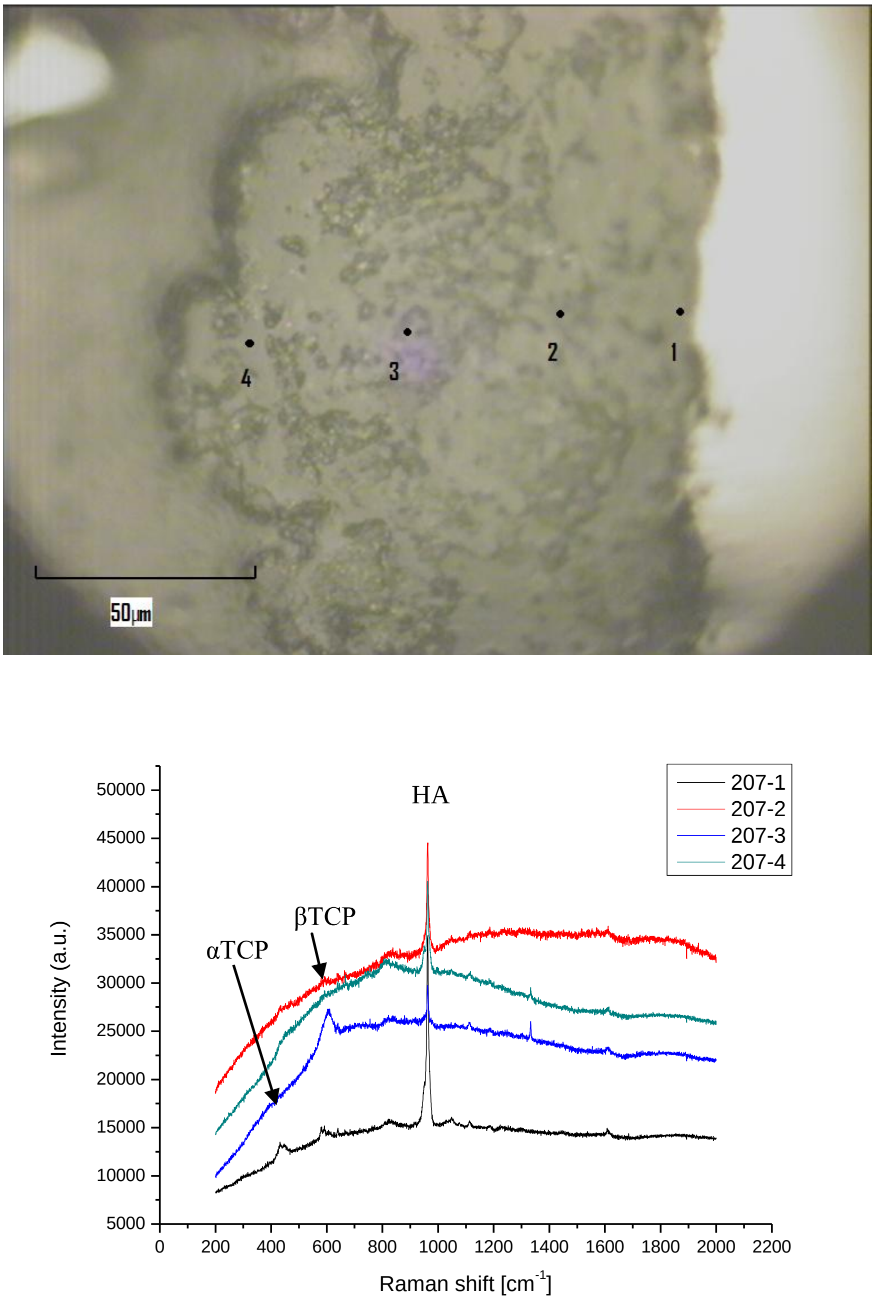

Figure 3.17 *Cross-section of sample 207 (top) and Raman spectra (down).*

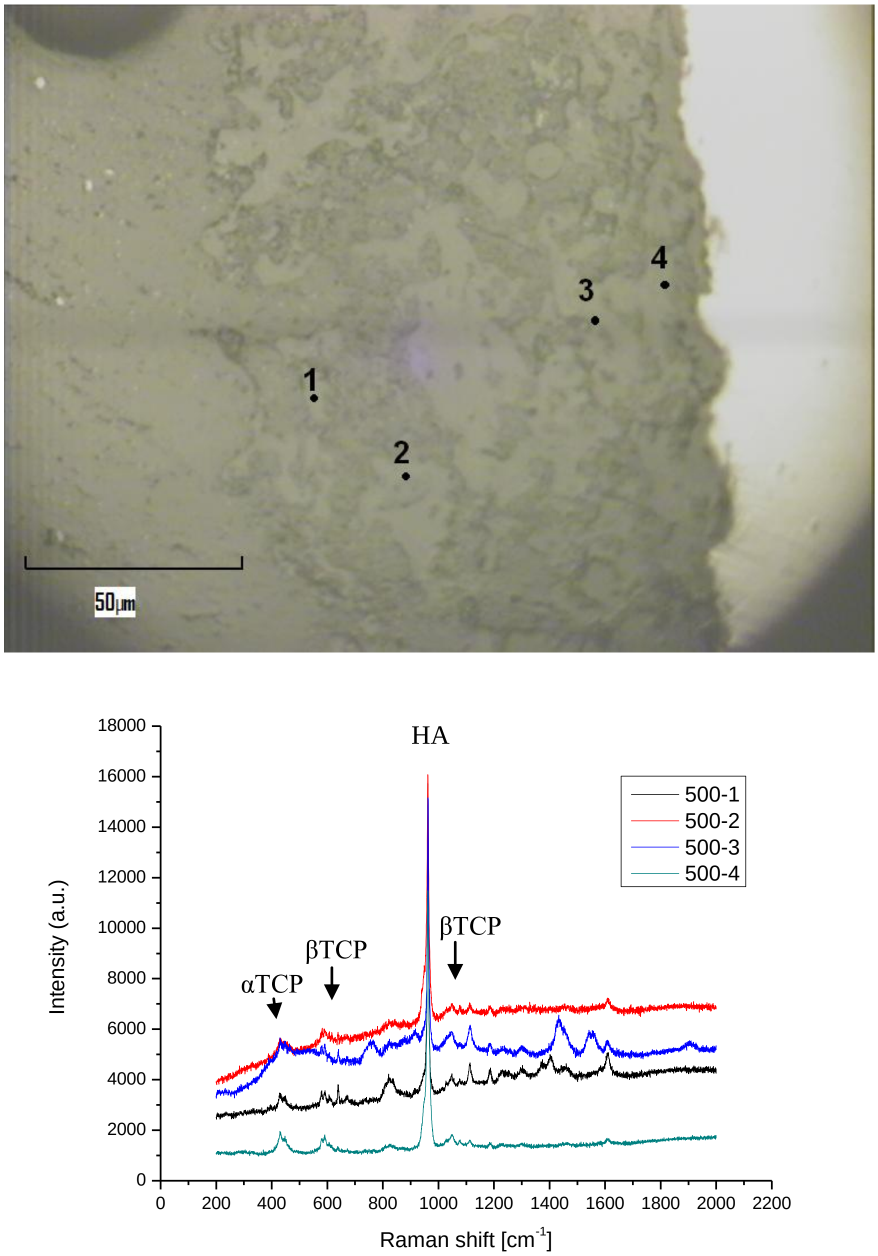

Figure 3.18 *Cross-section of sample 500 (top) and Raman spectra (down).*

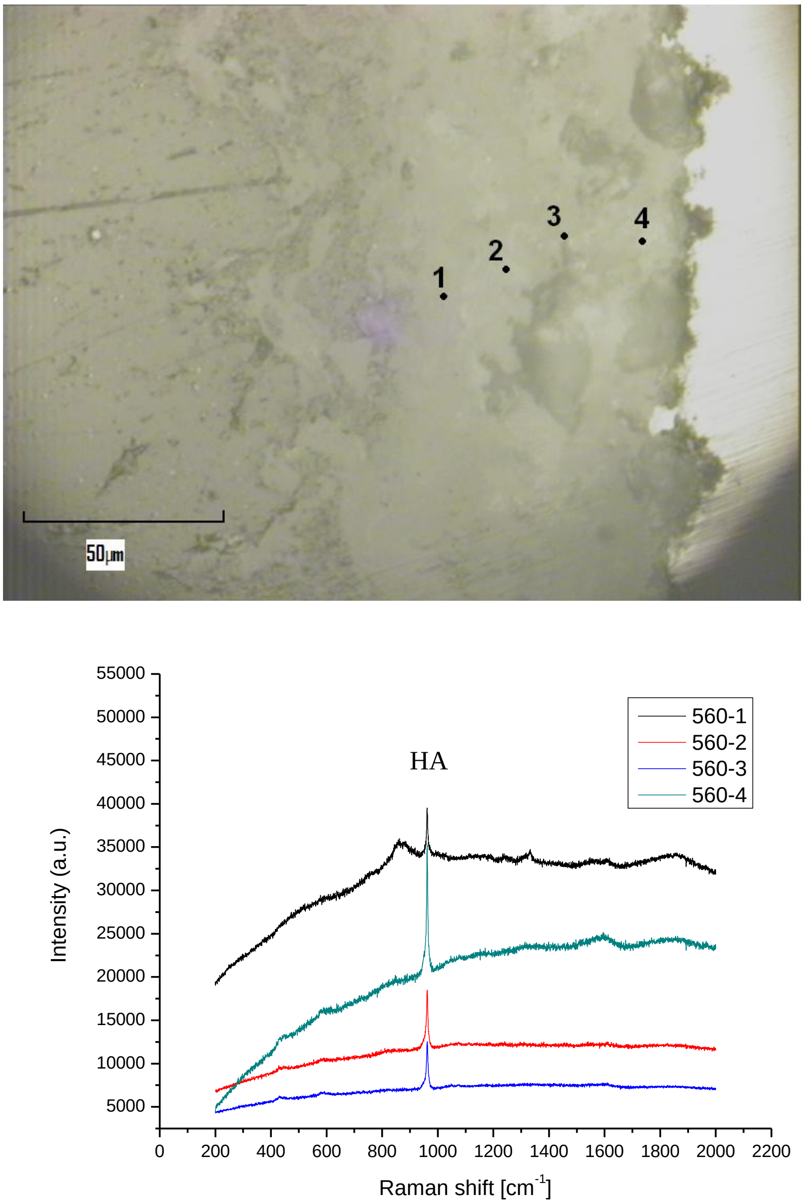

Figure 3.19 *Cross-section of sample 560 (top) and Raman spectra (down).*

The results presented above show that the BSF solution dissolves some phases in the top layer of the coating. Peaks of the phases α-TCP and β-TCP in the range from 400 cm^{-1} to 650 cm^{-1} and β-TCP in the range from 1020 cm^{-1} to 1080 cm^{-1} seem to be weaker after immersion in BSF. This is clearly seen in the case of samples 500 and 560. The change in the crystalline structure of the coatings is not significant, the width of the HA peaks (960 cm^{-1}) before and after immersion in the BSF are comparable.

3.4.6 Electron Micro-Probe Analyzer (EMPA) investigations

The sample series of experiment No. 2 were chosen to analysis. The samples cross-sections were put into the vacuum chamber in Cameca EMPA and then quantitative measurements of Ca and P content were done. Measurements were carried out along the red line marked on the presented samples. Some representative samples 200, 207 and 260 are shown in Figs. 3.20 - 3.22. The rest of samples photos and Ca/P ratios are included in appendix (section 7.5).

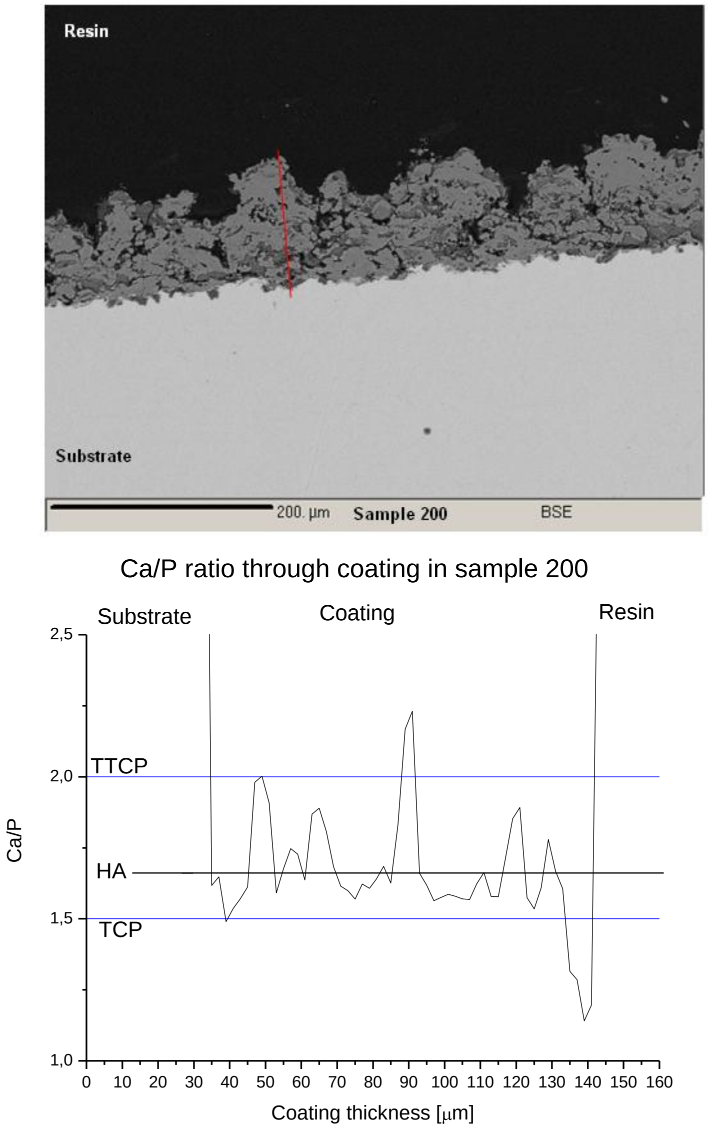

Figure 3.20 *Cross-section of 200 sample (top), and corresponding course of Ca/P ratio along marked line (down).*

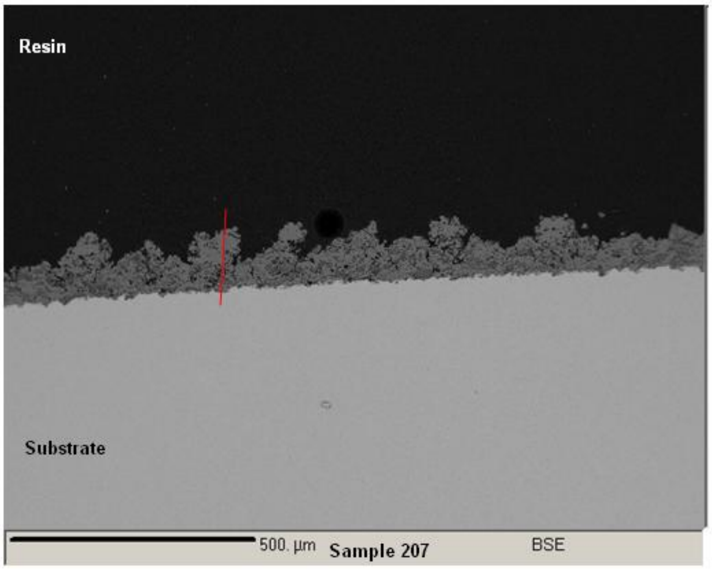

Ca/P ratio through coating in sample 207

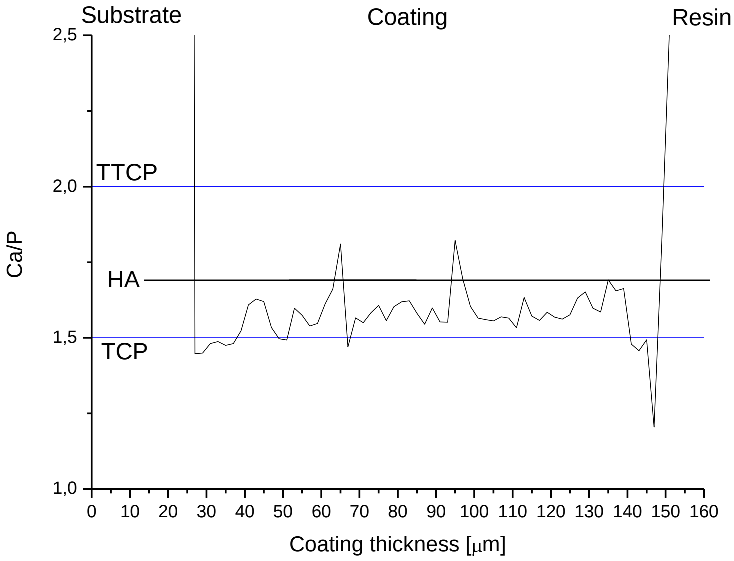

Figure 3.21 *Cross-section of 207 sample (top), and corresponding course of Ca/P ratio along marked line(down).*

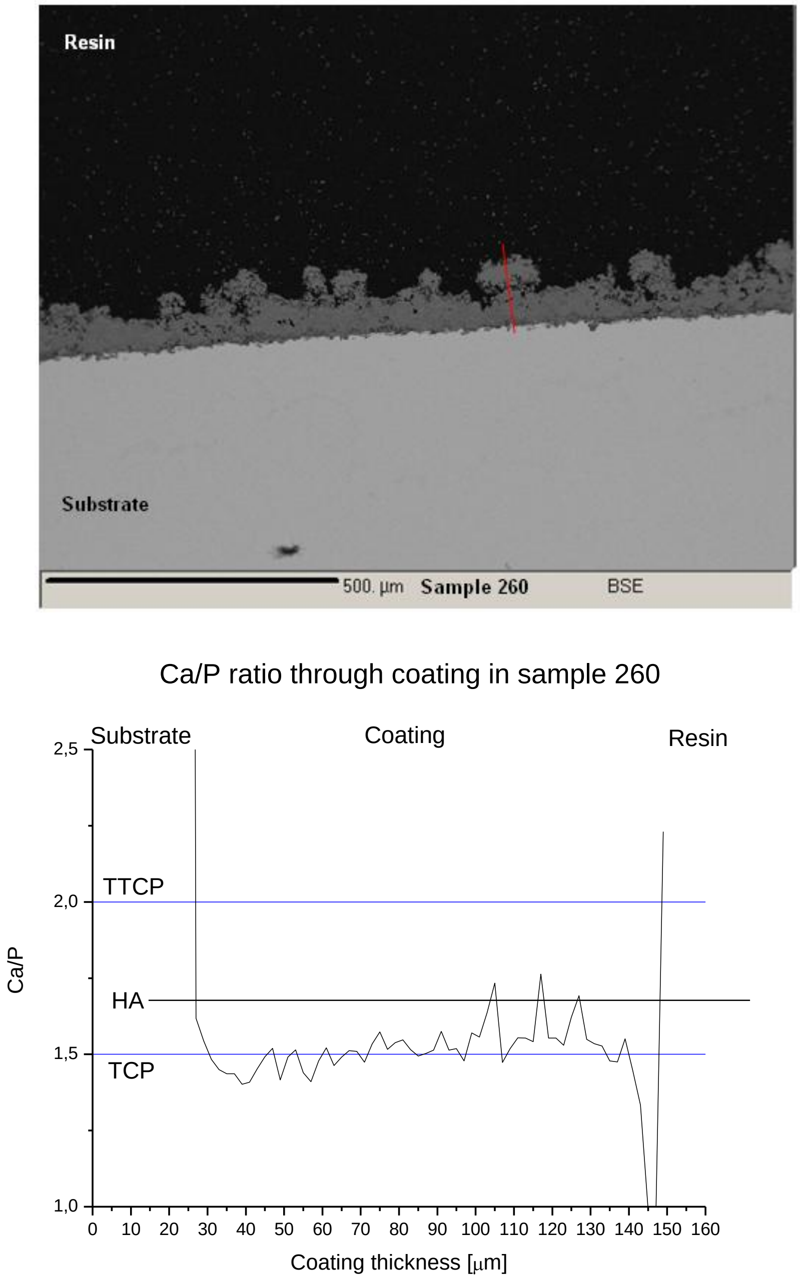

Figure 3.22 *Cross-section of 260 sample (top), and corresponding course of Ca/P ratio along marked line (down).*

The ratio Ca/P shows the composition of the coating i.e. if the value of Ca/P is equal to 1.66 it corresponds to pure HA (the Ca/P ratio comes from the chemical formula of the compound), value 1.5 is related to TCP phase (α and β). TTCP is presented by the Ca/P ratio equal to 2, and 4 value corresponds to the phase rich in CaO. The levels for different phases are drawn in the figures presented above. The sample 200 represented by mean Ca/P ratio is close to the value 1.66 of HA, but after immersion of samples 207 and 260 in BSF the mean Ca/P ratio is closer to 1.5. The results show that Ca/P ratio decreases with the time of immersion. It is caused by dissolution of the calcium phosphate (CP) phases followed by some decrease in the number of Ca atoms. The bound between the coating and resin or substrate is very porous what causes some upsetting close to the joint of the two different media.

3.4.7 Impedance Spectroscopy

To obtain the information about electrical properties of HA coatings as well as information about their microstructure the investigations by Impedance Spectroscopy (IS) were carried out. Those investigations concerned the samples with codes 100, 200, 300, 400 and 500, i.e. samples without immersing in BSF.

At the beginning a special preparation of the top electrode was required. It was done by painting a circle with a diameter of about 5 mm. For this operation a special conductive silver paint was used. The top view and cross section of the samples are shown in Figure 3.23.

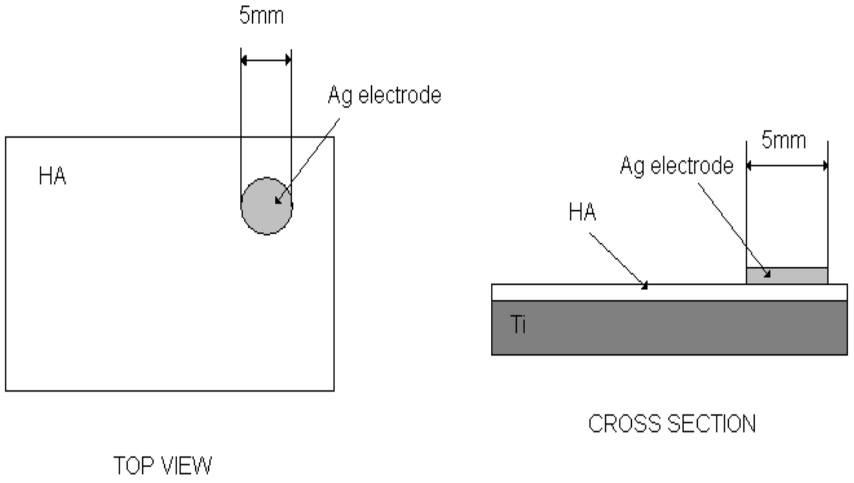

***Figure 3.23** The top view and cross-section of samples used for IS measurements.*

IS measurements were performed in the capacitor configuration, where HA coating was used as dielectric, metallic substrate was one cover, the second one was formed by the electrode painted on the coating. The capacity might be calculated according to well known formula:

$$C = \varepsilon_o \varepsilon_r \frac{s}{d} \qquad (3.2)$$

Two types of measurements were carried out. The first one was performed to obtain information about the dry HA electric properties and their dependence on temperature (Figure 3.24). Second one was performed to determine the porosity of the samples.

In the first measurements the samples series were heated up to 210°C and kept in that temperature for 30 min, to remove moisture from the surface and from the pores which were present in the coating. Then the group of impedance spectra were measured, in the frequency range from 40 Hz to 4 MHz at temperature ranging from 210°C to 30°C with 30°C steps.

The temperature dependence of dry HA coatings impedance spectra were similar in all samples. They behaved like capacitor with losses and with two dielectric relaxation processes, whose time constants (TC_1 and TC_2) depended on the temperature. One dielectric relaxation

(TC_1) was visible only at high temperature due to the limitations of impedance spectra bandwidth.

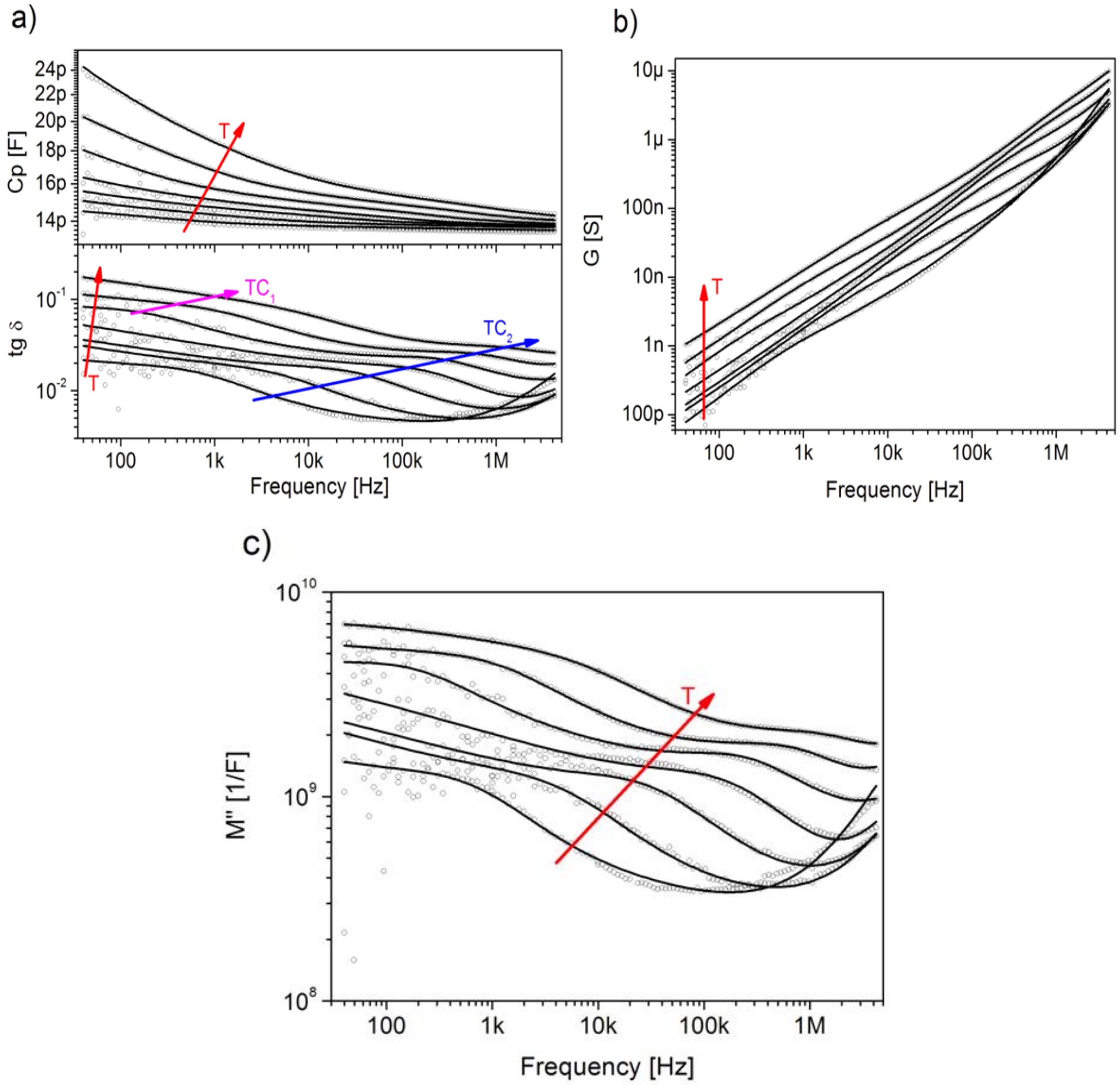

Figure 3.24 *Examples of measured impedance spectra (sample 100): a) parallel capacitance (C_p) and loss factor (tg δ), b) conductance (G), c) imaginary dielectric modulus (M'')* ***[97].***

The analysis of measured spectra was used to the modelling of electric equivalent circuit. The parallel equivalent circuit [98] was chosen (Figure 3.25).

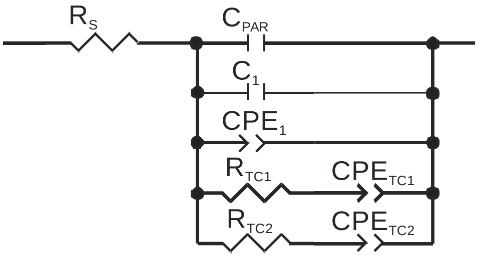

Figure 3.25 *The parallel equivalent circuit used in HA coatings analysis* ***[97].***

The equivalent circuit consisted of:

R_S, C_{PAR} – parasitic resistance and capacitance of the fixture and electrodes

$C_1 \parallel CPE_1$ – modelling crystalline and amorphous phases in bulk HA

R_{TC1} – CPE_{TC1}, R_{TC2} – CPE_{TC2} – modelling dielectric relaxations [99]

where the CPE is a constant phase element [100] which admittance is given by equation:

$$Y = Q \cdot (j\omega)^n \qquad (3.3)$$

Equivalent circuit was fitted to measured spectra at varying temperatures. Results of the fitting are shown in Figure 3.26.

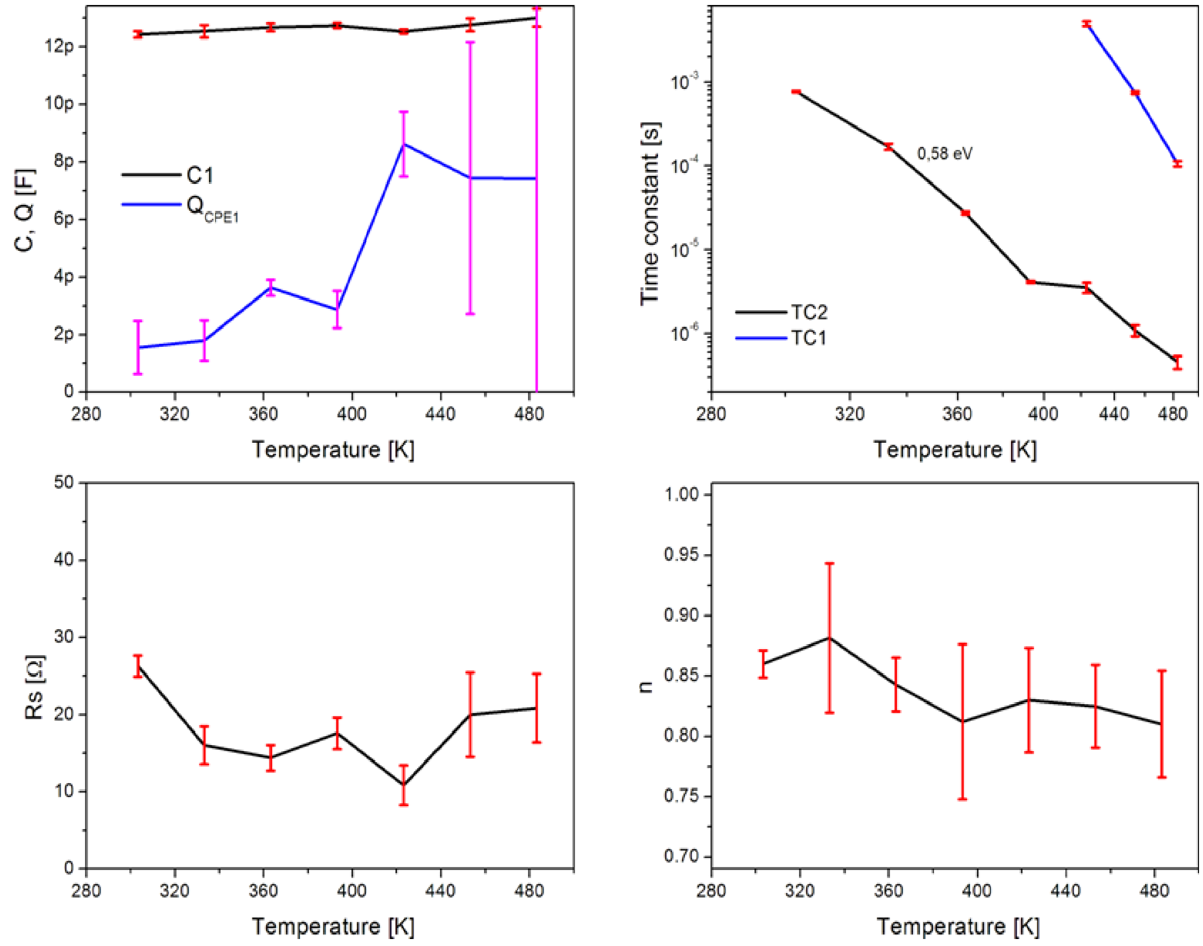

Figure 3.26 *The temperature dependence of model parameter values (sample 100): a) C1 capacitance and CPE1 Q - factor, b) time constants of dielectric relaxations, c) series resistance, d) CPE1 n – factor. Error bars correspond with fitting error* ***[97].***

All samples showed similar behaviour. Results of equivalent circuit analysis are shown in Table 3.16. The n-factors in the CPE_1 and CPE_{TC2} correspond to the amount of amorphous phase in the HA coating. HA coatings were highly defective, as activation energies (E_a) of dielectric relaxation in all samples were much lower than 2 eV reported as activation energy of conductivity in bulk HA [101].

Table 3.16 Results of equivalent circuit analysis.

Sample No.	CPE_1 n	E_a of TC2 [eV]	CPE_{TC2} n	drying time [s]
100	0.84	0.58	0.75	13.5
200	0.89	0.49	0.82	40.5
300	0.86	0.55	0.83	44.5
400	0.81	0.42	0.71	22.5
500	0.82	0.48	0.72	

Second measurement series was performed to determine the porosity of the samples. Special preparation before measurement was carried out i.e. the samples were immersed for 4 hours in deionized water at 60°C to saturate them with water. Then the sample was put on the heated table at 60°C and a number of fast, coarse impedance spectra in the frequency range from 200 Hz to 10 MHz were measured as the sample was drying and the water evaporating.

The impedance spectra of wet samples are shown in Figure 3.27 a. At low frequencies strong capacitance dispersion was visible.

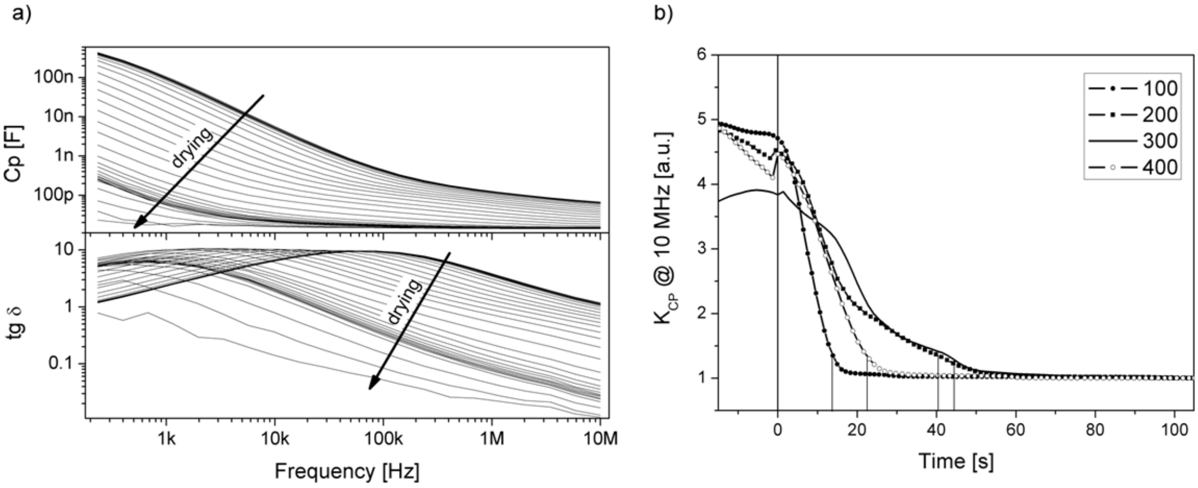

Figure 3.27 a) Changes of impedance spectra while sample drying, b) Capacitance at 10 MHz normalized to dry sample capacitance **[97]**.

The time t = 0 was the moment at which the impedance spectra of wet sample started to change due to the water evaporation. To illustrate the amount of water, the coefficient named K_{CP} was calculated according to the formula:

$$K_{CP} = \frac{C}{C_{dry}} \qquad (3.4)$$

where: C – the capacitance measured at 10 MHz while drying, C_{dry} – the capacitance of dry sample measured at 10 MHz

The amount of water absorbed by the HA coating was similar in all samples. The initial values of K_{CP} were comparable but drying time were different. The drying time was determined as the moment when the K_{CP}-1 dropped to the 10% of its original value.

SUMMARY OF THE HA COATINGS INVESTIGATIONS.

The hydroxyapatite coatings were investigated using micro-Raman spectroscopy, XRD, IS and EMPA. The preliminary test of the samples sprayed using ATM let one to state that the coatings were very porous with poor cohesion. It was probably caused by not sufficient evaporation of solvent from the part of particles not injected into plasma jet core. The analysis by XRD has shown that the phases of the hydroxyapatite decomposition occur. The most evident was αTCP.

The corrosion tests were done in Kokubo solution to observe the influence of the electrolyte environment on HA coatings. The time of the immersion was the variable, and was set up for 3, 7,14,28 and 60 days. The results of the XRD investigations have shown that the phases of hydroxyapatite decomposition undergo dissolution, and their percentage content was decreased with the increase of the immersion time.

The micro-Raman and EMPA confirmed also that the dissolution of the phase of decomposition took place. It was clearly seen on the Raman spectra of the samples series 5 and the decrease of the Ca/P ratio in the EMPA results.

The IS seems to be very interesting method of investigation in the analysis of porosity of the HA coatings. It revealed that the samples of series 2 and 3 had smaller pores with more complex microstructure. It was observed after IS measurements of the drying times of the HA coatings immersed in water.

3.5 PROPERTIES OF TITANIA COATINGS

3.5.1 Influence of spraying parameters on anatase phase content, coating thickness and anatase crystal sizes

Suspension used in the experiment was prepared from rutile TiO_2 powder (Tioxide R-TC90 of Huntsman) which was mixed with other ingredients in following proportions: 360g of distilled water, 40g of rutile, 0.12g of dispersant (Hydropalat N, Conigs). Granulometry of the powders used as suspension ingredients is shown in Figure 3.28 **[102]**. The geometry of atomizer/injector is shown in Figure 3.10 (right).

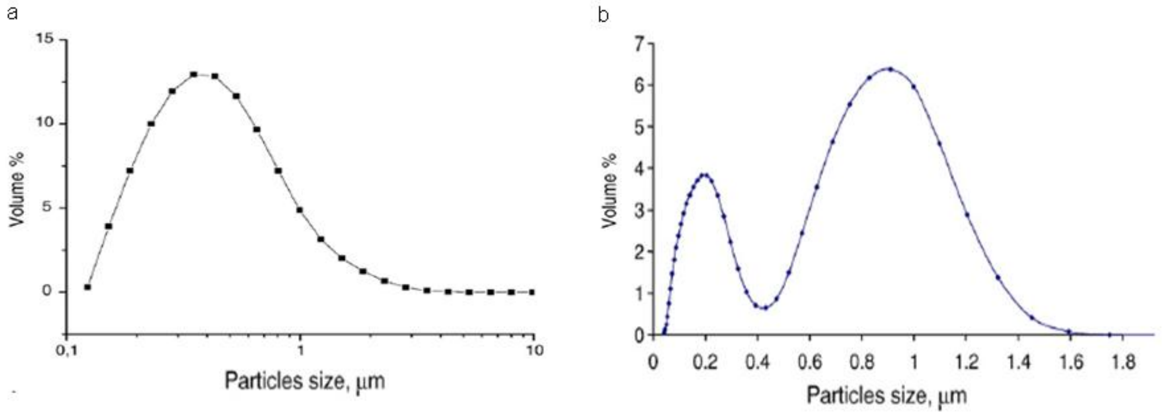

Figure 3.28 *Size distribution of rutile TiO_2 (Huntsman) powder (a) and anatase TiO_2 (Aldrich) powder (b)* ***[102].***

Injection of the suspension was realized using air as atomizing gas with a pressure of 0.6 bar, angle of injection $\alpha=90^0$, distance d=13mm, distance D=15mm (according to Figure 3.10).

The samples were sprayed onto aluminium plates (sand blasted) with dimensions 15x15x3mm. Some parameters, including plasma gases and their compositions - Ar and H_2 with 45splm and 5 slpm flow rates respectively were kept constant. Trajectory of plasma torch (according to Figure 3.10 left) was also the same for all experiments with linear velocity 500mm/s, 50 passages (5 cycles of 10 passages with 1 minute break for cooling down, between cycles). Three parameters were chosen as variables : X_1 – suspension feed rate, X_2 – spray distance, X_3 – power input to plasma. Experimental space is presented in Table. 3.17.

Table 3.17 Parameters of suspension plasma spraying.

Variable	Spray process parameter	Low level $X_i = -1$	Central point $X_i = 0$	High level $X_i = +1$
X_1	Suspension feed rate [ml/min]	20	30	40
X_2	Spray distance [mm]	80	100	120
X_3	Power input to plasma [kW]	38	39	40

Complete full factorial matrix (2^3) of plasma sprayed experiments using water-based suspension (T1-T8) and additional central experiments (T9-T10) are shown in Table 3.18.

Table 3.18 Matrix of sprayed experiment T1-T10 with corresponding variables levels.

Experiment No.	X_1	X_2	X_3
T1	-1	-1	-1
T2	1	-1	-1
T3	-1	1	-1
T4	1	1	-1
T5	-1	-1	1
T6	1	-1	1
T7	-1	1	1
T8	1	1	1
T9	0	0	0
T10	0	0	0

The effects of the process variables onto experimental responses were calculated according to the model valid in the experimental space presented in Table 3.18:

$$Y_m = b_0 + \sum b_i X_i + \sum b_{ij} X_i * X_j + b_{123} X_1 * X_2 * X_3 \qquad (3.5)$$

where i,j are equal to 1, 2, 3 and m can be equal to 1, 2 or 3, b_0 is the mean of responses of all experiments , b_{ij} and b_{123} are the coefficients which represent the effect of the variable interaction X_i*X_j and X_1*X_2*X_3 respectively.

Statistical analysis of the results of anatase content, coating thickness and anatase crystal sizes was carried out with Nemrod software [90]].

In order to calculate phase content, i.e. the peaks distribution, and to confirm the validity of the calculation method, preliminary tests of XRD analysis were carried out. The pure rutile powder (Huntsman) and anatase powder (99,8%, Aldrich) were analyzed by XRD, also three mixtures of powders were prepared and analyzed – rutile and anatase with changing composition from 75% (wt%) of anatase and 25% (wt %) of rutile to 25% of anatase and 75%(wt%) of rutile by 25% step. Then the calculations of phase content based on X-ray spectra were accomplished. The calculations were carried out according to formula[103]:

$$C_A = \frac{8I_A}{13I_R + 8I_A} \qquad (3.6)$$

where C_A is the content of anatase, I_A is intensity of anatase (101) peak, I_R is intensity of rutile (110) peak. Next this formula was corrected by taking into account different densities of two phases of TiO_2 in the following way:

$$C_{Acor} = \frac{8I_A/\rho_A}{\frac{13I_R}{\rho_R} + \frac{8I_A}{\rho_A}} \qquad (3.7)$$

where ρ_A is density of anatase (3.9g/cm^3) and ρ_R is density of rutile (4.2g/cm^3).

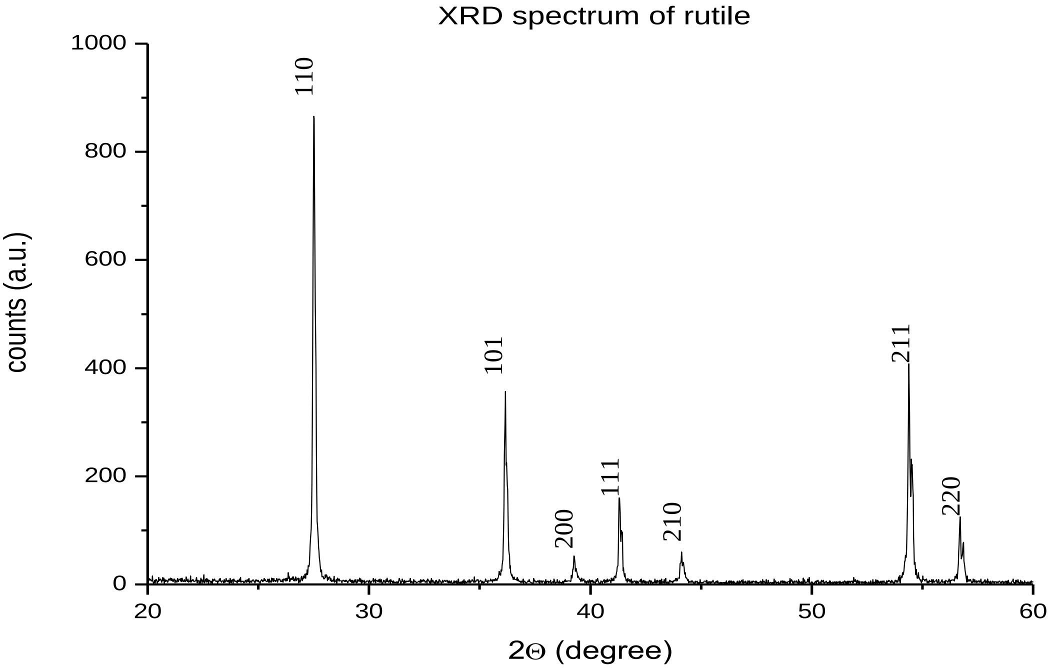

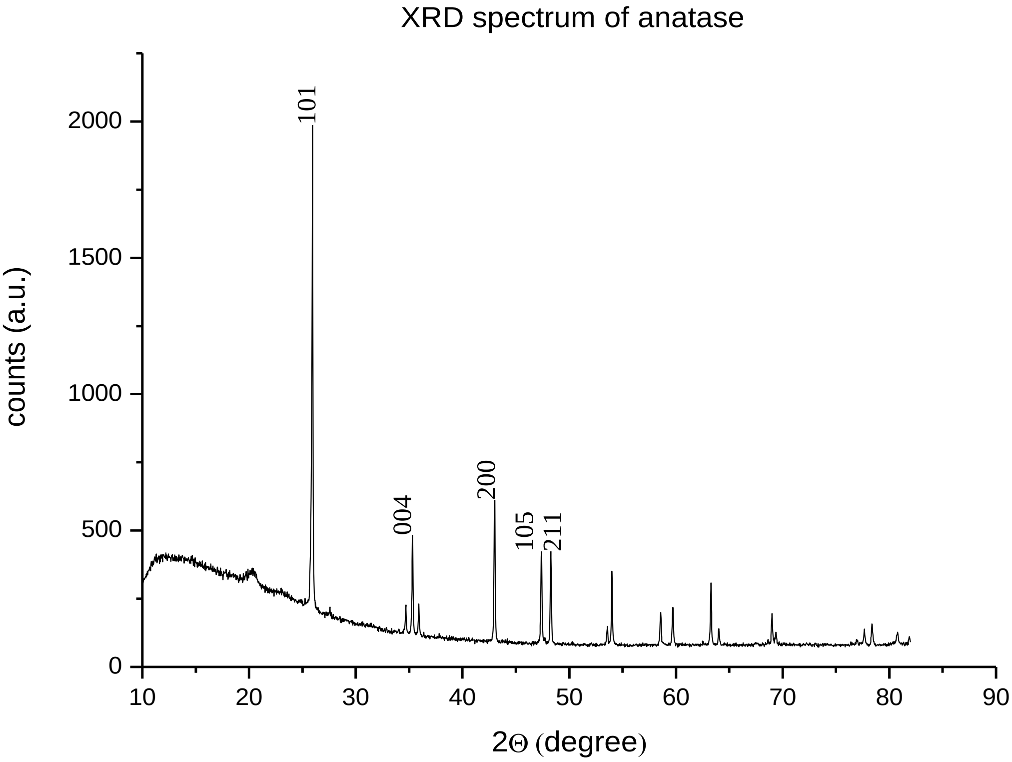

Figure 3.29 *The X-ray spectra of rutile (top) and anatase (bottom).*

Calculations of phase content (in wt%), which results are shown in Table 3.19, were carried out using heights and areas of the peaks.

Table 3.19 Comparison of the content of anatase (wt%) calculated by different methods

Mass fraction of anatase in tested mixtures	Analysis of peaks in X-ray diagrams			
	Peak height		Peak area	
	C_A	C_{Acor}	C_A	C_{Acor}
0.25	0.21	0.22	0.20	0.21
0.50	0.39	0.41	0.39	0.41
0.75	0.73	0.75	0.73	0.75

Results of anatase content calculations together with the results of calculations of coating thicknesses and sizes of anatase crystals calculations are presented in Table 3.20.

Table 3.20 Results of anatase content, thickness of coatings , size of anatase crystals for examined samples.

Experiment No.	Thickness of coatings [μm]	Fraction of anatase [wt%]	Size of anatase crystals [nm]
T1	29	9.4	95
T2	33	11.8	97
T3	11	13.8	105
T4	22	15.3	89
T5	8	9.7	85
T6	10	9.9	82
T7	10	15.4	98
T8	9	14.5	82
T9	-	13.1	-
T10	-	12.1	-

As response to the calculations, significant effects (by Student criterion taken at 95% confidence level and for degree of freedom depending on number of experiment, number of their repetitions and number of regression equation coefficients as shown by Lazic [87]) are presented. Next, the analysis was repeated using only significant active effects. Finally, the probability of activity of the effects was calculated.

Results of these calculations are graphically presented in Figure 3.30

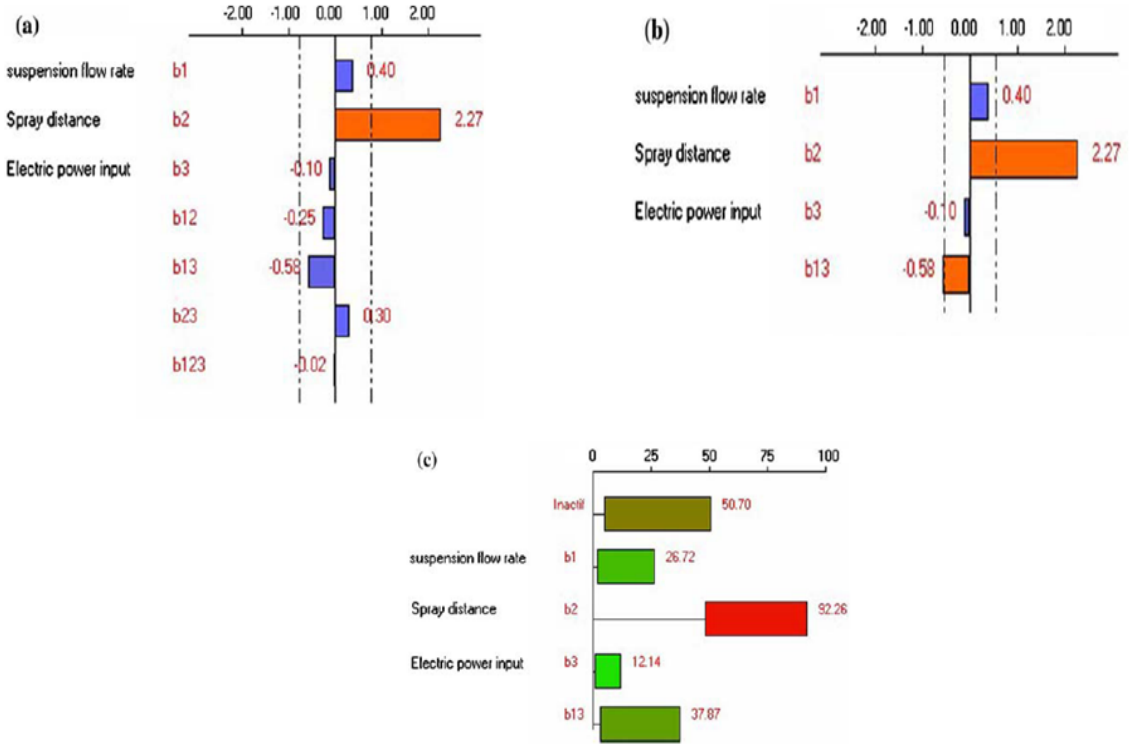

Figure 3.30 *Results of statistical analysis of active effects influencing the anatase fraction in sprayed coatings: regression equation coefficients for the model including all effects and their interaction of second and third order (a); refined regression equation coefficients for the most active effects (b); determination of probability that the effects in the refined regression equation are active (c)***[96].**

The initial analysis shows that only the value of coefficient b_2 is higher than 95% significance level (Figure 3.30a)). The refined analysis with regression equation limited to three principal variables and one interaction i.e. X_1*X_3, shows that b_{13} value exceeds somewhat the significance level (Figure 3.30b)). The third stage of calculations i.e. determination of probability of the effects activity shows that for b_{13} interaction this value is lower than 50% (Figure 3.30c)) and may be neglected. The final regression equation has the following form:

$$Y_1 = b_0 + b_2X_2 = 12.5 + 2.3X_2 \qquad (3.8)$$

The second part of investigations concerned the influence of spraying parameters on coating thickness. Metalographically prepared cross-sections of all samples were visualized using Olympus optical microscope CK40M with camera Camedia 3040 and their thicknesses were determined using DP-SOFT 5.0. An example of the thickness determination is shown in Figure 3.31.

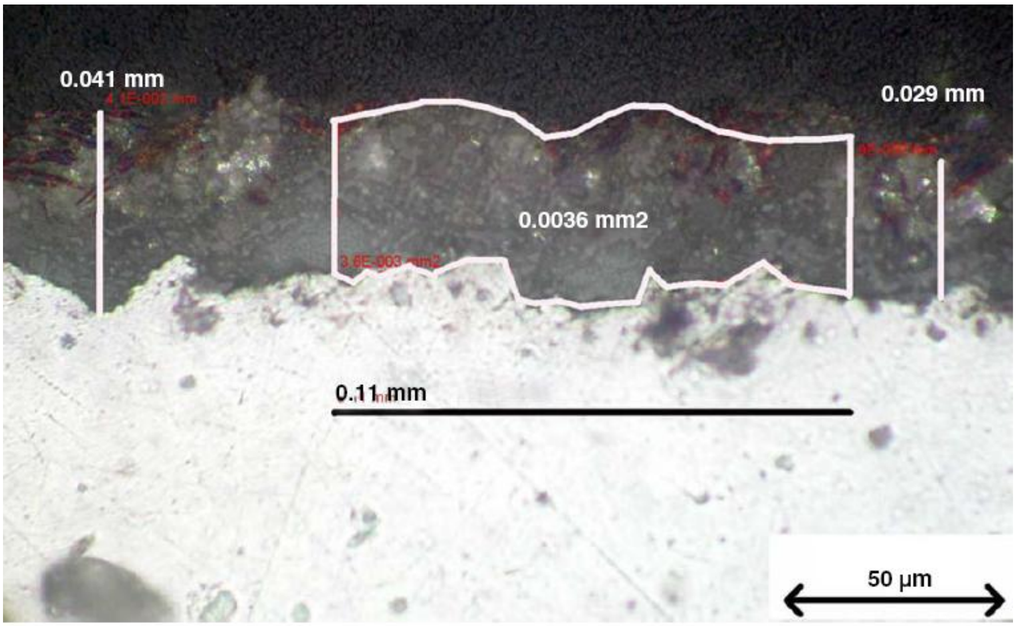

Figure 3.31** Example of thickness determination using DP-SOFT 5.0 software* ***[96].

Results of statistical analysis performed for thicknesses are shown in Figure 3.32.

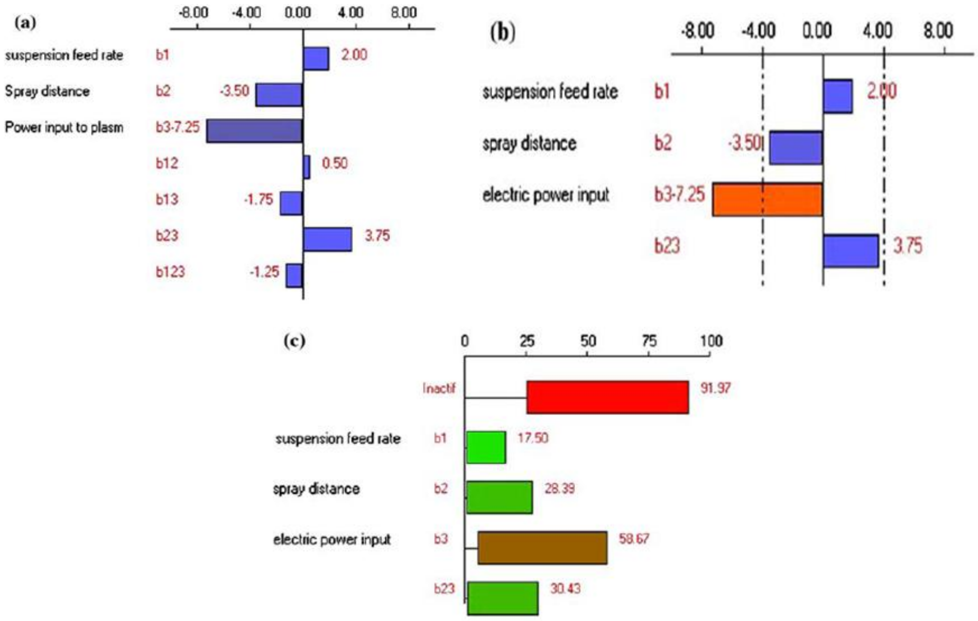

Figure 3.32** Results of statistical analysis of the active effects influencing coating thickness: regression equation coefficients for the model including all effects and their interactions of second and third order (a); refined regression equation coefficients for the most active effects (b); determination of probability that the effects in the refined regression equation are active (c)*[96].***

The initial analysis indicates that neither of coefficients in the regression equation exceeds 95% significance level. (Figure 3.32a). The analysis limited to three principal effects and X_2*X_3 interaction enabled us to find out that the effect b_3 of electric power input to plasma is significant what was confirmed by the probability calculation (Figure 3.32b, c)

Final equation for the influence of spraying parameters on coating thickness takes the form :

$$Y_2 = b_0 + b_3 X_3 = 16.5 - 7.3 X_3 \qquad (3.9)$$

In the third part of our investigations the sizes of anatase crystals (Table 3.21) were calculated on the basis of Laue-Scherrer equation :

$$D_{hkl} = \frac{k\lambda}{\beta \cos\Theta} \text{ [Å]} \qquad (3.10)$$

Where:
k – coefficient of crystallite form = Scherrer constant ≈ 0,9
λ - wave length 1,5406Å
β – full width in half height of Bragg peak β_m, corrected by device deviation β_0
$\beta = \beta_m - \beta_0$
2Θ - angle of scan

Table 3.22 shows device deviation for corresponding 2Θ angle values.

Table 3.21 Deviation of Bruker device.

2Θ	Deviation β_0
25	0.045
35	0.046
37	0.046
43	0.048
52	0.052
57	0.055
61	0.055
66	0.055
68	0.056
76	0.058
77	0.061
89	0.068
90	0.071
91	0.075
95	0.077

Results of statistical analysis of spraying parameters influence on anatase crystals size are shown in Figure 3.33.

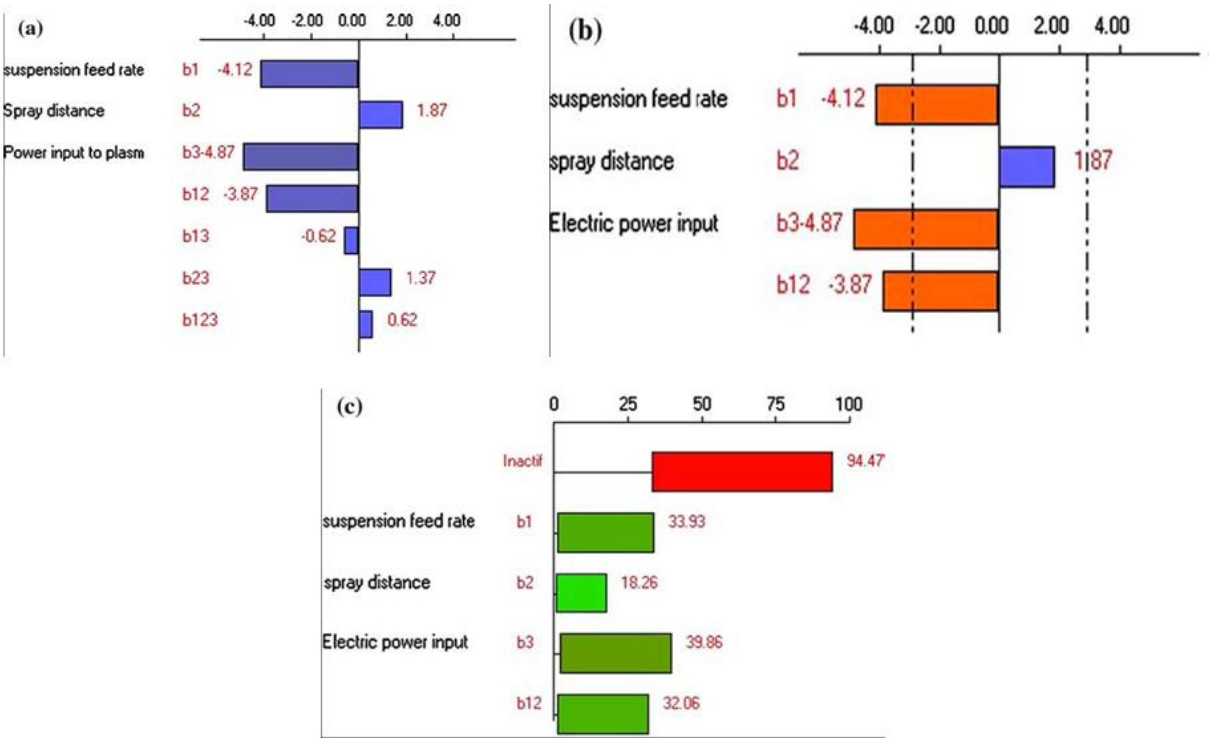

Figure 3.33 *Results of statistical analysis of active effects influencing anatase crystal size in sprayed deposits: regression equation coefficients for a model including all effects and their interaction of second and third order (a); refined regression equation coefficients for the most active effects (b); determination of probability that the effects in the refined regression equation are active (c)* ***[96].***

The initial and refined analysis show that the coefficients b_1,b_3 and b_{12} can be significant (Figure 3.33 a, b). Probability of those effects is lower than 50% what indicates that the influence of spraying parameters on the anatase crystal size may be neglected.

3.5.2 Influence of spraying parameters on mechanical properties of titania - scratch test

This investigation was applied to the samples used in 3.4.1 section. During each spraying experiment i.e. T1 to T10 three samples were sprayed in the same time. One sample was taken to XRD investigation followed by SEM observation of sample surface, the second one was destined for cross-section observation, the third sample was assigned to scratch test what will be described in this section.

Preparation of the samples used for the scratch test has been widely described in section 3.4.1. The scratch test was used for estimation of adhesion of the coatings sprayed by SPS with different parameters according to full factorial 2^3 plan of experiments enabling statistical data treatment. The scratches were linear with progressively increasing load. Increase of the load was accompanied by micro-cracks generation along the way of indenter in different directions. In the case of investigated coatings the micro-cracks were perpendicular to the scratch direction (Figure 3.34).

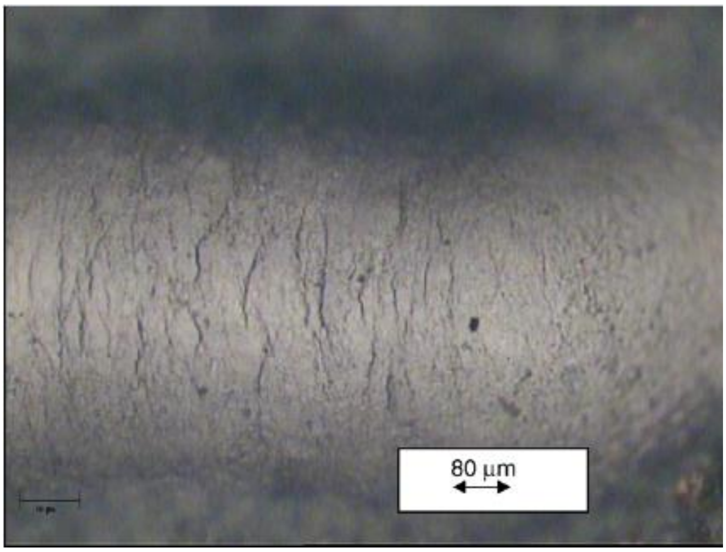

Figure 3.34 *Optical microscope view of micro-cracks generated during scratch test* ***[102].***

Experimental conditions of scratch test are presented in Table 3.23.

Table 3.22 Parameters used in scratch test.

Parameter		Value
Initial load	[N]	0.05
Final load	[N]	30
Rate of load increase,	[N/min]	15
Speed of indenter,	[mm/min]	5.22
Scratch length,	[mm]	10

Typical scratch curve is presented in Figure 3.35.

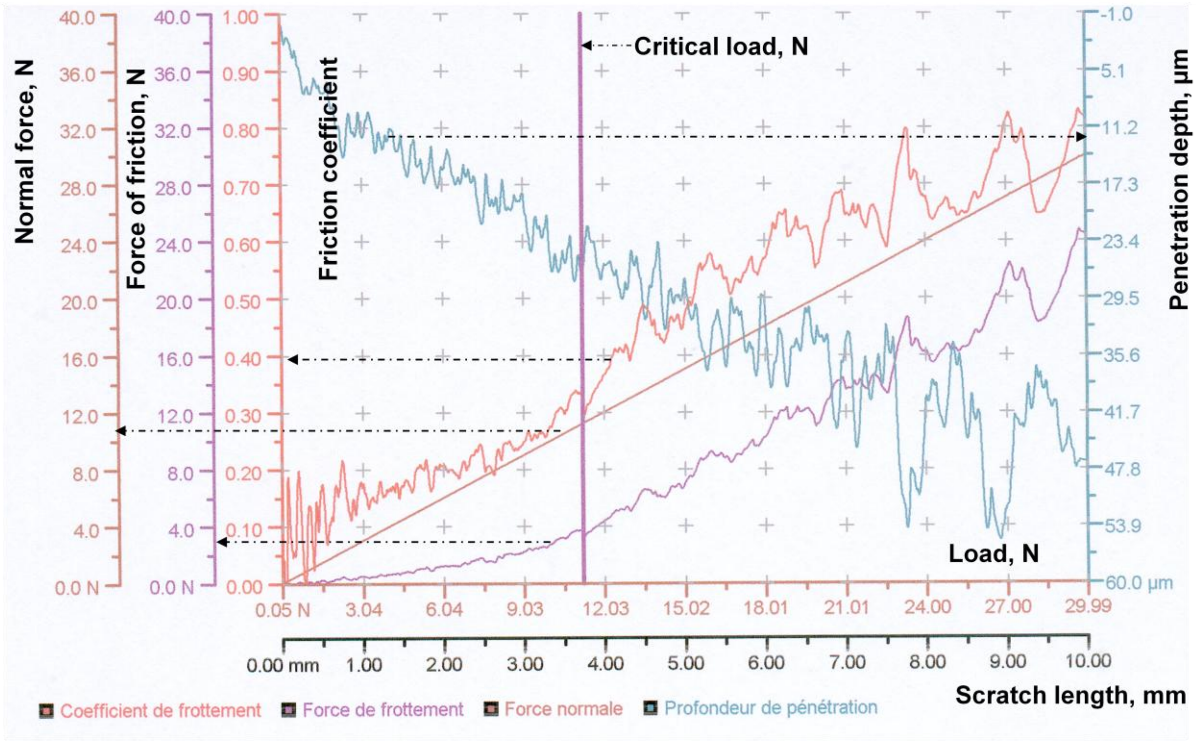

Figure 3.35 *Typical scratch curve obtained for the sample T1 with the critical load of $L_c = 11.2$ N* ***[102].***

The value of critical load L_C is defined as the load when a coating is broken, what is associated with appearance of metallic substrate inside the channel scratched by indenter (the tip radius 0.2 mm). Observations by optical microscope are necessary to examine this run. The scratch test enabled us also to assess the friction coefficient at the critical load. The scratch hardness HS_L was estimated following the specification of ASTM G171-03 norm:

$$HS_L = \frac{8L}{\pi d^2} \qquad (3.11)$$

where L [N] is applied normal force, d[m] is scratch width. The scratch hardness may be an indicator of coating cohesion.

Results of mechanical parameters investigations are collected in Table 3.23. The run for T1 sample was repeated twice. Observations made by optical microscope showing scratch channels for T6 and anatase coating are presented in Figure 3.36.

Table 3.23 Results of mechanical properties investigations for plasma sprayed coatings deposited by using suspension of rutile (T1-T9) and anatase.

Experiment No.	Critical load, L_C [N]		Friction coefficient [a]		Hardness, HS_{Lc}	
	Mean value	Standard deviation	Mean value	Standard deviation	Mean value	Standard deviation
T1	10.68	0.47	0.29	0.04	0.64	0.10
First repeat for T1	12.99	0.66	0.27	0.00	0.73	0.06
Second repeat for T1	13.93	1.31	0.29	0.06	0.76	0.05
T2	13.10	1.23	0.37	0.05	0.59	0.02
T3	10.15	1.96	0.27	0.04	0.60	0.07
T4	12.64	0.34	0.31	0.02	0.58	0.03
T5	14.49	1.35	0.34	0.06	0.66	0.06
T6	16.56	2.10	0.38	0.04	0.65	0.04
T7	10.55	0.85	0.27	0.05	0.69	0.04
T8	11.08	0.09	0.27	0.01	0.68	0.05
T9	11.54	1.01	0.27	0.04	0.71	0.04
Anatase sample	>30	-	0.11	0.01	3.6 [b]	0.03

[a] At critical load, [b] At 30 N.

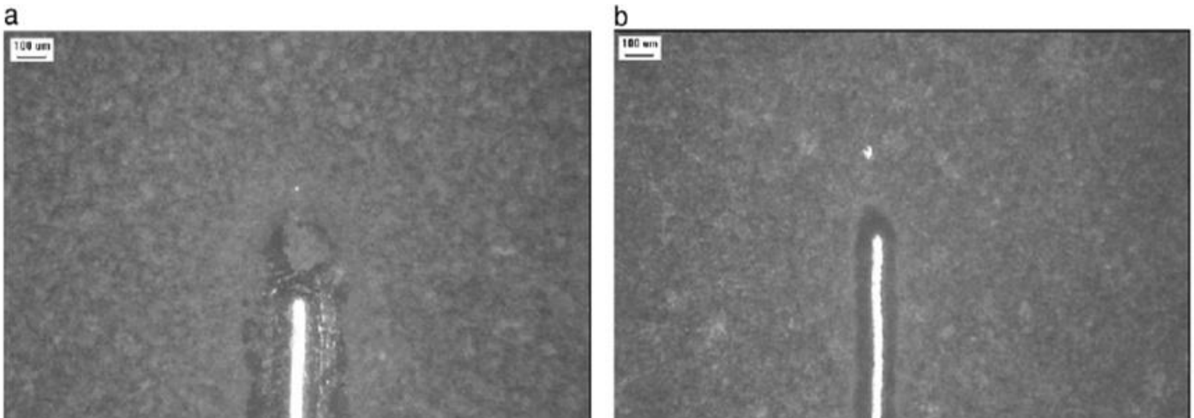

Figure 3.36 Optical microscope images of scratch channels: for T6 (a) and for anatase coating (b).

Statistical analysis was carried out with Nemrod software (the same as in section 3.4.1) Its results are presented in three diagrams. Statistical analysis of critical load is shown in Figure 3.37.

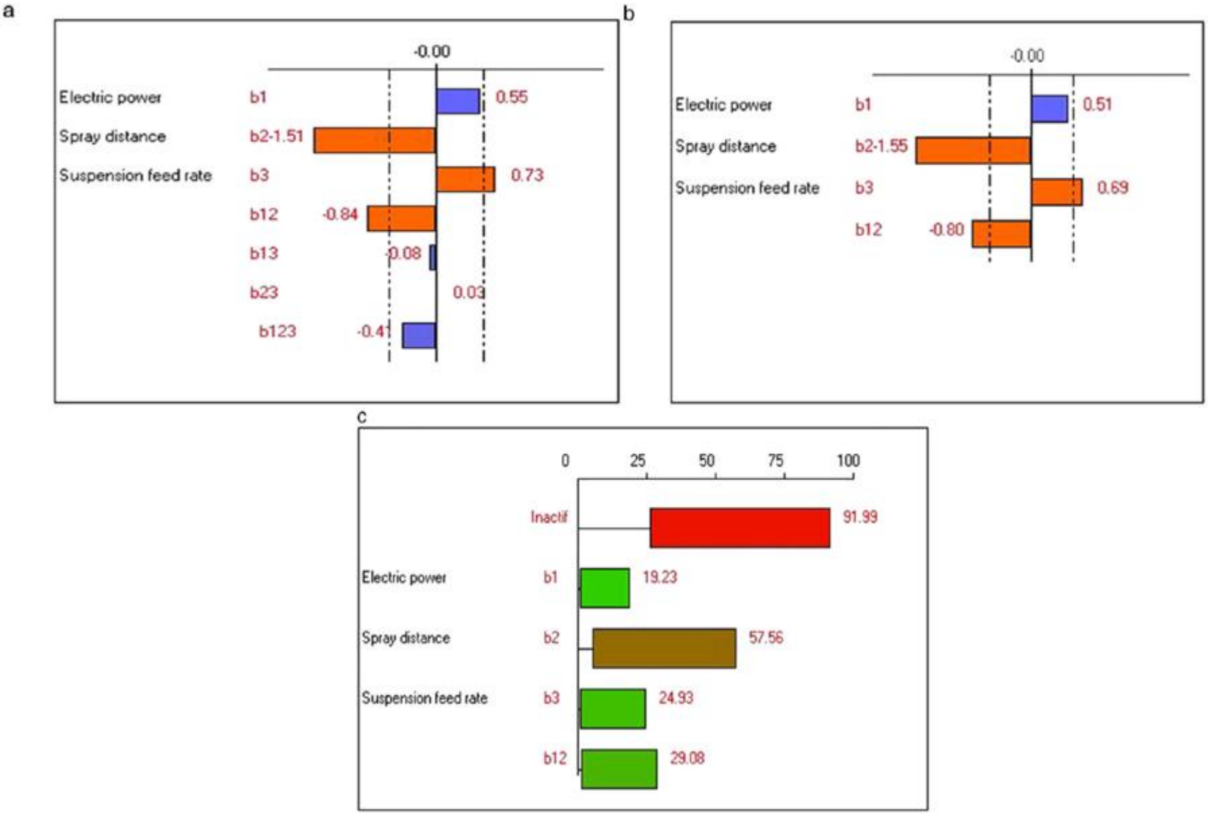

Figure 3.37. *Results of statistical analysis of active effects influencing critical load in scratch test of coatings obtained by suspension plasma spraying using rutile: regression equation coefficients for the model including all effects and their interaction of second and third order (a); refined regression equation coefficients for the most active effects (b); determination of the probability that the effect in the refined regression equation is active (c)**[102].***

The initial analysis shows that b_2, b_3 and b_{12} are greater than 95% significance level. (Figure3.37a). After refined analysis again b_2, b_3 and b_{12} exceeded again the significance level (Figure 3.37b). Finally probability calculations (Figure 3.37c)showed that only spray distance coefficient had a value higher than 50% and only this parameter was taken into consideration in final regression equation which has the following form:

$$Y_1 = b_0 + b_2X_2 = 12.5 - 1.5X_2 \qquad (3.12)$$

Statistical analysis of hardness is shown in Figure 3.38.

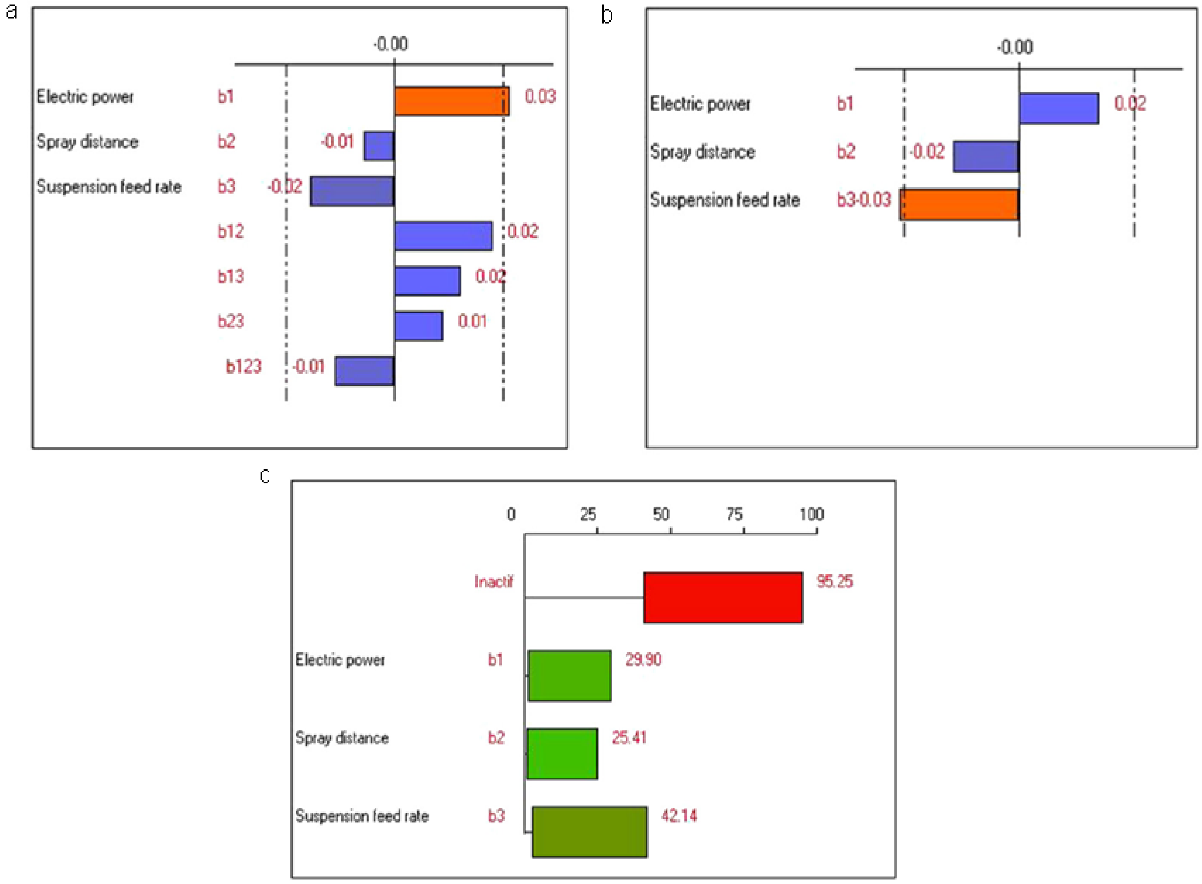

Figure 3.38 *Results of statistical analysis of active effects influencing scratch hardness of coatings obtained by suspension plasma spraying using rutile: regression equation coefficients for a model including all effects and their interaction of second and third order (a); refined regression equation coefficients for the most active effects (b); determination of the probability that the effect in the refined regression equation is active (c)****[102].***

The initial analysis shows that b_1 effect is higher than 95% of significance level (Figure3.38 a.), but refined analysis with the calculation of three principal effects showed that only coefficient b_3 exceeded the significance level (Figure 3.38 b). The probability calculations revealed that no significant effects of selected variables influence the scratch hardness (Figure 3.38 c).

3.5.3. Microstructural study of TiO_2 coatings

This section includes the results of titania coatings microstructure study using micro-Raman spectroscopy and some TEM and SEM observations. The examined samples were chosen from previously sprayed samples (T1 – T10) described in section 3.4.1. However the samples were sprayed additionally with suspensions using different solvents (Table 3.24.) and with some changes in suspension injection parameters (geometry and denotation see Figure3.10 b)(Table 3.25) were also included.

Table 3.24 Composition of TiO_2 suspension used in spraying experiments.

Sample name	Suspension composition
T1-T11	360g distilled water + 40g rutile+0.12g dispersant
T01-T02	360g (distilled water +50vol% ethanol) + 40g rutile+0.12g dispersant
T03-T04	360g ethanol + 40g rutile
T05-T06	284g ethanol + 40g rutile

Table 3.25 Parameters of suspension injection.

Experiment No.	Atomizing gas	Atomizing gas pressure [bar]	Angle of injection, α, [^{0}]	Distance from plasma torch face, d, [mm]	Distance from plasma axis, D, [mm]
T1-T10	Air	0.6	90	13	15
T11	Air	0.4	90	11.5	15
T01	Air	0.6	100	11	15
T02	Air	0.6	100	11	12
T03	Air	0.6	100	11	15
T04	Air	0.6	100	11	15
T05	Air	0.5	100	11	11
T06	Air	0.7	100	11	11

Plasma spraying parameters for all investigated samples are shown in Table 3.26, Some parameters were kept constant for all experiments and are described in section 3.4.1.

Table 3.26 Plasma spraying parameters for all samples used for investigation in this section.

Experiment No.	Suspension feed rate [ml/min]	Spray distance, [cm]	Power input to plasma, [kW]
T1	20	8	38
T2	40	8	38
T3	20	12	38
T4	40	12	38
T5	20	8	40
T6	40	8	40
T7	20	12	40
T8	40	12	40
T9	20	10	39
T10	40	10	39
T11	25	10	40
T01-T02	30	10	38
T03	20	12	30
T04	20	10	30
T05-T06	20	12	40

Raman spectroscopy was employed to characterize the coatings sprayed from aqueous suspension, ethanol suspension and mixture of water and ethanol suspension. For those investigations, the samples were put into epoxy resin (Epofix, Struers), then cut transversely in the middle and polished. Because of poor coatings cohesion, the polished section was glued to prevent spalling of coating grains. At first, the spectra of resin and glue, shown in Figure 3.39 and Figure 3.40 were measured.

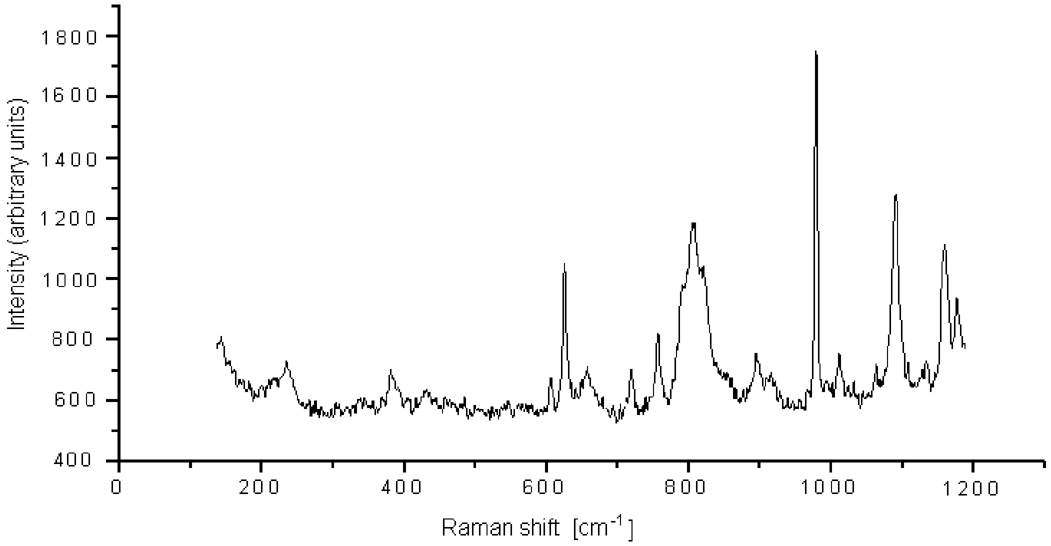

Figure 3.39 *Raman spectra of epoxy resin.*

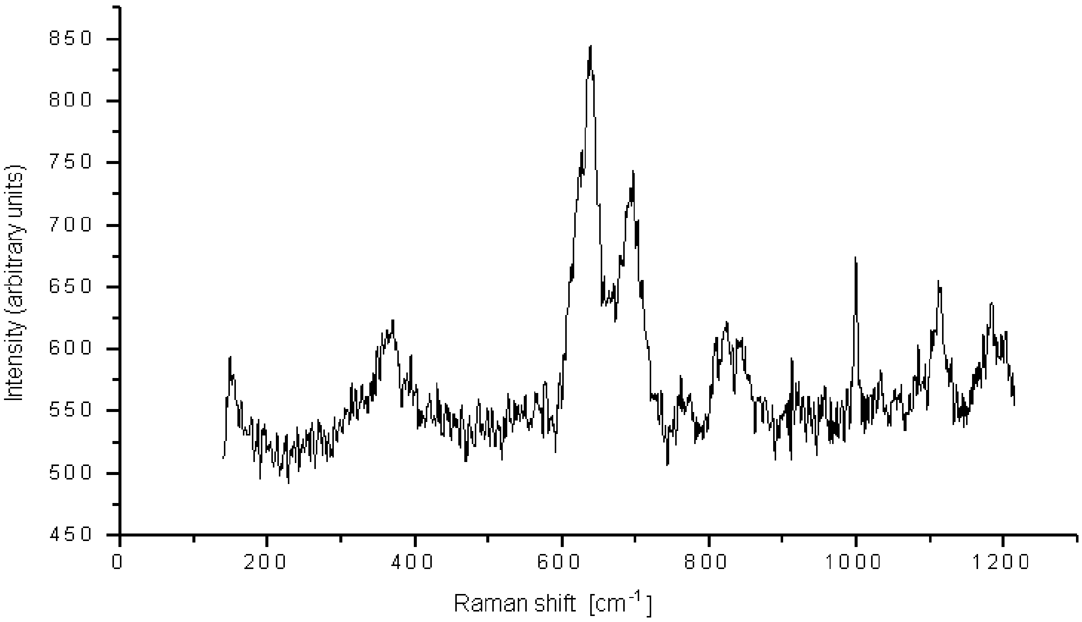

Figure 3.40 *Raman spectra of the glue.*

Each sample was observed with an optical microscope to choose potentially interesting sites and then laser beam was positioned. Three sites in the coating were examined i.e. interface between the coating and substrate, one point in the middle zone of the coating and the last one at the coating top. The following phases of TiO_2 were identified [104]:

- anatase with characteristic modes at the wave numbers of 144 (strong), 198 (weak), 399 (weak), 516 (weak), 640 (strong) [cm^{-1}]

- rutile with characteristic modes at the wave numbers of 143 (weak), 240 (weak), 447(strong) and 612(strong) [cm^{-1}]

On the Raman spectra presented below (Figures 3.41 - 3.43) anatase and rutile peaks are marked as A and R, respectively and the mixture of rutile and anatase is marked as R+A. Three samples considered as interesting and representative are presented as examples of Raman measurements. Samples T1 and T7 are shown as representatives of the samples made by SPS of aqueous suspension (Figure 3.41 and Figure 3.42). Sample T02 was chosen as a representative of the samples made by SPS of alcoholic suspension and it is shown in Figure 3.43.

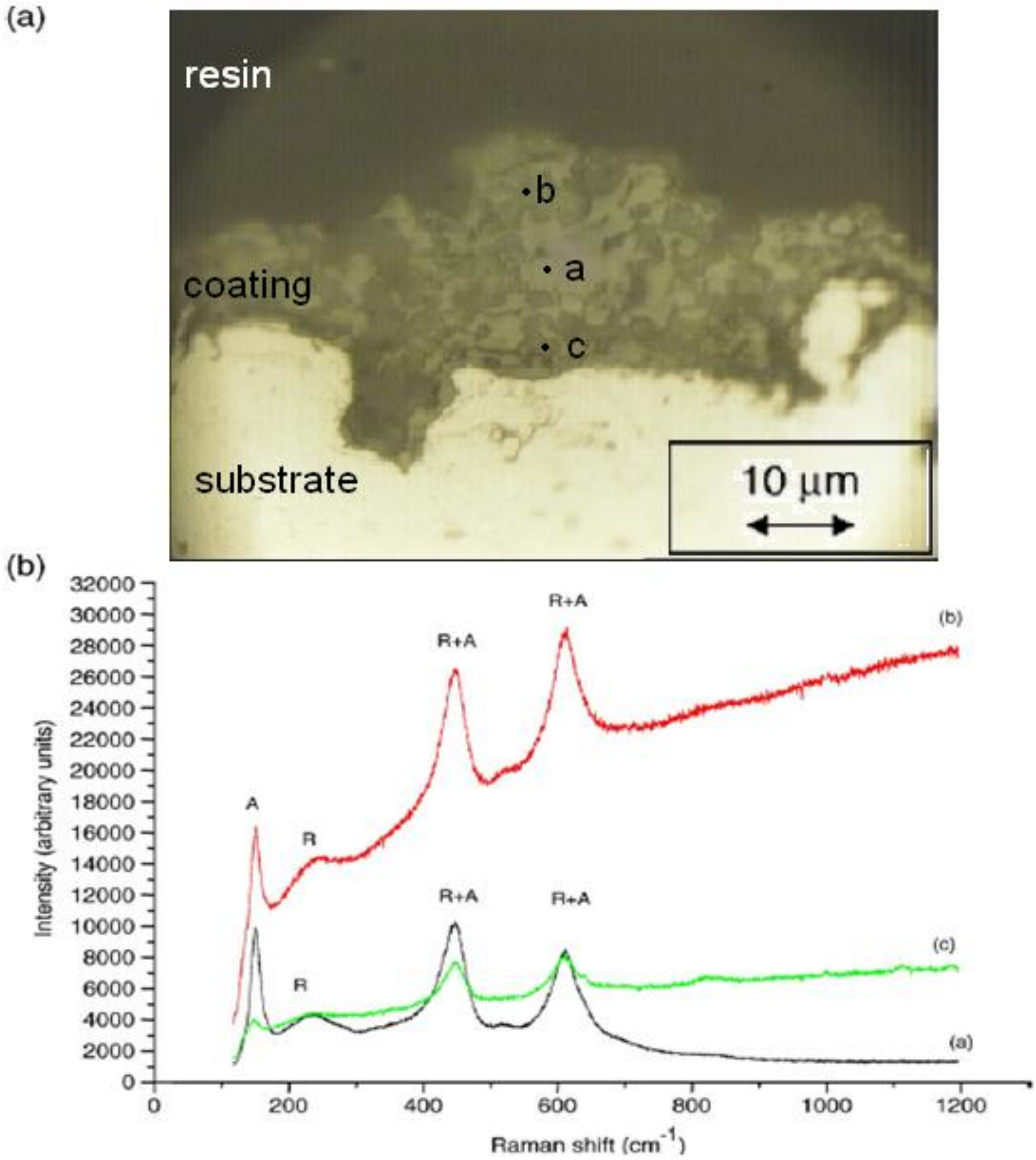

Figure 3.41 *Metallographic cross-section of the sample T1 with marked tested points on the coating (a) and Raman spectra in the marked points (b)* ***[105].***

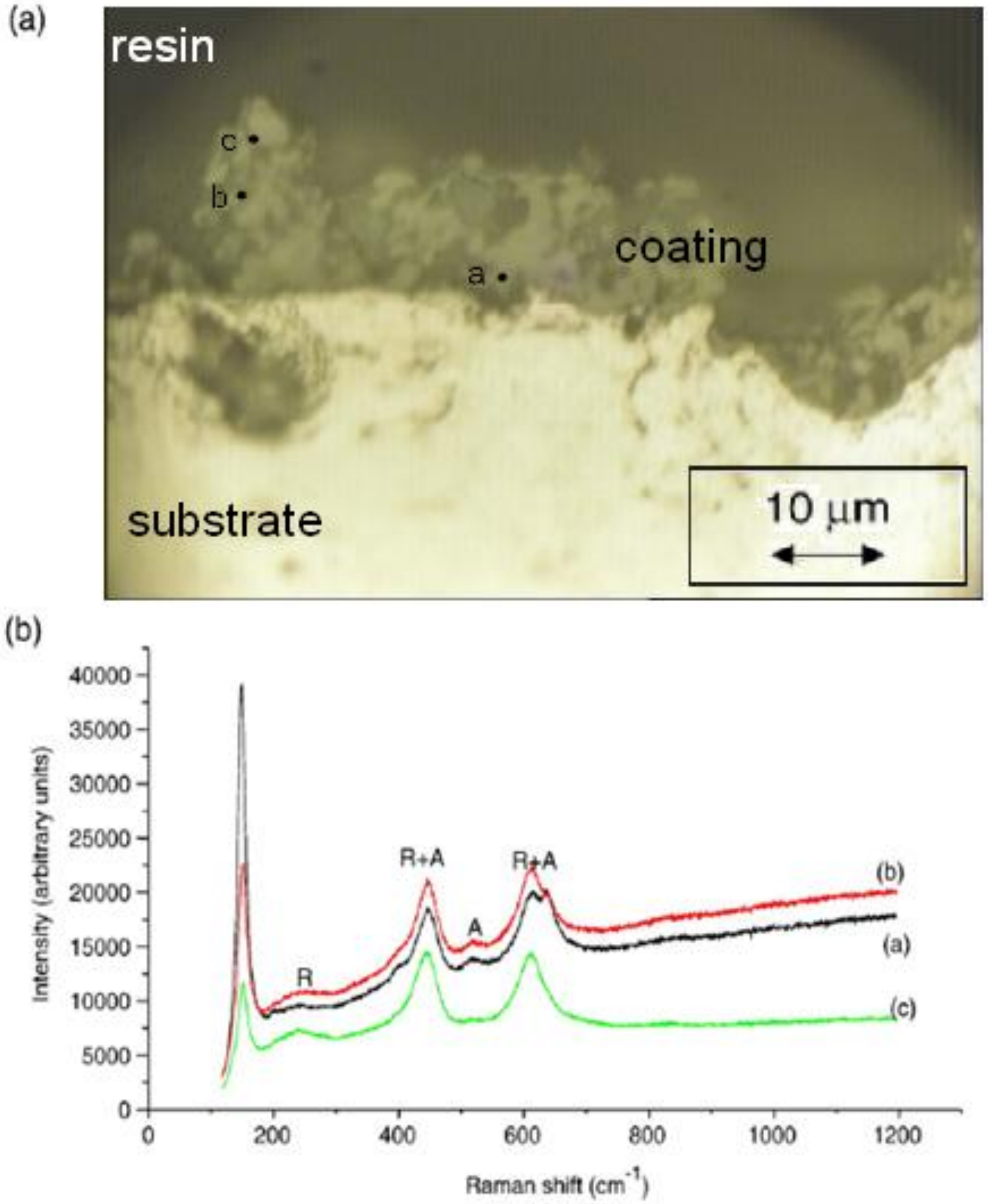

Figure 3.42** Metallographic cross-section of the sample T7 with marked tested points on the coating (a) and Raman spectra in the marked points (b)* ***[105].

The presence of rutile and anatase phase in the samples based on water suspension was confirmed. The quantity of anatase was varying locally inside the coating and was different for various tested samples. Typical sample with low anatase content - T1 (presented above) has the peaks of rutile and anatase superimposed in the regions at 400-440 cm^{-1} and 600-640 cm^{-1} (R+A peaks are present in majority of tested samples). In the sample containing more anatase those R+A peaks are split (see Figure3.42 b point a). The anatase rich zones are present rather at the interface of coating and substrate (similar phenomenon was observed for sample T4).

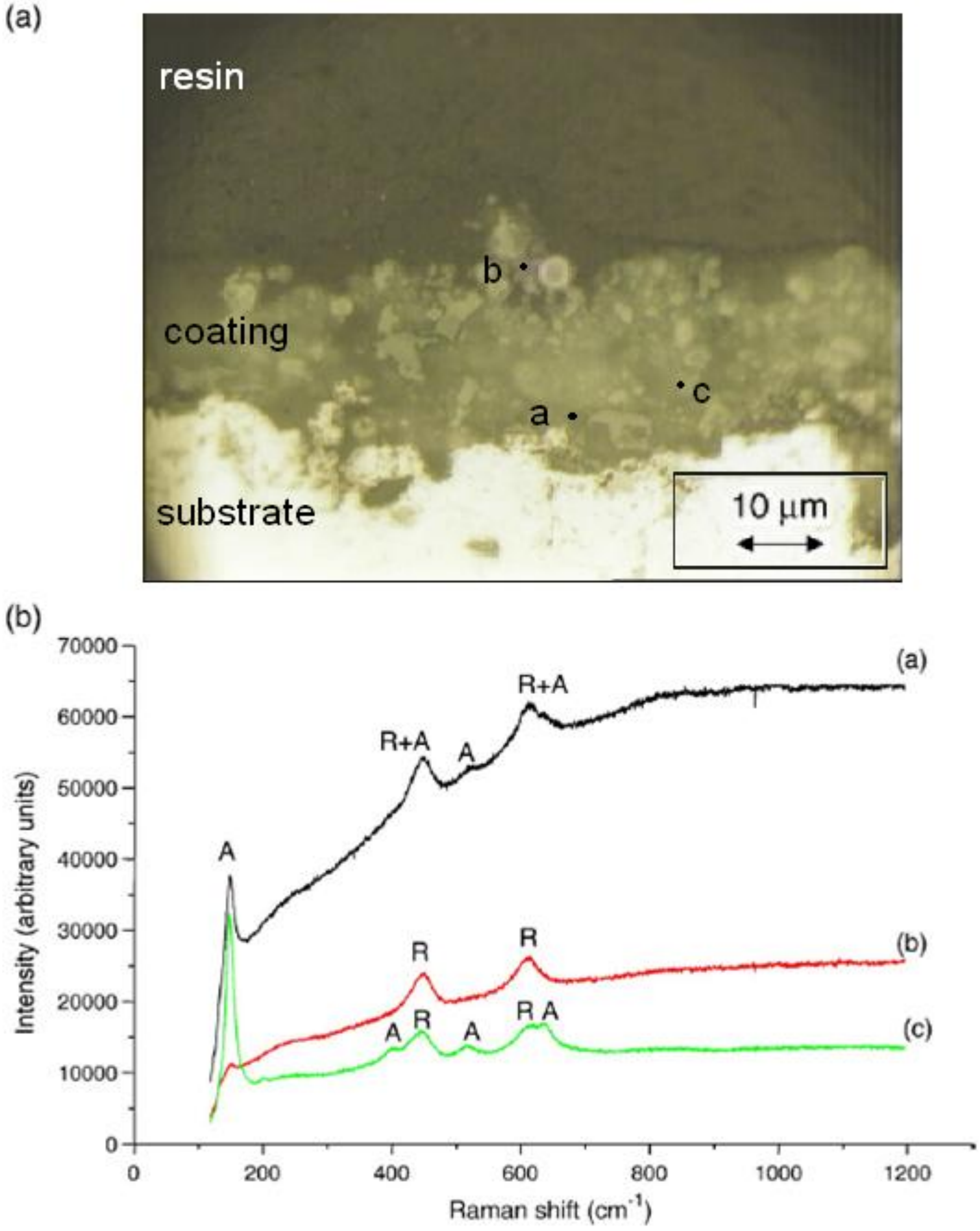

Figure 3.43 *Metallographic cross-section of the sample T02 with marked tested points on the coating (a) and Raman spectra in the marked points (b)* ***[105].***

More porous microstructure could be seen using microscopic observations for the samples made by SPS of alcoholic suspension. In some of the observed sites, the Raman spectra are similar to that of water based suspensions. However there are some sites (Figure3.43b. point c) having anatase peaks (at 399 cm^{-1} and 640 cm^{-1}) clearly separated from the rutile ones (430 cm^{-1} and 612 cm^{-1}). The results for the samples sprayed using only ethanol (T03 an T04) were similar to the results of T02 sample (points a and c). It confirms that for the samples sprayed with alcohol, the quantity of anatase at analyzed sites is greater.

This fact was also confirmed by XRD analysis of anatase content in samples T01 and T02. The results show that the fraction of anatase is about twice greater than in the samples made by water based suspension. The results of anatase content calculations are presented in Table 3.27 which is complementary to Table 3.20.

Table 3.27 Content of anatase in samples T01 and T02.

Experiment No.	Fraction of anatase [wt%]
T01	19.6
T02	22.4

SEM and TEM analyses were also used for microstructure study of TiO_2 coatings. Figure 3.44 presents SEM micrograph of the cross section of sample T11 used for TEM investigations (left), and TEM micrograph of the region adjacent to surface (coating with varying transparency due to ion thinning)(right). Two regions were chosen (marked with A and B rectangles) for detailed investigation.

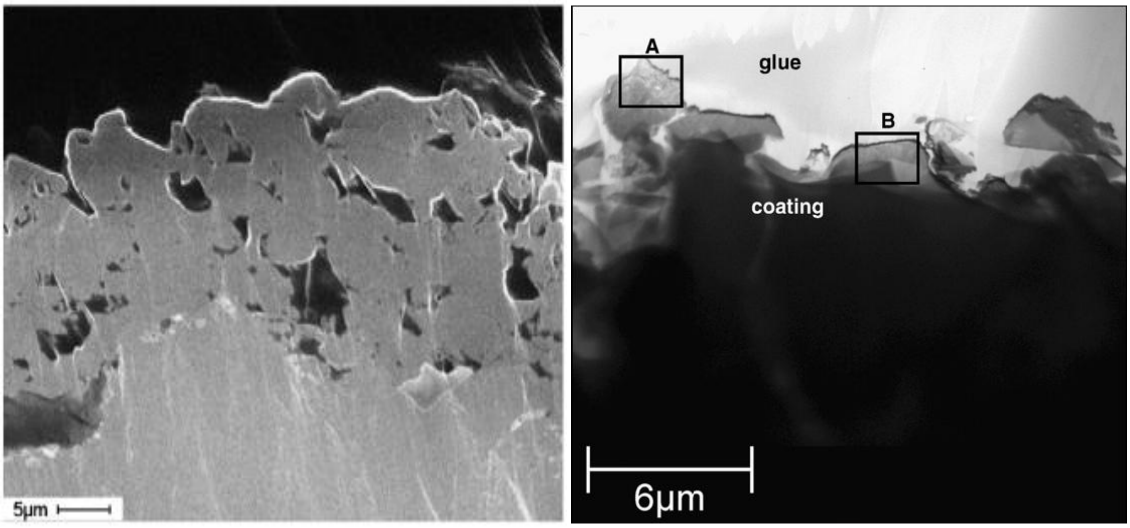

Figure 3.44 *SEM (secondary electrons) micrograph of the cross-section of T11 sample (left);TEM micrograph of the region adjacent to surface (coating with varying transparency) (right) of the same sample* ***[105].***

The observations made by electron microscopy confirm that the coatings are porous and their surfaces are rough. TEM micrograph shows thinned region with varying specimen thickness. Marked regions were magnified and shown in Figure 3.45.

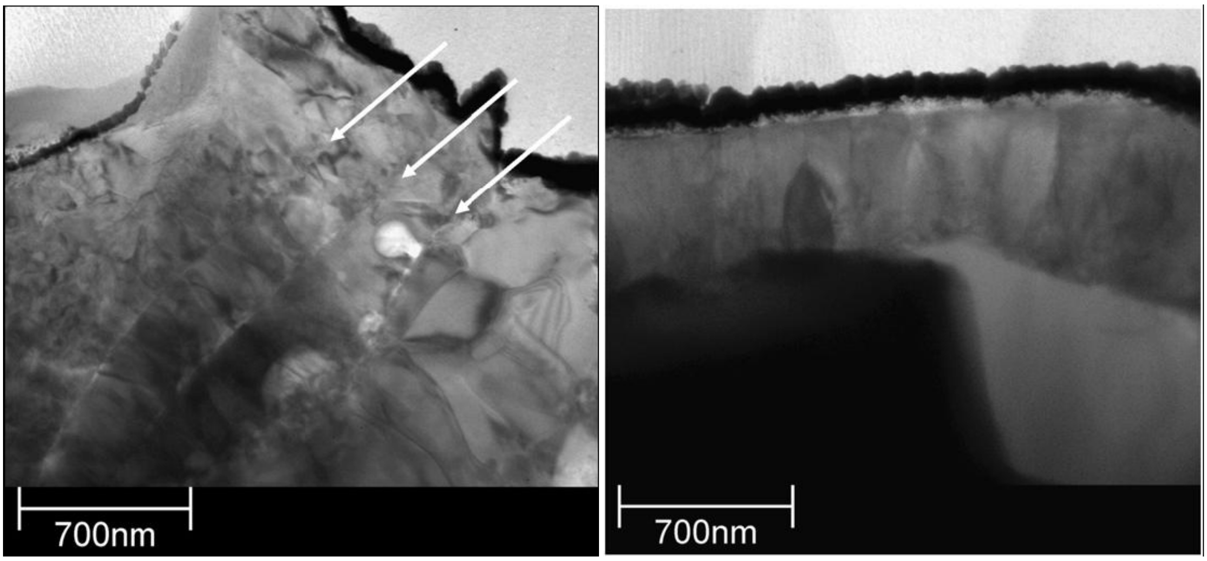

Figure 3.45 *TEM micrographs of the area A (left) and B (right) from previous figure. The arrows indicate boundaries between lamellae* ***[105].***

The results shown in Figure. 3.45 are typical for stacking structure of small submicrometer lamellae (area A), and columnar structure of crystal grain inside lamellae (area B); thin dark layer at the top of the sample corresponds to evaporated gold layer.

SUMMARY OF THE TiO_2 COATINGS INVESTIGATION

The coatings of titania were sprayed using commercially available powder in form of rutile. Only atomizer was used as injector during the spraying of the samples. The samples were very porous and their thicknesses ranged from few to tens of micrometers. The statistical analysis let one to state that anatase content is correlated with spraying distance. An increase in anatase content was caused by increase of spraying distance. The reason of this phenomenon was probably solidification of the particles before impact on the substrate.

The thickness of the coating was dependent on the electric power input to the plasma. The increase of the power caused some decrease of the coating thickness due to increase of the velocity and turbulence of the plasma jet.

The analysis by scratch test showed that spraying distance was again the parameter which influenced at the highest degree the value of the critical load. Another measured value i.e. scratch hardness was higher for anatase samples due to stronger cohesion strength.

Finally the content of anatase and rutile was independent on the position of measurement point in the micro-Raman analysis, but in the majority of samples the highest content of anatase was found close to the coating surface.

4 DISCUSSION

4.1 HYDROXYAPATITE POWDER SYNTHESIS

As it was mentioned in the chapter 3 the HA powder was synthesized by precipitation. The precursor solutions were: diammonium phosphate and calcium nitrate. The synthesis was optimized by design of experiments using composite matrix. Two variables were chosen i.e. the concentration of [Ca] solution and volume of ammonia. As responses, purity of obtained powder and its mass were considered. It was found that molar concentrations influence strongly the HA purity. The optimal calculated value was equal to 1.26 mol/l of calcium nitrate and consequently 0.76 mol/l of diammonium phosphate. Optimal value of the ammonium hydroxide volume present during synthesis was equal to 41ml. The other parameters had also an important influence on the final HA purity, e.g. temperature should be kept constant at the level of 80^0C, in comparison with 60^0C used by Bouyer et al.[106]. Those conditions enabled us to obtain the purest HA powder. The undesirable change of the parameters resulted in appearance of impurity in form of α-TCP and β-TCP. The calcination process causes some increases in the powder grain sizes, but the calcination is necessary to obtain the crystal in form of powder. After calcination the increase in grain sizes makes it necessary to realize attrition milling in order to obtain submicrometer sized powder which was used as initial feedstock for suspension plasma spraying.

4.2 OPTIMIZATION OF SUSPENSION COMPOSITION AND SUSPENSION INJECTING SYSTEM

Different solvents for the suspension preparation were considered, namely:

- Water (H_2O) (causes the most significant cooling of the plasma)
- Ethanol (C_2H_5OH) (causes a rise of plasma jet temperature, what may lead to partial melting of the substrate surface)
- Mixture water and ethanol (50:50) (seems to be a kind of compromise between the properties of solvents specified above – it was found that the most repeatable experiments results were obtained using that mixture)

As it was mentioned before, the results obtained during optimization of injection system enable one to state that the most significant parameter of suspension injecting is the suspension feed rate. Changing of the feed rate results in the change in the plasma properties – especially important change of plasma temperature. The parameter directly connected with feed rate of suspension is electric arc power input which should be adjusted to prevent excessive cooling of the plasma jet by the stream of the injected suspension.

Both the external suspension injecting methods - atomizing and continuous stream have some advantages and drawbacks.

The atomizer cools down plasma jet. Furthermore – it influences the droplets sizes in the suspension. Consequently a lot of the droplets may stay in the plasma periphery and be transported towards the substrate without total evaporation of the solvent. Consequently the, melting of the powder particles during theirs flight is impossible. Moreover, the plasma jet, due to the short spraying distance, may cause increase in temperature of the substrate.

In the system with external continuous stream nozzle, the stream of suspension droplets is generated by the secondary break-up (fragmentation). The solvent evaporates. The pressure of the suspension stream must be precisely set up so as to cause the break-up of particles. The produced small particles would be able to melt and form a coating.

Internal injection (with continuous stream nozzle) was the most promising method of suspension injection. In this system the suspension feed rate influences considerably plasma temperature and must be also precisely adjusted. But in this case, the value of injection pressure may be changed in a wide range and it is not a critical parameter as in the case of the external injection method. However, there is maximum value of feed rate exists. Above this feed rate value the drops of suspension would flow down along the torch nozzle walls (anode).

4.3 HYDROXYAPATITE COATINGS INVESTIGATION

As it was mentioned in chapter 3 the preliminary studies of HA coatings obtained by SPS with atomizer injection were carried out. The results indicate that the injection system has great influence on the coating properties. The ideal injection case, atomizer should produce droplets with homogeneous size distribution, what would result in their similar thermal history after injection into plasma jet. The real coatings were very porous and characterized by very poor cohesion. That was caused, probably, by injecting of some amount of suspension into the jet periphery, what caused that the solvent was not fully evaporated and some particles of powder were sintered onto the substrate by the next torch pass over deposited coating. The second case of particles history in the jet was connected with less intensive cooling after deposition on the substrate what resulted in the formation of decomposition phases. The XRD revealed that the phase decomposition of HA occured, and that, αTCP and βTCP phases were presented in the coatings. βTCP could have been formed from αTCP and CaO from TTCP during cooling down of the particles. In this case the spraying parameters were defferent from the optimal parameters values.

The corrosion test in the BSF was done for the period ranging from 3 to 60 days. The investigations results show that hydroxyapatite coatings composition vary in function of immersion time in the BSF. XRD results show that some phases are dissolved in the Kokubo solution. This is clearly seen on the all plots showing phase content vs. immersion time. Percentage of the decomposed phases decreased. The case of CaO shows the reduction of content after 3 days of immersion from 1.5 to about 0.5 %. Li et al.[107] showed the way of HA coating dissolution in the following sequence:

$$\text{HA}<\text{CDHA}<\text{OHA}<\beta\text{-TCP}<\alpha\text{-TCP}<\text{TTCP}<\text{ACP}$$

The micro-Raman spectroscopy confirms the fact that after immersion in the BSF the HA coatings content less TCP phases what can be seen due to the absence of the peaks in the range 390 – 650 cm^{-1} and in the range from 1020 cm^{-1} to 1080 cm^{-1}.

The measurements carried out by impedance spectroscopy made it possible to fit the response of the signal in the wide range of frequencies to the electrical equivalent circuit. The n-factors in the CPE_1 and CPE_{TC2} correspond to the amount of amorphous phase in the HA coating. The value close to 0.8 is typical for amorphous materials [99]. The samples fabricated with higher torch power contained less crystalline phase in HA layer and more of the amorphous phase. HA layers were highly defective as the activation energies of dielectric relaxation in all samples were much lower than 2eV, reported as activation energy of conductivity in bulk crystalline HA [108].

The second series of measurements was done after immersing the sample in deionized water and drying it with a heater. The results give some information about porosity of the coatings, which is determined by drying time of the sample. On the beginning, the results of measurements of wet samples showed strong capacitance dispersion. It must have been caused by the dielectric polarization in water [109]. As the sample dried out the dispersion shifted to lower frequencies and disappeared. At high frequencies the changes in capacitance were related mainly to the changes of effective electric permittivity of HA-H_2O composition. The changes resulted from large difference of electric permittivities of water (ε_{H2O}=67 at 60°C [110]) and dry hydroxyapatite (ε_{HA}=18 [108]).

The initial K_{CP} values of the investigated samples were comparable, however their drying times were different. The drying time was determined as the moment when (K_{CP}-1) dropped to 10% of its original value. The samples which were sprayed at a shorter distance (sample No. 200 and 300), as shown before, contained more crystalline phase in HA coating and had longer drying times, what suggests that these samples had more complex structure with smaller pores.

4.4 TITANIUM OXIDE COATINGS INVESTIGATIONS

All titania coatings were sprayed using commercially accessible powder.

According to the description in section 3.5 titanium oxide coating suspension sprayed using atomizer were examined. In this case plasma jet was intensively cooled by suspension solvent as well by atomizing gas. Ten samples were sprayed at different process parameters. The samples had very porous microstructure and their thicknesses varied from few to tens of micrometers. The obtained results were treated by Nemrod software for statistical analysis, in order to observe the influence of the spraying parameters on the coating microstructure. The regression equation calculated by Nemrod software indicates that the fraction of anatase is strongly correlated with only one process parameter i.e. spraying distance. In such way that – an increase in the spraying distance causes the increase of the anatase content in the coating. This was probably caused by solidification of the particles before impact on the substrate.

The analysis shows also that the thickness of the coating depends mainly on power input into plasma. The increase of electric power results in a decrease of the coating thickness. It results from an increase in the velocity and turbulence of the plasma jet with increasing power. Then, the suspension droplets need more kinetic energy to get into plasma jet. Additionally, some particles which are not closely adhering to the substrate are blown away. The last analysis revealed that the anatase crystal sizes are not dependent on the spraying parameters.

The same samples were investigated by the scratch test. Statistical analysis of the test results shows that the spraying distance has again the most significant influence on the critical load. The decrease of the spray distance results in the formation of well molten particles. This promotes better adhesion and cohesion of the coatings. Scratch hardness value was much higher for anatase coating than for the rutile ones. This is due to a stronger cohesion strength of anatase. The coatings made from rutile suspension were very porous and rough.

Analysis by micro-Raman spectroscopy showed that the measured content of anatase and rutile is not strongly correlated with the position of measurement point at the sample cross-section (however majority of samples showed the anatase rich zones close to the coating surface).

5 CONCLUSIONS

The investigations realized in the thesis let one to obtain the finely structured coatings.

Two types of suspension delivery systems were adopted for suspension plasma spraying, namely pressurized vessel system and electronically controlled feeder with the peristaltic pumps. It was found that the latter can be used just in the configuration with atomizer - while in the case of continuous stream nozzle the outlet pressure of suspension was insufficient to penetrate the plasma jet by suspension stream.

The investigations aiming at an optimization of the injecting system have shown that more efficient was the system using continuous stream nozzle and the best solution was an internally mounted injector (with diameter 0.5 mm), which injected 100% of suspension into plasma jet. The coatings of about 100μm thickness, were obtained by two times less numer of torch passages in comparison with an atomizer.

Essentially, three variables were significantly influenced resulting coatings at SPS experiments i.e. spraying distance, torch power and kind of suspension solvents. It was found that the water used for the formulation of suspension consumed the highest amount of energy, whereas pure ethanol burnt during spraying and in consequence increased the temperature of the plasma jet, which in special case melted the substrate. The compromise, mixture of water and ethanol (50:50) appeared as the best solution.

Larger quantity of hydroxyapatite powder was obtained in a single synthesis and in a short time using:

a) multiplying of the initial solutions concentrations (2,4 and 8 times; the amount of ammonia was the same for all trials) – increasing of the concentrations resulted in proportional mass increases of obtained powder, however, too high concentration (increased by 8 times) caused significant deterioration of powder purity (to 65 % HA)

b) reduction of reaction time from 3h to 15 minutes (without the rest time) – did not influence the purity of synthesized powder

c) multiplication of the ammonia volume by the same factor as initial solutions concentrations did not influence the purity of the obtained powder

d) increasing the volume of reagents and reactor (scale effect) did not influence the purity of the obtained powder

After application of the means listed above in the optimal conditions ([Ca] concentration – 2mol/l, [P] concentration – 1.2 mol/l, V_{amon} = 40 ml, time of reaction 15 minutes, volume of glass bulb – 1l) it was possible to obtain 600-700 grams of the HA powder with high quality (with the mean purity 99% HA)

The statistical treatment enabled us to calculate the isopleths of two process variables i.e. concentration of calcium nitrate solution and volume of ammonium hydroxide. It was shown that the concentration of the $[Ca^{2+}]$ above 2 mol/l does not allow one to obtain pure HA powder. Also statistical treatment by Nemrod software made it possible to calculate the optimal concentration of the [Ca] solution (1.26 mol/l), optimal concentration of [P] solution (0.76 mol/l) and optimal volume of ammonia (41ml).

The corrosion test let one to see that during immersion of HA samples in the body simulated fluid, the content of decomposition phases such as (α-TCP, β-TCP, TTCP and CaO) decreased, what would be useful in the applications as implant coatings in medical prosthetics.

Impedance spectroscopy investigations of the HA samples without immersion in BSF revealed that the samples No. 200 and No. 300 had longer drying times what suggests that the samples have smaller pores or more complex structure, corresponding to the samples sprayed at the smaller spray distance of 50mm.

The investigations of titania coatings properties and their statistical analysis using Nemrod software have shown that spraying distance was influenced the anatase content and critical load in the scratch tester, whereas the electric arc power was influencing the coating thickness. This analysis pointed out also that the anatase crystal sizes and scratch hardness are independent on the analyzed spraying parameters.

The analysis of the X-ray and micro-Raman spectroscopy results revealed that the titania coating sprayed using alcoholic suspension promotes more porous microstructure (confirmed also by SEM and TEM observations) with higher quantity of anatase.

The further works should be focused on:

- calculations of the heat amount transfer to the substrate during spraying
- investigations of the coating contamination by the products of ethanol burning
- repeating the investigation of the spraying parameters influence on HA content in coatings using higher number of experiments

Conclusions and discussions presented in the text of the thesis and briefly in this chapter above let one to claim, that the confirmation of the thesis formulated within the investigations was succeeded . The thesis has the following form:

It is possible to optimize the successive stages of the hydroxyapatite and titania coatings production so as to obtain submicrometric structures with desirable phase composition and physicochemical properties.

The optimization concerned the following problems:

- selection of the plasma spraying method,
- selection and preparation of the suspension components (powder, solvent and eventually dispersant),
- selection of the suspension feeding and injection system,
- selection of the spraying process parameters.

In this thesis there were realized the particular aims which includes among others:

- determination of the spraying process parameters, the most important for achieving desirable coating properties,
- selection of the parameters values, using the observation of their influence on the coating properties verified by analytical methods.

6 REFERENCES

[1] Pawlowski L. *The science and engineering of thermal spray coatings*, 2 ed., Wiley, Chichester, England

[2] Morel S. *Powłoki natryskiwane cieplnie,* Wydawnictwo Politechniki Częstochowskiej 1997

[3] Fauchais P., Montavon G., Vardelle M., Cedelle J. *Recent development in direct current plasma spraying,* conference proceedings 2RIPT, Lille 2005, pp. 1 - 34

[4] Bansal P., Shipway P.H., Leen S.B. *Effect of particle impact on residual stress development in HVOF sprayed coatings*, Journal of Thermal Spray Technology, Vol. 15, No. 4 / December 2006, pp. 570-575

[5] Guilemany J.M., Nin J. *HVOF Forming: A new&promising tool*, conference materials 2RIPT, Lille 2005, pp. 196-208

[6] Ma X.Q., Roth J., Gandy D.W., Frederick G.J. *A new high-velocity oxygen fuel process for making finely structured and highly bonded inconel alloy layers from liquid feedstock*, Journal of Thermal Spray Technology, Vol. 15, No. 4 / December 2006, pp 670 - 675

[7] Lima R.S., Li H., Khor K.A., Marple B.R. *Biocompatible nanostructured high-velocity oxyfuel sprayed titania coating: Deposition, characterization, and mechanical properties,* Journal of Thermal Spray Technology, Vol. 15, No. 4 / December 2006, pp. 623 - 627

[8] Bolot R., Sokolov D., Klein D., Coddet C. *Nozzle developments for thermal spray at very low pressure*, Journal of Thermal Spray Technology, Vol. 15, No. 4 / December 2006, pp. 827 - 833

[9] Fan S., Yang G., Li C., Liu G., Li C., Zhang L. *Characterization of microstructure of nano-TiO2 coating deposited by vacuum cold spraying*, Journal of Thermal Spray Technology, Vol. 15, no. 4 / December 2006, pp. 513-517

[10] Giannini G. Ducati A. *Plasma stream apparatus and methods*, US Patent, no 2922869

[11] Gage R., Nestor O., Yenni D. *Collimated electric arc powder deposition process,* US Patent, No. 3016447

[12] Gerdien H. and Lotz A. *Wissen. Veröffen. Siemens Werken*, 1922, **2**, pp. 489–496

[13] Lee Yi-Pang, Wang Chih-Kuang, Huang Tsui-Hsien, Chena Chun-Cheng, Kaoa Chia-Tze, Ding Shinn-Jyh. *In vitro characterization of postheat-treated plasma-sprayed hydroxyapatite coatings*, Surface and Coatings Technology Vol. 197, 2005, pp. 367– 374

[14] Li H., Khor K.A., Cheang P. *Effect of steam treatment during plasma spraying on the microstructure of hydroxyapatite splats and coatings*, Journal of Thermal Spray Technology, Vol. 15, No. 4 / December 2006, pp. 610 - 616

[15] Ernst P., Barbezat G. *Thermal spray applications in powertrain contribute to the saving of energy and material resources*, Surface and Coatings Technology, Vol. 202, 2008, pp. 4428-4431

[16] Soltani R., Garcia E., Coyle T.W., Mostaghimi J., Lima R.S., Marple B.R., Moreau C. *Thermomechanical behavior of nanostructured plasma sprayed zirconia coatings,* Journal of Thermal Spray Technology, Vol. 15, No. 4 / December 2006, pp/ 657 - 662

[17] Rico A., Rodriguez J., Otero E., Zeng P., Rainforth W. *Wear behavior of nanostructured alumina-titania coatings deposited by atmospheric plasma spray,* Wear, Vol 267, 2009, pp. 1191-1197

[18] Klimpel A. *Napawanie i natryskiwanie cieplne*. Wydawnictwa Naukowo-Techniczne 2000

[19] Trelles J.P., Heberlein J.V.R. *Simulation results of arc behavior in different plasma spray torches*, Journal of Thermal Spray Technology, Vol. 15, No. 4 / December 2006, pp. 563 - 569

[20] Dyshlovenko S., Pawlowski L., Pateyron B., Smurov I., Harding J.H. *Modelling of plasma particle interactions and coating growth for plasma spraying of hydroxyapatite,* Surface and Coatings Technology, Vol. 200, 2006, pp. 3757 – 3769

[21] Fauchais P., Rat V., Coudert J.-F., Etchart-Salas R., Montavon G. *Operating parameters for suspension and solution plasma-spray coatings,* Surface and Coatings Technology, Vol. 202, 2008, pp. 4309–4317

[22] Ravi B.G., Gandhi A., Guo X.Z., Margolies J. and Sampath S. *Liquid Precursor Plasma Spraying of Functional Materials: A Case Study for Yttrium Aluminum Garnet (YAG),* Journal of Thermal Spray Technology, Vol. 17, No. 1 / March, 2008, pp. 82 - 90

[23] Ravi B.G., Sampath S., Gambino R., Devi P., Parise J. *Plasma spray synthesis from precursors: Progress, issues, and considerations,* Journal of Thermal Spray Technology, Vol. 15, no. 4 / December 2006, pp. 701-707

[24] Gell M., Jordan E., Teicholz M., Cetegen B., Padture N, Xie L., Chen D, Ma X. and Roth J. *Thermal Barrier Coatings Made by the Solution Precursor Plasma Spray Process,* Journal of Thermal Spray Technology, Vol. 17, No. 1 / March, 2008, pp. 124-135

[25] Jordan E.H., Xie L., Ma X., Gell M., Padture N.P., Cetegen B., Ozturk A., Roth J., Xiao T.D., Bryant P.E.C. *Superior Thermal Barrier Coatings Using Solution Precursor Plasma Spraying,* Journal of Thermal Spray Technology, Vol. 13, no. 1 / March 2004, pp. 57 - 65

[26] Basu S., Jordan E., Cetegen B. *Fluid Mechanics and Heat Transfer of Liquid Precursor Droplets Injected into High-Temperature Plasmas,* Journal of Thermal Spray Technology, Vol. 17, No. 1 / March, 2008, pp. 60 – 72

[27] Borisov Y., Bushma A., Krivtsun I. *Modeling of motion and heating of powder particles in laser, plasma, and hybrid spraying,* Journal of Thermal Spray Technology, Vol. 15, no. 4 / December 2006, pp. 553 – 558

[28] Fukumoto M., Nagai H., Yasui T. *Influence of surface character change of substrate due to heating on flattening behavior of thermal sprayed particles,* Journal of Thermal Spray Technology, Vol. 15, No. 4 / December 2006, pp. 759 – 764

[29] Ivosevic M., Gupta V., Baldoni J.A., Cairncross R.A., Twardowski T.E., Knight, R. *Effect of substrate roughness on splatting behavior of HVOF sprayed polymer particles: Modeling and experiments*, Journal of Thermal Spray Technology, Vol. 15, No. 4 / December 2006, pp 725 - 730

[30] Raessi M., Mostaghimi J., Bussmann M. *Effect of surface roughness on splat shapes in the plasma spray coating process,* Thin Solid Films, Vol. 506– 507, 2006, pp. 133-135

[31] Pasandideh-Fard M., Pershin V., Chandra S., Mostaghimi J. *Splat Shapes in a Thermal Spray Coating Process: Simulations and Experiments,* Journal of Thermal Spray Technology, Vol. 11, No. 2 / June 2002, pp. 206 - 217

[32] Cedelle J. PhD Thesis, *Study of the formation of lamellae resulting from the impact of millimeter and micrometer sized droplets: application of coating manufacturing by plasma spraying,* Limoges 2005

[33] Fauchais P., Etchart-Salas R., Rat V., Coudert J.F., Caron N. and Wittmann -Ténèze K. *Parameters Controlling Liquid Plasma Spraying: Solutions, Sols, or Suspensions*, Journal of Thermal Spray Technology, Vol. 17, No. 1 / March, 2008, pp. 31 - 59

[34] Li C., Li C., Yang G., Wang Y. *Examination of substrate surface melting-induced splashing during splat formation in plasma spraying*, Journal of Thermal Spray Technology, Vol. 15, No. 4 / December 2006, pp. 717 – 724

[35] Xue M., Chandra S., Mostaghimi J. *Investigation of splat curling up in thermal spray coatings*, Journal of Thermal Spray Technology, Vol. 15, No. 4 / December 2006, pp. 531 - 536

[36] Marchand C., Maitre A., Grimaud A., De Noirjean A., Lefort P. *Nitridation of Ti_6Al_4V powder in thermal plasma conditions and sintering of obtained TiN powder,* conference proceedings 2RIPT, Lille 2005

[37] Dyshlovenko S., Pateyron B., Pawlowski L., Murano D. *Corrigendum to Numerical simulation of hydroxyapatite powder behaviour in plasma jet. [Surf. Coat. TechNol. 179 (2004) 110–117]* Surface and Coatings Technology, Vol. 187, 2004, pp. 408– 409

[38] Dyshlovenko S., Pateyron B., Pawlowski L., Murano D. *Numerical simulation of hydroxyapatite powder behaviour in plasma jet,* Surface and Coatings Technology, Vol. 179, 2004, pp. 110–117

[39] Heimann R. B., *Thermal spraying of biomaterials,* Surface and Coatings Technology, Vol. 201, 2006, pp. 2012-2019

[40] Heimann R. B., *Is it feasible to develop plasma-sprayed tandem coating with bio-capacitor properties?*, 3rd Workshop “Keramische Biomaterialien”, 20.-21.Oktober 2005, University of Bochum, Germany

[41] Tomaszek R., Pawlowski L., Zdanowski J., Grimblot J., Laureyns J. *Microstructural transformations of TiO2, Al2O3+13TiO2 and Al2O3+40TiO2 at plasma spraying and laser engraving,* Surface and Coatings Technology, Vol. 185, 2004, pp. 137– 149

[42] Hornez J., Chai F., Blanchemain N., Lefevre A., Descamps M., Hildebrand H. *Biocompatibility Improvement of Pure Hydroxyapatite (Ha) with Different Porosity,* Key Engineering Materials Vol.s. 330-332, 2007, pp. 927-930

[43] Wierzchoń T., Czarnowska E., Krupa D., *Inżynieria powierzchni w wytwarzaniu biomateriałów tytanowych.* Oficyna Wydawnicza Politechniki Warszawskiej 2004

[44] Dyshlovenko S., Pawlowski L., Roussel P., Murano D., Le Maguer A. *Relationship between plasma spray operational parameters and microstructure of hydroxyapatite coatings and powder particles sprayed into water,* Surface and Coatings Technology, Vol. 200, 2006, pp. 3845– 3855

[45] Dyshlovenko S., Pawlowski L., Smurov I., Veiko V. *Pulsed laser modification of plasma-sprayed coatings: Experimental processing of hydroxyapatite and numerical simulation,* Surface and Coatings Technology, Vol. 201, 2006, pp. 2248–2255

[46] Pierlot Ch., Pawlowski L., Tomaszek R., Dyshlovenko S., Bigan M. *Interdependence of different properties of hydroxyapatite coatings and powders plasma sprayed into water,* Chemometrics and Intelligent Laboratory Systems Vol. 86, 2007, pp. 153–158

[47] Mroz W., Jedynski M., Paszkiewicz Z., Prokopiuk A., Slosarczyk A. *Characterization of hydroxyapatite and Mg-doped hydroxyapatite coatings deposited by pulsed laser ablation technique using: ARF excimer laser,* Engineering of Biomaterials, Vols. 69-72, 2007, pp 15-17

[48] Mroz W., Jedynski M., Prokopiuk A., Burdynska S., Wierzchon T. *Influence of substrate temperature on hydroxyapatite coatings deposited by pulsed laser ablation method,* Engineering of Biomaterials, Vols. 69-72, 2007, pp. 8-11

[49] **Jaworski R**., Pierlot C., Tomaszek R., Pawlowski L., Znamirowski Z., Zdanowski J. *Optimization of Dielectric Properties of Suspension Plasma Sprayed Hydroxyapatite Coatings,* Mat.-wiss. u. Werkstofftech., Vol. 38, No. 2 / 2007

[50] **Jaworski R.** MA thesis, Wrocław 2006

[51] Pyda W., Slosarczyk A., Paszkiewicz Z., Rapacz-Kmita A., Haberko M., Pyda A. *Polycrystalline hydroxyapatite materials reinforced with zirconia inclusions*, Composites 1(2001)2

[52] **Jaworski R**., Le Maguer A., Laureyns J., Tomaszek R., Pawlowski L. *Raman microscopic studies on phases distribution in suspension plasma sprayed TiO2 and films and coatings,* International conference JSPTS Tours, 2007
[53] Tomaszek R., Pawlowski L., Gengembre L., Laureyns J., Znamirowski Z., Zdanowski J. *Microstructural characterization of plasma sprayed TiO2 functional coating with gradient of crystal grain size,* Surface and Coatings Technology, Vol. 201, 2006, pp. 45–56
[54] Larouche S., Szymanowski H., Klemberg-Sapieha J., Martinu L. *Microstructure of plasma-deposited* SiO_2/TiO_2 *optical films,* Journal of Vac. Sci. Technology, Vol 22, No 4, 2004, pp. 1200 - 1207
[55] www.azom.com
[56] Tomaszek R. PhD Thesis, *Suspension plasma spraying of functional gradient coatings,* Lille and Wrocław 2006
[57] Tomaszek R., Pawlowski L., Gengembre L., Laureyns J., Le Maguer A. *Microstructure of suspension plasma sprayed multilayer coatings of hydroxyapatite and titanium oxide,* Surface and Coatings Technology, Vol. 201, 2007, pp. 7432–7440
[58] Tomaszek R., Znamirowski Z., Pawlowski L., Wojnakowski A. *Temperature behaviour of titania field emitters realized by suspension plasma spraying,* Surface and Coatings Technology, Vol. 201, 2006, pp. 2099–2102
[59] Znamirowski Z., Czarczynski W., Le Maguer A., Pawlowski L. *Plasma sprayed and laser engraved field electron emitters,* Surface and Coatings Technology, Vol. 165, 2003, pp. 211-215
[60] Czarczyński W., Znamirowski Z. *Field electron emission experiments with plasma sprayed layers*, Surface and Coatings Technology, Vol. 202, 2008, pp. 4422-4427
[61] Znamirowski Z., Ladaczek M. *Lighting segment with field electron titania cathode made using suspension plasma spraying,* Surface and Coatings Technology, Vol. 202, 2008, pp. 4449-4452
[62] Berghaus J., Legoux J.G., Moreau C., Tarasi F. and Chráska T. *Mechanical and Thermal Transport Properties of Suspension Thermal-Sprayed Alumina-Zirconia Composite Coatings* Journal of Thermal Spray Technology,Vol. 17, No. 1 / March, 2008, pp 91-104
[63] **Jaworski R**., Le Maguer A., Laureyns J., Tomaszek R., Pawlowski L. *Raman microscopic studies on phases distribution in suspension plasma sprayed TiO2 and films and coatings,* International conference JSPTS Tours, 2007
[64] Kang Man Gu, Park Nam-Gyu, Park Yong Joon, Ryu Kwang Sun, Chang Soon Ho. *Manufacturing method for transparent electric windows using dye-sensitized TiO2 solar cells,* Solar Energy Materials and Solar Cells, Vol. 75, 2003, pp. 475–479
[65] Toma F., Bertrand G., Klein D., Coddet C., Meunier C. *Nanostructured photocatalytic titania coatings formed by suspension plasma spraying*, Journal of Thermal Spray Technology, Vol. 15, No. 4 / December 2006, pp. 587 - 592
[66] Toma F., Sokolov D., Bertrand G., Klein D., Coddet C., Meunier C. *Comparison of the photocatalytic behavior of TiO2 coatings elaborated by different thermal spraying processes,* Journal of Thermal Spray Technology, Vol. 15, No. 4 / December 2006, pp 576 - 581
[67] Fauchais P., Rat V., Delbos C., Courdet J.F., Chartier T., Bianchi L. *Understanding of Suspension DC Plasma Spraying of Finely Structured Coatings for SOFC,* IEEE Transactions On Plasma Science, Vol. 33, 2005, No. 2 / April, pp. 920 - 930
[68] Toma F.-L., Berger L.-M., Naumann T., Langner S. *Microstructures of nanostructured ceramic coatings obtained by suspension thermal spraying,* Surface and Coatings Technology, Vol. 202, 2008, pp. 4343-4348

[69] Rampon R., Marchand O., Filiatre C., Bertrand G. *Influence of suspension characteristics on coatings microstructure obtained by suspension plasma spraying*, Surface and Coatings Technology, Vol. 202, 2008, pp. 4337–4342

[70] Rampon R., Filiatre C. and Bertrand G. *Suspension Plasma Spraying of YPSZ Coatings: Suspension Atomization and Injection*, Journal of Thermal Spray Technology, Vol. 17, No. 1 / March, 2008, pp. 105 - 114

[71] Rampon R., Toma F., Bertrand G. Coddet C. *Liquid plasma sprayed coatings of yttria-stabilized zirconia for SOFC electrolytes*, Journal of Thermal Spray Technology, Vol. 15, No. 4 / December 2006, pp 682 - 688

[72] Kaβner H., Vaβen R., Stöver D. *Study on instant droplet and particle stages during suspension plasma spraying (SPS),*Surface and Coatings Technology, Vol. 202, 2008, pp. 4355-4361

[73] Fazilleau J., Delbos C., Rat V., Courdet J.F., Fauchais P., Pateyron B. *Phenomena Involved in Suspension Plasma Spraying Part 1: Suspension Injection and Behavior,* Plasma Chem Plasma Process, Vol. 26, 2006, pp. 371–391

[74] Fauchais P. *Suspension and Solution Plasma or HVOF Spraying*, Journal of Thermal Spray Technology, Vol. 17, No. 1 / March, 2008, pp. 1 - 3

[75] Pawlowski L. *Suspension and solution thermal spray coatings,* Surface and Coatings Technology, Vol. 203, 2009, pp 2807-2829

[76] Pawlowski L. *Corrigendum to Finely grained nanometric and submicrometric coatings by thermal spraying: A review [Surface and Coatings Technology 202 (2008) 4318–4322],* Surface and Coatings Technology, Vol. 203, 2008, pp. 397

[77] Pawlowski L. *Finely grained nanometric and submicrometric coatings by thermal spraying: A review*, Surface and Coatings Technology Vol. 202, 2008, pp. 4318–4328

[78] Kaβner H., Siegert R., Hathiramani D., Vaβen R. and Stöver D. *Application of Suspension Plasma Spraying (SPS) for Manufacture of Ceramic Coatings,* Journal of Thermal Spray Technology, Vol. 17, No. 1 / March, 2008, pp 115 -123

[79] Ctibor P., Neufuss K., Chraska P. *Microstructure and abrasion resistance of plasma sprayed titania coatings,* Journal of Thermal Spray Technology, Vol. 15, No. 4 / December 2006, pp. 689-694

[80] Prevéy Paul S. *X-Ray Diffraction Characterization of Crystallinity and Phase Composition in Plasma-Sprayed Hydroxyapatite Coatings,* Journal of Thermal Spray Technology, Vol. 9 No. 3 / September 2000, pp. 369 -376

[81] Podlesak H., Schnick T., Pawlowski L., Steinhauser S., Wielage B. *Microscopic study of Al-SiC particulate composites processed by laser shocks,* Surface and Coatings Technology, Vol. 124, 2000, pp. 32-38

[82] Silva C. C., Almeida A. F. L., R. S. De Oliveira, Pinheiro A. G., Oes J. C. G, Sombra A. S. B. *Dielectric permittivity and loss of hydroxyapatite screen-printed thick films.* Journal of Material Science, Vol. 38, 2003, pp. 3713 – 3720

[83] Silva C.C., Rocha H.H.B., Freire F.N.A., Santos M.R.P., Saboia K.D.A., G´oes J.C. Sombra A.S.B. *Hydroxyapatite screen-printed thick films: optical and electrical properties,* Materials Chemistry and Physics, Vol. 92, 2005, pp. 260–268

[84] Soutoa Ricardo M., Lazb Marýa M., Reisc Rui L. *Degradation characteristics of hydroxyapatite coatings on orthopaedic TiAlV in simulated physiological media investigated by electrochemical impedance spectroscopy,* Biomaterials, Vol. 24, 2003, pp. 4213–4221

[85] Tomaszek R., Nitsch K., Pawlowski L., Znamirowski Z., Brylak M. *Impedance spectroscopy of suspension plasma sprayed titania coatings* Surface and Coatings Technology Vol. 201, 2006, pp. 1930–1934

[86] Zakharov N. A. and Orlovski V. P. *Dielectric Characteristics of Biocompatible* $Ca_{10}(PO_4)_6(OH)_2$ *Ceramics*. Technical Physics Letters, Vol. 27, No. 8, 2001, pp. 629–631

[87] Lazic Z. Design of Experiments in Chemical Engineering, Wiley-VCH,Germany 2004

[88] Pierlot Ch., Pawlowski L., Bigan M., Chagnon P. *Design of experiments in thermal spraying: A review*, Surface and Coatings Technology, Vol. 202, 2008, pp. 4483–4490

[89] Dyshlovenko S., Pierlot Ch. , Pawlowski L., Tomaszek R., Chagnon P. *Experimental design of plasma spraying and laser treatment of hydroxyapatite coatings*, Surface and Coatings Technology, Vol. 201, 2006, pp. 2054–2060

[90] Nemrod, software, version Education 2000 (Marseille, France)

[91] Markovic M., Fowler B**.,** Tung M., *Preparation and comprehensive characterization of calcium hydroxyapatite reference material,* Journal Res. Natl. Inst. Stand. Technology, Vol. 109, 2004, pp. 553-568

[92] Slosarczyk A., Knychalska-Karwan Z., Stobierska E., Paszkiewicz Z. *Cracow hydroxyapatite ceramics – a product report*

[93] Hornez J., Chai F., Blanchemain N., Lefevre A., Descamps M., Hildebrand H. *Biocompatibility Improvement of Pure Hydroxyapatite (Ha) with Different Porosity*, Key Engineering Materials Vol. 330-332, 2007, pp. 927-930

[94] **Jaworski R**., Pierlot Ch., Pawlowski L, Bigan M. and Quivrin M. *Synthesis and Preliminary Tests of Suspension Plasma Spraying of Fine Hydroxyapatite Powder* Journal of Thermal Spray Technology, Vol. 15,No. 5-6 / December 2008, pp. 679-684

[95] **Jaworski R**., Pierlot Ch., Pawlowski L., Bigan M., Martel M. *Design of the synthesis of fine HA powder for suspension plasma spraying*. Surface and Coatings Technology, Vol. 203, 2009, pp. 2092–2097

[96] **Jaworski R**., Pawlowski L., Roudet F., Kozerski S., Le Maguer A. *Influence of Suspension Plasma Spraying Process Parameters on* TiO_2 *Coatings Microstructure*, Journal of Thermal Spray Technology, Vol. 17, No.1 / March, 2008, pp. 73 - 81

[97] Piasecki T., Nitsch K., Pawłowski L., **Jaworski R.** *Impedance spectroscopy of suspension plasma sprayed hydroxyapatite coatings,* conference speech Szklarska Poręba 2009

[98] Fleig J., *Impedance Spectroscopy on Solids: The Limits of Serial Equivalent Circuit Models*, Journal of Electroceramics, Vol. 13, 2004, pp. 637–644

[99] Jonscher A.K., *Universal Relaxation Law*, Chelsea Dielectric Press, London 1996

[100] Jorcin J., Orazem M., Pébère N., Tribollet B., *CPE analysis by local electrochemical impedance spectroscopy*, Electrochimica Acta, Vol. .51, 2006, pp. 1473-1479

[101] Gittings J., Bowen C., Turner I., Baxter F., Chaudhuri J. *Characterisation of ferroelectric-calcium phosphate composites and ceramics*, Journal of the European Ceramic Society, Vol. 27, 2007, pp. 4187–4190

[102] **Jaworski R**., Pawlowski L., Roudet F., Kozerski S, Petit F. *Characterization of mechanical properties of suspension plasma sprayed* TiO_2 *coatings using scratch test*. Surface and Coatings Technology, Vol. 202, 2008, pp. 2644-2653

[103] Berger-Keller N., Bertrand G., Filiatre C., Meunier C., Coddet C. *Microstructure of plasma-sprayed titania coatings deposited from spray-dried powder,* Surface and Coatings Technology, Vol. 128, 2003, pp. 281-290

[104] Skryshevsky V., Dittrich T., Rappich J., *Electrical characterization of gas sensing devices based on porous TiO2,* Physica Status Solidi, *Applied Research* Vol. 197,No. 2, 2004, pp. 534-538

[105] Podlesak H., Pawlowski L., Laureyns J., **Jaworski R**, Thomas Lampke. *Advanced microstructural study of suspension plasma sprayed titanium oxide coatings*, Surface and Coatings Technology, Vol. 202, 2008, pp. 3723-3731

[106] Bouyer E., Gitzhofer F., Boulos M. *Morphological study of hydroxyapatite nanocrystal suspension* Journal of Materials Science: Materials in Medicine, Vol. 11, No. 8, 2000, pp. 523-531

[107] Li H., Ng B., Khor K., Cheang P., Clyne T. *Raman spectroscopy determination of phases within thermal sprayed hydroxyapatite splats and subsequent in vitro dissolution examination*, Acta Materialia, Vol. 52, 2004, pp. 445 – 453

[108] Gittings J., Bowen C., Dent A., Turner I., Baxter F., Chaudhuri J. *Electrical characterization of hydroxyapatite-based bioceramics*, Acta Biomaterialia, Vol. 5, 2009, pp. 743–754

[109] Rusiniak L., *Electric properties of water. New experimental data in the 5Hz – 13MHz frequency range*, Acta Geophysica Polonica, Vol. 52, 2004, pp. 63–76

[110] Catenaccio A., Daruich Y., Magallanes C., *Temperature dependence of the permittivity of water*, Chemical Physics Letters 367, 2003, pp. 669–671

7 APPENDIX

7.1 THE MICROGRAPHS OF SUSPENSION INJECTING SYSTEM OPTIMIZATION

The optimization was carried out by changing some parameters of injection, injector configuration and electric power input into plasma. All experiments were carried out with the use of PVS (shown in Figure 2.6 a)

SEM images of sample surfaces bring some information about the quality of the coatings. Two samples were chosen as examples to illustrate some effects of injection on the coating properties. The samples were presented in Figure 3.8. Micrographs of the experiments No. 7 to No. 23 (excluding No.8 and No.22) samples are shown below.

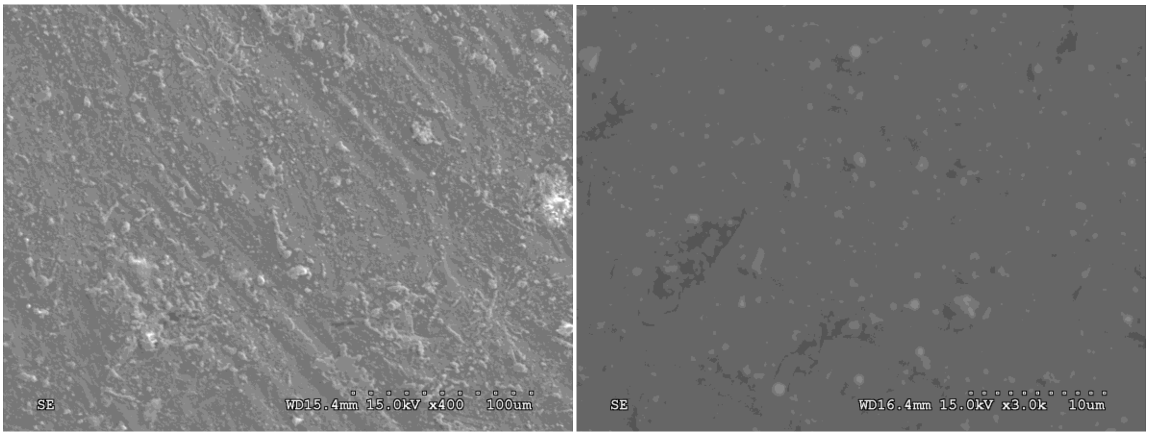

Micrographs of sample No. 7 (left - magnification x400) and No. 9 (right – magnification x3000)

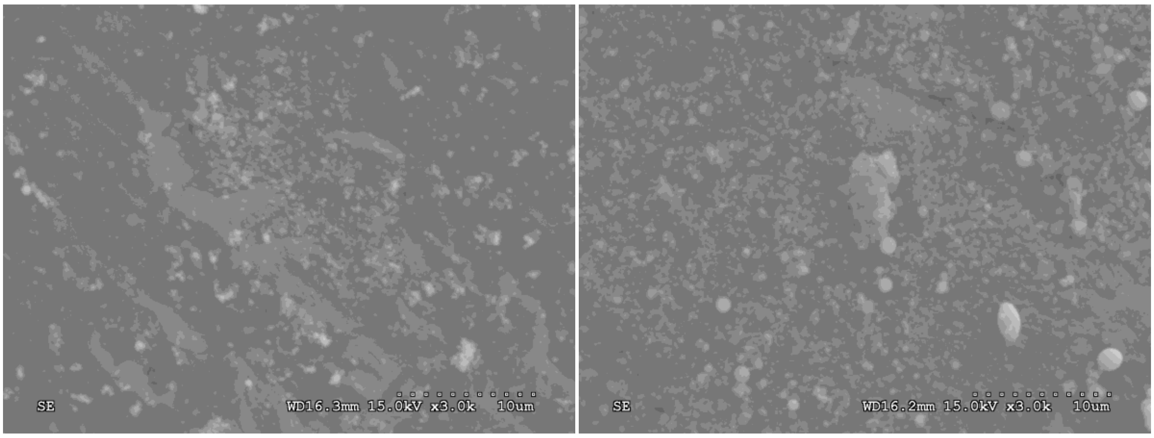

Micrographs of sample No. 10 (left - magnification x3000) and No. 13 (right – magnification x3000)

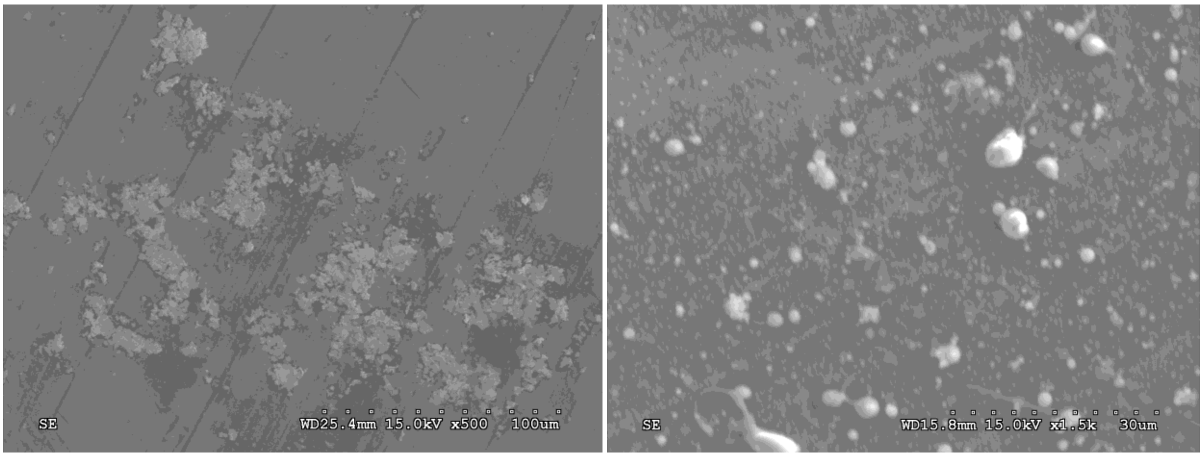

Micrograph of sample No. 14 (left - magnification x500) and No. 15 (right – magnification x1500)

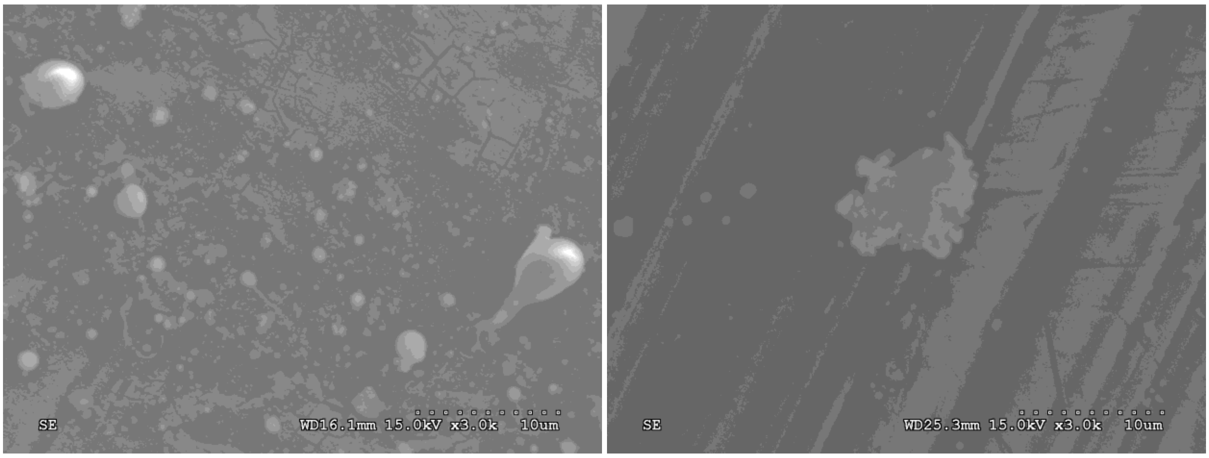

Micrograph of sample No. 16 (left - magnification x3000) and No. 17 (right – magnification x3000)

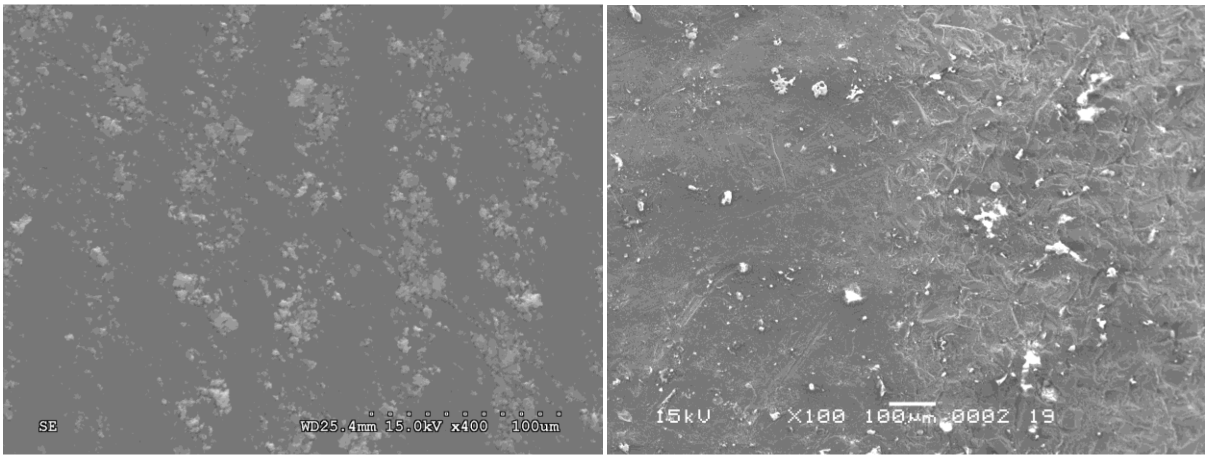

Micrograph of sample No. 18 (left - magnification x400) and No. 19 (right – magnification x100)

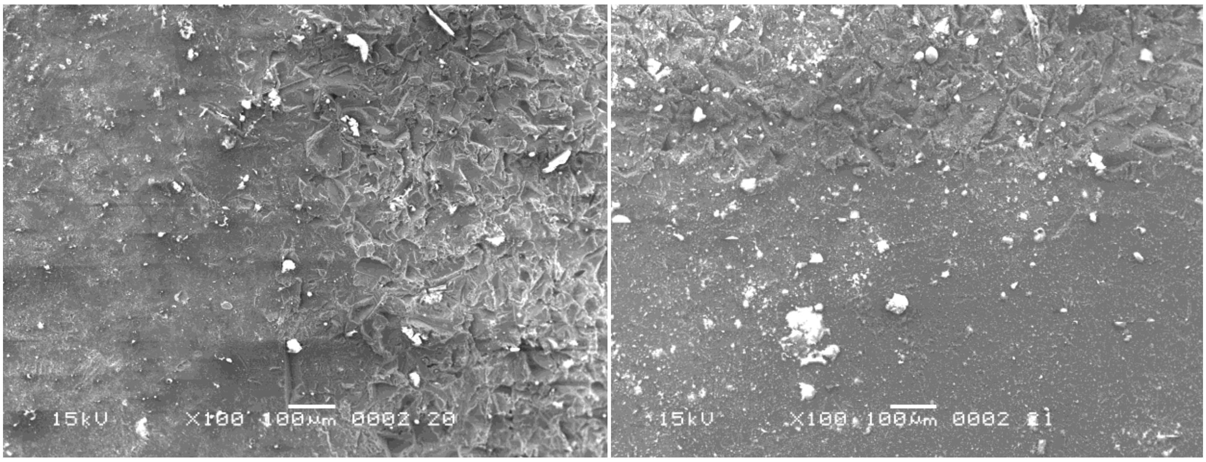

Micrograph of sample No. 20 (left - magnification x100) and No. 21 (right – magnification x100)

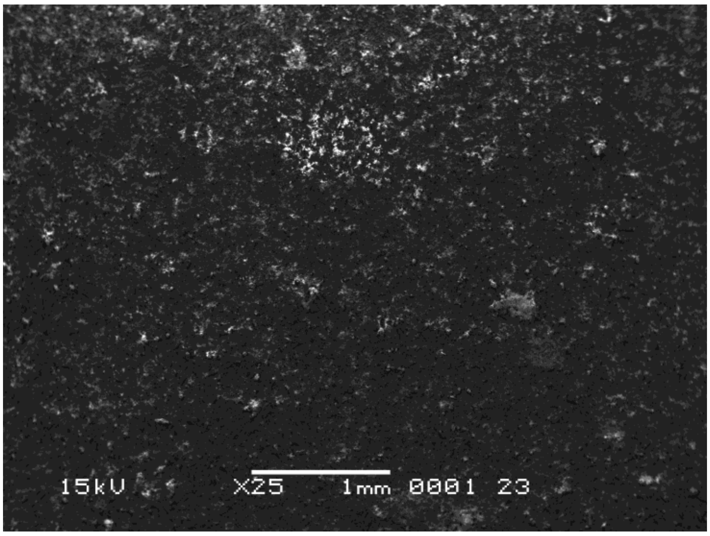

Micrograph of sample No. 23 (magnification x25)

7.2 FRACTION OF DECOMPOSED PHASES VS. IMMERSION TIME

The phase content analysis was carried out, using RIR method , for one of each experiment sample. The results of HA fractions calculations are shown in graphical form in Figure 3.12. Contents of remained phases are shown below.

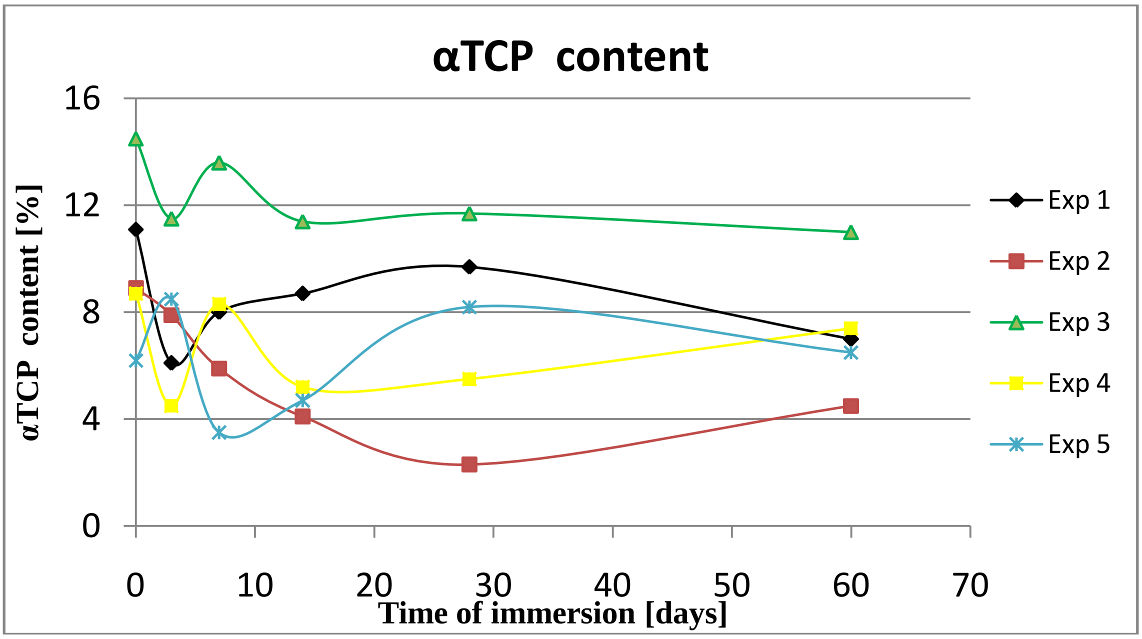

Content of αTCP vs. immersion time

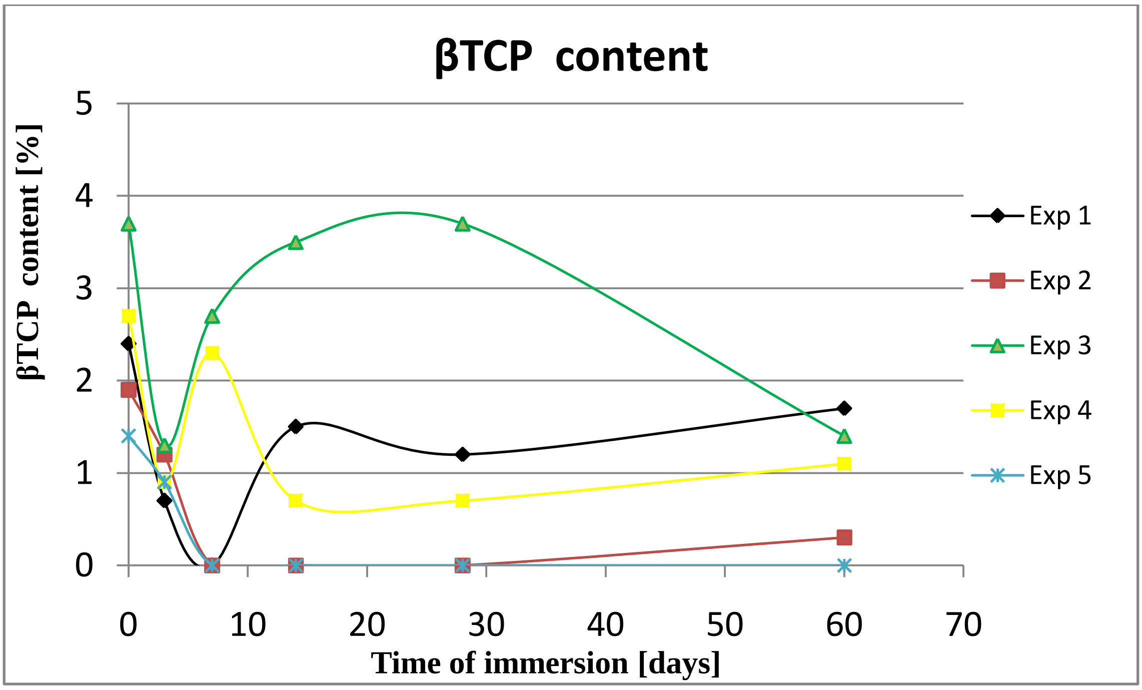

Content of βTCP vs. immersion time

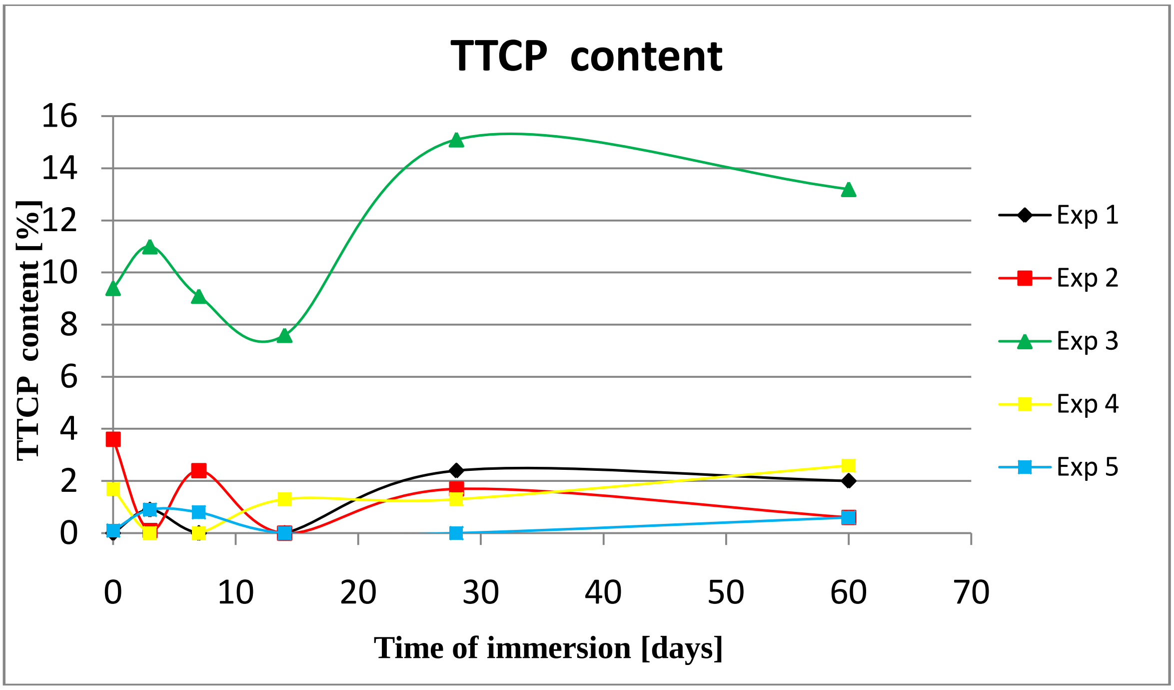

Content of TTCP vs. immersion time

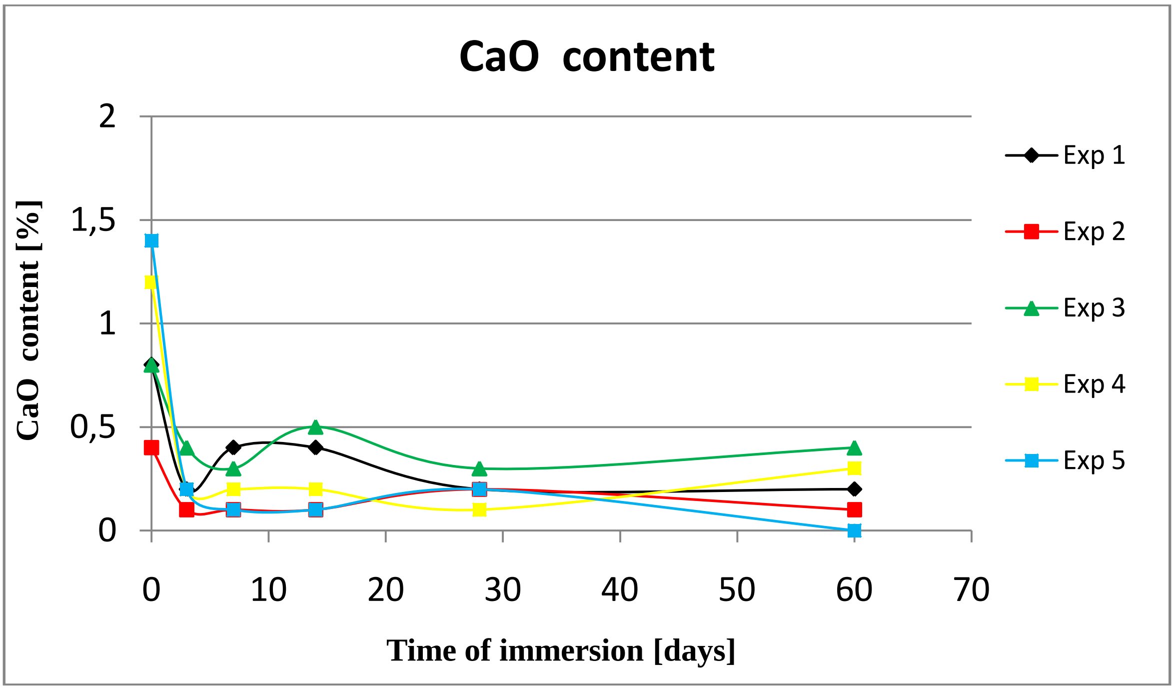

Content of CaO vs. immersion time

7.3 THE STATISTICAL ANALYSIS OF SPRAYING PARAMETERS INFLUENCE ON HA CONTENT (CALCULATED WITH NEMROD)

The statistical analysis was carried out with Nemrod software to observe the influence of spraying parameters on HA content. The results for samples without immersion in BSF were presented in Figure 3.13. The others results are shown below. The numbers in squares indicates HA content of the experiment carried out with parameters corresponding to values of variables shown on the axis and corrected by results of central experiment.

Results of statistical treatment showing influence of spraying parameters on HA content for experiments 1 to 5 after 3 days of immersion in BSF

Results of statistical treatment showing influence of spraying parameters on HA content for experiments 1 to 5 after 7 days of immersion in BSF

Results of statistical treatment showing influence of spraying parameters on HA content for experiments 1 to 5 after 14 days of immersion in BSF

Results of statistical treatment showing influence of spraying parameters on HA content for experiments 1 to 5 after 28 days of immersion in BSF

Results of statistical treatment showing influence of spraying parameters on HA content for experiments 1 to 5 after 60 days of immersion in BSF

7.4 THE RESULTS OF THE MICRO-RAMAN INVESTIGATIONS

The series of the experiments No. 2 and No. 5 were chosen for micro-Raman examinations. The coatings were investigated in the three or four points at the cross-section, i.e. one point adjacent to the substrate, two points in the middle of the coating and last one close to top of the coating. The marked points and the spectra corresponding to the samples 200, 207, 500, 560, which were chosen as the most interesting were presented in Figure 3.16 - 3.19. The other micrographs and micro-Raman spectra are shown below. The substrate is always presented on the left hand side on the micrograph, then marked points on the coating and bright area on the right hand side corresponds to epoxy resin.

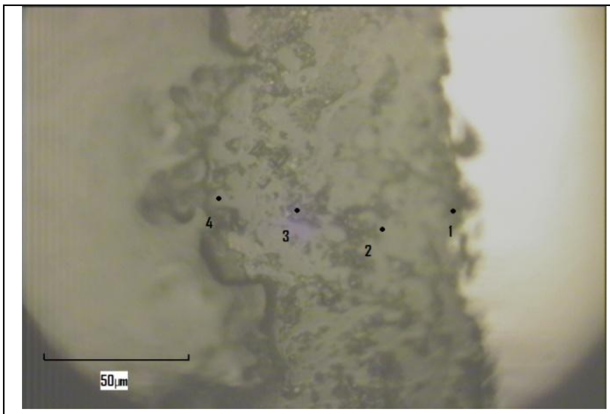

Sample 203 –measurements points

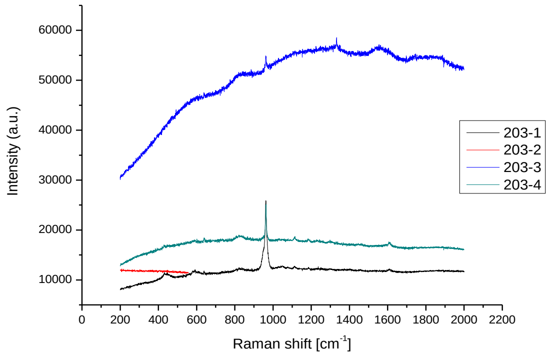

Sample 203 –Raman spectra

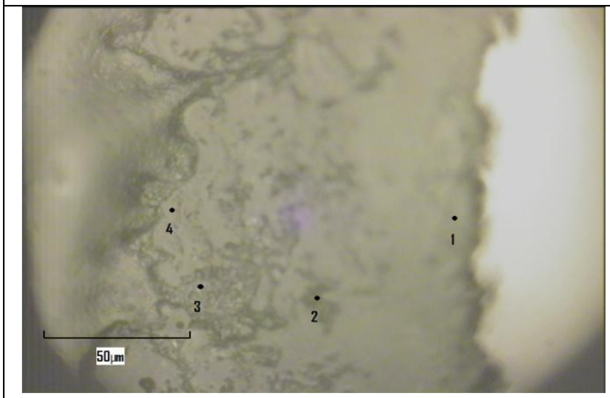

Sample 214 –measurements points

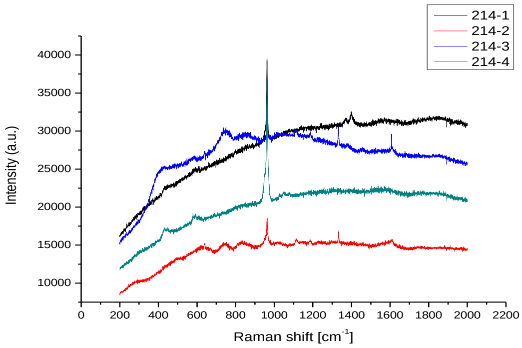

Sample 214 –Raman spectra

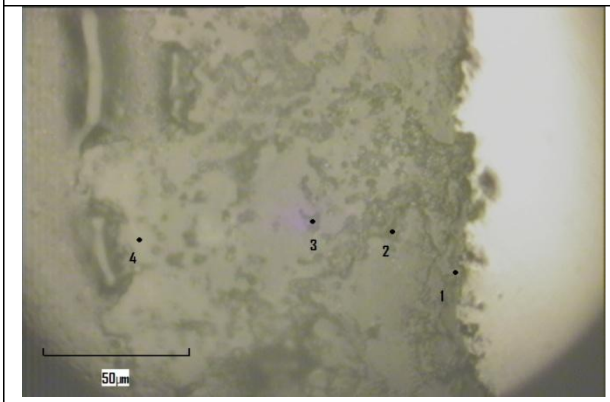

Sample 228 –measurements points

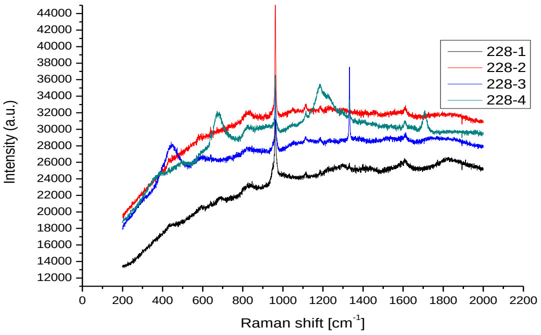

Sample 228 –Raman spectra

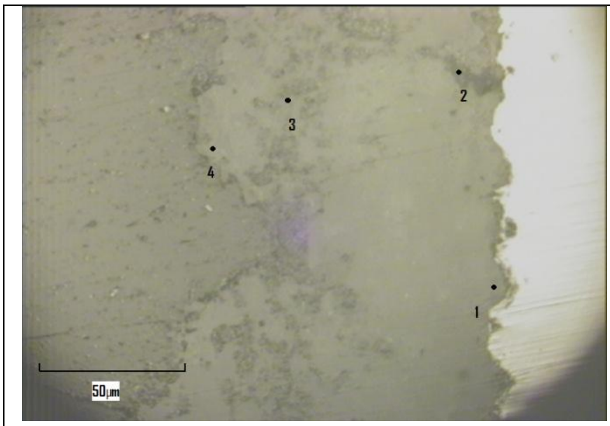

Sample 260 –measurements points

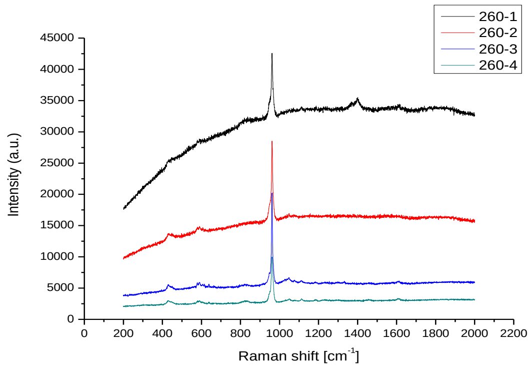

Sample 260 –Raman spectra

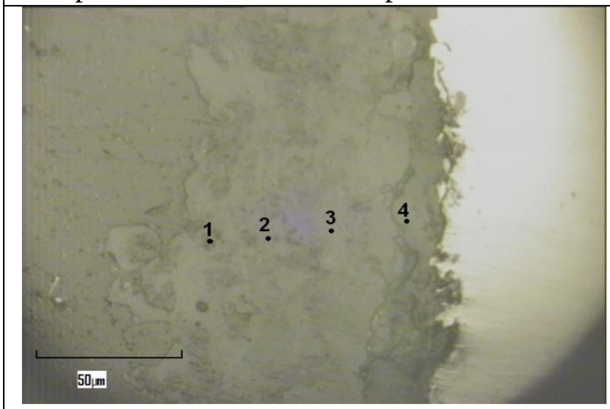

Sample 503 –measurements points

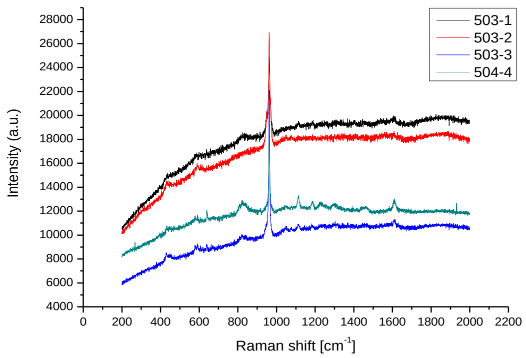

Sample 503 –Raman spectra

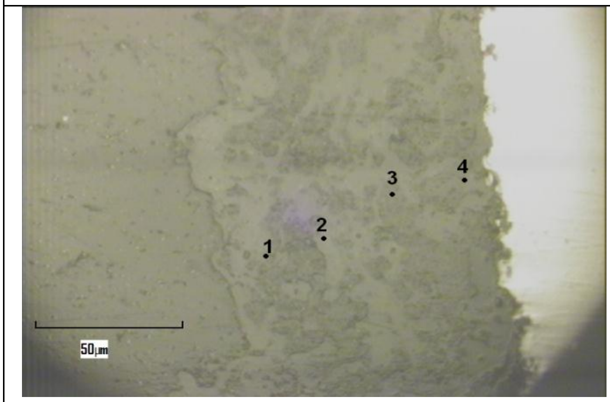

Sample 507 –measurements points

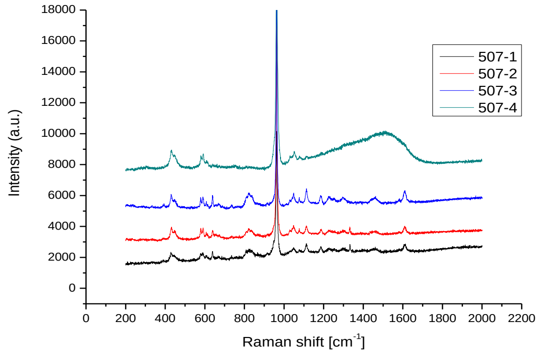

Sample 507 –Raman spectra

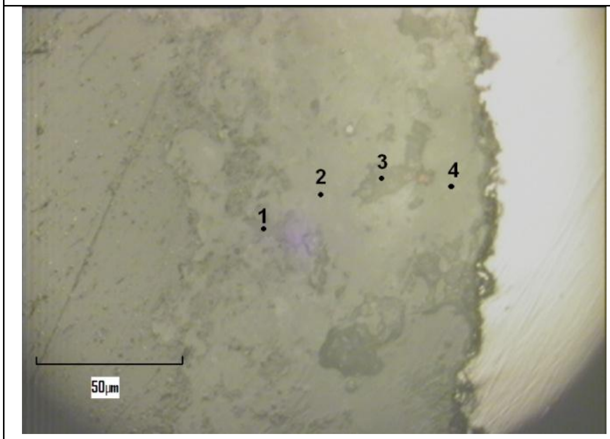

Sample 514 –measurements points

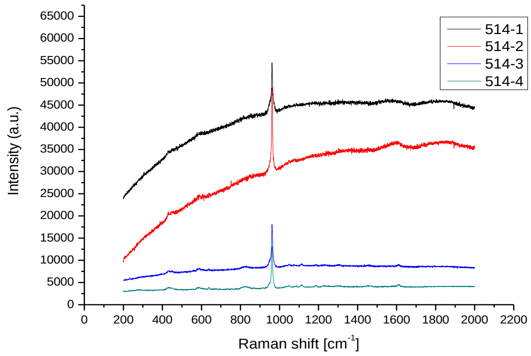

Sample 514 –Raman spectra

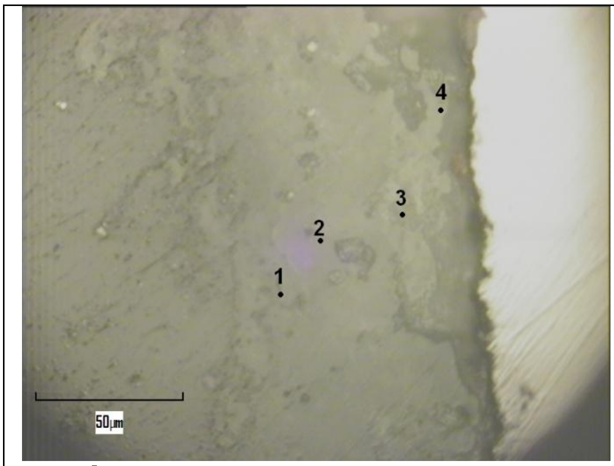

Sample 528 –measurements points

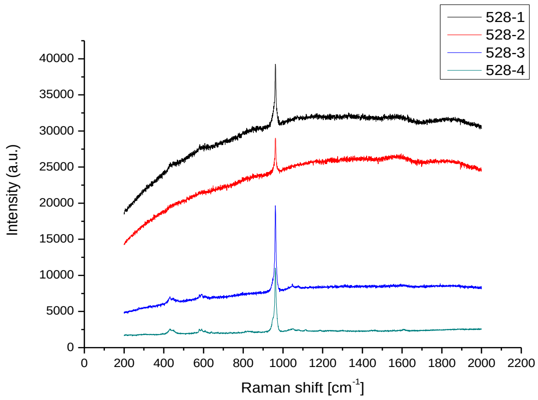

Sample 528 –Raman spectra

7.5 THE RESULTS OF Ca/P RATIO MEASUREMENTS BY EMPA

Sample series of experiment No. 2 were chosen to analysis by EMPA. The samples cross-sections were put into the vacuum chamber in Cameca EMPA and then quantitative measurements of Ca and P content were done. Measurements were carried out along the red line marked on the presented micrographs. As representative samples 200, 207 and 260 were shown in section 3.4.6 (Figure 3.20, Figure 3.21, Figure 3.22). The rest of samples photos and Ca/P ratios are shown below.

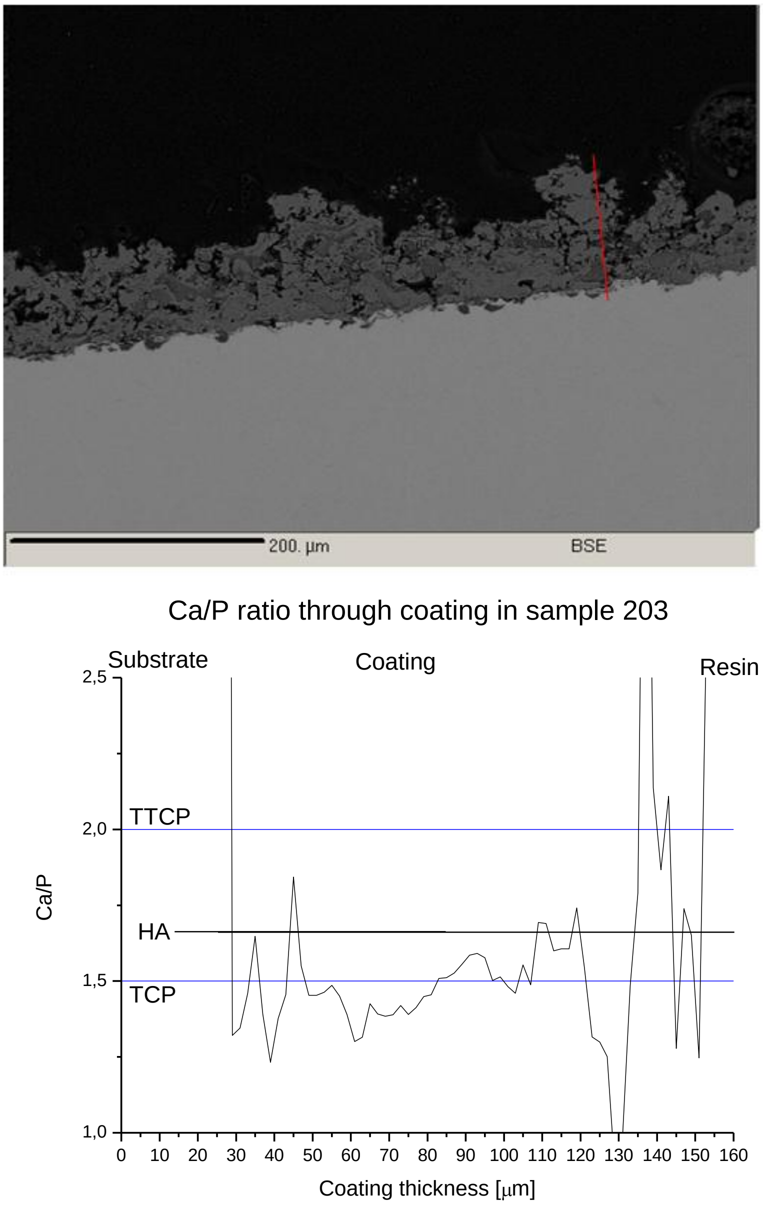

Cross-section of 203 sample (top), and corresponding course of Ca/P ratio along marked line (down).

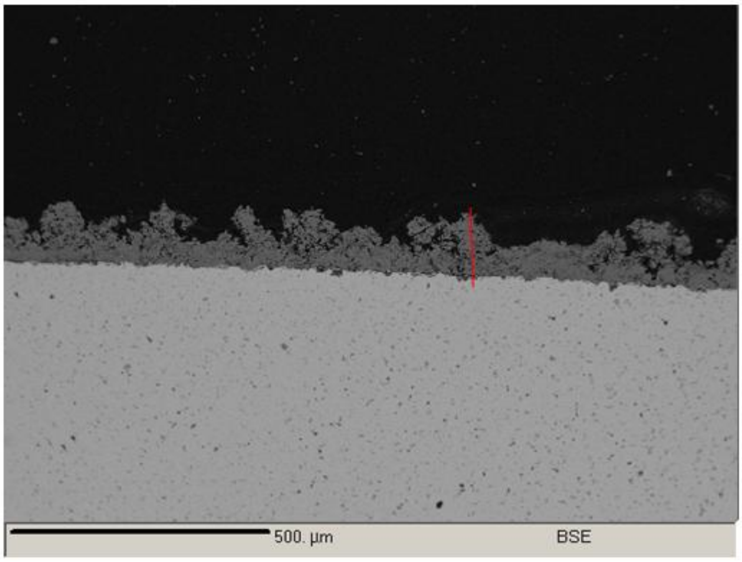

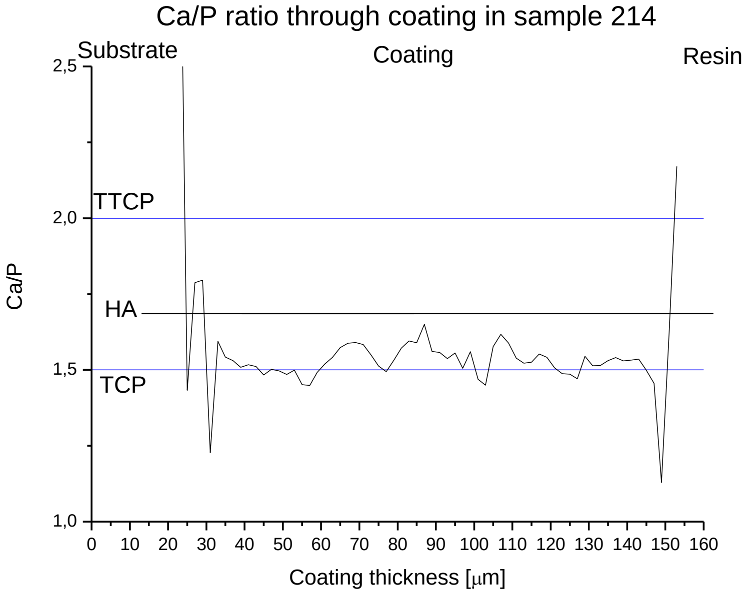

Cross-section of 214 sample (top), and corresponding course of Ca/P ratio along marked line (down).

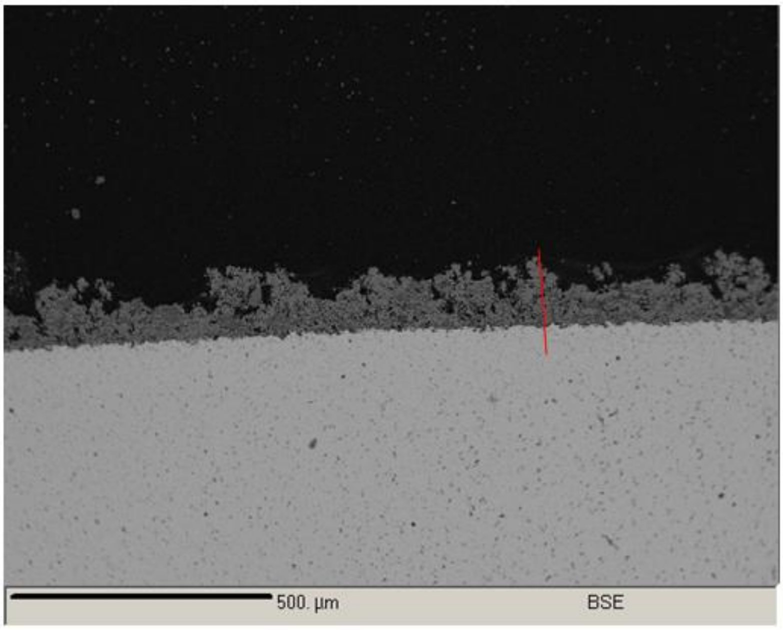

Ca/P ratio through coating in sample 228

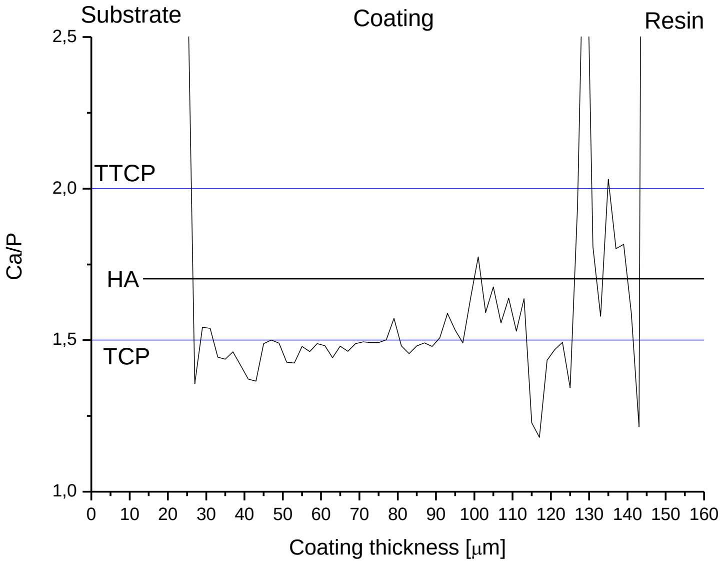

Cross-section of 228 sample (top), and corresponding course of Ca/P ratio along marked line (down).

7.6 AUTHOR'S PUBLICATIONS

a) Piasecki T., Nitsch K., Pawłowski L., **Jaworski R.** *Impedance spectroscopy of suspension plasma sprayed hydroxyapatite coatings,* Optica Applicata, accepted for publication

b) Kozerski S., Pawlowski L., **Jaworski R**., Roudet F., Petit F. *Two zones microstructure of suspension plasma sprayed hydroxyapatite coatings*, Surface and Coatings Technology, (2009), xxxx, available on line www.sciencedirect.com

c) **Jaworski R**., Pierlot Ch., Pawlowski L., Bigan M., Martel M. *Design of the synthesis of fine HA powder for suspension plasma spraying,* Surface and Coatings Technology, Vol. 203, 2009, pp. 2092–2097

d) **Jaworski R**., Pierlot Ch., Pawlowski L, Bigan M. and Quivrin M. *Synthesis and Preliminary Tests of Suspension Plasma Spraying of Fine Hydroxyapatite Powder* , Journal of Thermal Spray Technology, Vol. 15,No. 5-6 / December 2008, pp. 679-684

e) Podlesak H., Pawlowski L., Laurens J., **Jaworski R**., Lampke T. *Advanced microstructural study of suspension plasma sprayed titanium oxide coatings,* Surface and Coatings Technology, Volume 202, Issue 15, 25 April 2008, Pages 3723-3731

f) **Jaworski R**., Pawlowski L., Roudet F., Kozerski S., Petit F. *Characterization of mechanical properties of suspension plasma sprayed TiO_2 coatings using scratch test,* Surface and Coatings Technology, Volume 202, Issue 12, 15 March 2008, Pages 2644-2653

g) **Jaworski R**., Pawlowski L., Roudet F., Kozerski S., Le Maguer A. *Influence of Suspension Plasma Spraying Process Parameters on TiO_2 Coatings Microstructure,* Journal of Thermal Spray Technology, Volume 17, Number 1 / March 2008

h) **Jaworski R.**, Pierlot C., Tomaszek R., Pawlowski L., Znamirowski Z., Zdanowski J. *Optimization of Dielectric Properties of Suspension Plasma Sprayed Hydroxyapatite Coatings,* Mat.-wiss. u. Werkstofftech. 2007, 38, No. 2